Michaela Hawranek, BSc

Quantitative Evaluation of Left Ventricular Myocardial Perfusion using Computed Tomography - Assessment of Image Quality

MASTER'S THESIS

to achieve the university degree of

Diplom-Ingenieurin

Master's degree programme: Biomedical Engineering

submitted to

Graz University of Technology

Supervisor

Dipl.-Ing. Dr.techn. Theresa Margarethe Rienmüller

Institute of Health Care Engineering

Graz, May 2019

EIDESSTATTLICHE ERKLÄRUNG

AFFIDAVIT

Ich erkläre an Eides statt, dass ich die vorliegende Arbeit selbstständig verfasst, andere als die angegebenen Quellen/Hilfsmittel nicht benutzt, und die den benutzten Quellen wörtlich und inhaltlich entnommenen Stellen als solche kenntlich gemacht habe. Das in TUGRAZonline hochgeladene Textdokument ist mit der vorliegenden Masterarbeit/Diplomarbeit/Dissertation identisch.

I declare that I have authored this thesis independently, that I have not used other than the declared sources/resources, and that I have explicitly indicated all material which has been quoted either literally or by content from the sources used. The text document uploaded to TUGRAZonline is identical to the present master's thesis/diploma thesis/doctoral dissertation.

Datum / Date

Unterschrift / Signature

Die Technische Universität Graz übernimmt mit der Betreuung und Bewertung einer Masterarbeit keine Haftung für die erarbeiteten Ergebnisse: Eine positive Bewertung und Anerkennung (Approbation) einer Arbeit bescheinigt nicht notwendigerweise die vollständige Richtigkeit der Ergebnisse.

Abstract

The quantitative evaluation of myocardial perfusion using computed tomography is a promising modality, since technical improvements, such as higher temporal resolution and the wider detectors, have been introduced. However, the result of the perfusion calculation depends on the quality of the data obtained from CT images.

The aim of this work is to assess the quality of these CT images. For this purpose, the image noise, the signal-to-noise ratio and the contrast-to-noise ratio of 14 patients at five different locations of the myocardium were determined. For the subjective evaluation of image quality, four radiologists were questioned in regard to image contrast, image noise, artifacts and reason for the artifacts. The perfusion was calculated using the Upslope and the Fermi method. In the Upslope method, the raw data were fitted by model curves, which are further used for perfusion calculation. To assess the quality of the model curves fitting to the raw data, the difference between myocardial and ventricular baseline, the signal-to-noise ratio and contrast-to-noise ratio of the model curves are determined.

It can be shown that in both, the Upslope and the Fermi method, outliers were found in the perfusion results. One reason for these outliers was the high image noise, which was mainly caused by streak-artifacts from the vertebral body. Another reason was the wrong timing between contrast agent start and scan start, which led to differences between the myocardial and ventricular baseline. Therefore, to improve the results of the perfusion calculation, artifacts should be avoided, and the timing between the contrast agent start and scan start should be optimized.

Key words: Myocardial perfusion, image quality, signal-to-noise ratio, contrast-to-noise ratio, artifacts

Zusammenfassung

Die quantitative Bestimmung der Myokardperfusion mittels Computertomographie ist eine vielversprechende Modalität, seitdem technische Verbesserungen wie eine höhere zeitliche Auflösung und breitere Detektoren eingeführt wurden. Das Ergebnis der Perfusionsberechnung hängt allerdings von der Qualität der Daten ab, die aus den CT-Bildern gewonnen werden.

Ziel dieser Arbeit ist es, die Qualität dieser CT-Bilder zu beurteilen. Dazu wurde das Bildrauschen, das Signal-Rausch-Verhältnis und das Kontrast-Rausch Verhältnis von 14 Patienten an fünf verschiedenen Stellen des Myokards bestimmt. Zur subjektiven Bewertung der Bildqualität wurden vier Radiologen zu Bildkontrast, Bildrauschen, Artefakten und Gründen für die Artefakte befragt. Die Berechnung der Perfusion erfolgte mittels der Upslope und der Fermi Methode. Bei der Upslope Methode werden die Rohdaten durch Modellkurven angepasst, die in weiterer Folge zur Perfusionsberechnung verwendet werden. Um die Qualität der Anpassung der Modellkurven an die Rohdaten zu ermitteln, wurden der mittlere quadratische Fehler, der Unterschied zwischen myokardialer und ventrikulärer Basislinie sowie Signal-Rausch-Verhältnis und Kontrast-Rausch-Verhältnis der Modellkurven bestimmt.

Es konnte gezeigt werden, dass sowohl in der Upslope als auch in der Fermi Methode Ausreißer in den Perfusionsergebnissen zu finden waren. Ein Grund dafür lag im erhöhten Bildrauschen, das vorwiegend durch Streifenartefakte aus dem Wirbelörper verursacht wurde. Ein weiterer Grund lag am falschen Timing zwischen Kontrastmittelstart und Scanstart, der zu Unterschieden zwischen der myokardialen und ventrikulären Basislinie führte. Um die Ergebnisse der Perfusionsberechnung zu verbessern, sollten deshalb Artefakte vermieden werden und das Timing zwischen Kontrastmittelstart und Scanstart optimiert werden.

Schlüsselwörter: Myokardperfusion, Bildqualität, Signal-Rausch-Verhältnis, Kontrast-Rausch-Verhältnis, Artefakte

Contents

List of Figures

List of Tables

List of Abbreviations

ACC American College of Cardiology

AFC alternative forced choice

AFROC alternative free-response ROC

AHA American Heart Association

AIF arterial input function

ANOVA analysis of variance

CAD coronary artery disease

CHD coronary heart disease

CNR contrast-to-noise ratio

CT computed tomography

CTA CT angiography

CTDI computer tomography dose index

CTP CT perfusion

CVD cardiovascular disease

DECT dual-energy CT

DLP dose length product

DQE detective quantum efficiency

DRL diagnostic reference level

DROC differencial ROC

DSCT dual-source CT

ECG electrocardiography

FBP filtered back projection

FFE free-response forced error

FFR fractional flow reserve

FROC free-response ROC

Gy Gray

HU Hounsfield unit

ICA invasive coronary angiography

IR iterative reconstruction

IV intravenous

LAD left anterior descending

LCX left circum-flex

LROC localization ROC

MBF myocardial blood flow

MDCT multi-detector CT

MPI myocardial perfusion imaging

MRI magnetic resonance imaging

MSE mean square error

MTF modulation transfer function

NPS noise power spectrum

NPV negative predictive value

RCA right coronary artery

ROC receiver operating characteristics

ROI region of interest

SNR signal to noise ratio

SPECT single-photon emission computed tomography

TAC time-attenuation curve

VGA visual grading analysis

VGC visual grading characteristics

1 Introduction

Cardiovascular disease (CVD) claims more than 4 million lives in 2016, accounting for 45 % of all deaths each year in Europe. The most common cause of CVD is the coronary heart disease (CHD) with 19 % of all deaths, accounting for 1.8 million deaths [1].
Atherosclerotic disease leading to obstructive coronary artery disease takes typically decades to develop. These patients are often asymptomatic for years. But, when symptoms of angina or angina equivalent manifest, patients are referred for myocardial perfusion imaging (MPI). That is not only for risk stratification but also to determine if they benefit from revascularisation [2].

Guidelines from national organizations, including the American Heart Association (AHA) and the American College of Cardiology (ACC), provide guidance on the choice and use of these techniques in the area of echocardiography, cardiac radionuclide imaging, cardiac computed tomography (CT), and cardiac magnetic resonance imaging (MRI) [3]. CT is the only of the aforementioned imaging technologies that is able to provide the anatomic assessment of the coronary arteries and functional evaluation of the downstream myocardial territory in a single mode.

Although the concept of CT examination for myocardial perfusion defect was first investigated in 1978 [4], its reliability has only been increased with recent advancements in CT technologies [5]. In 2005 Kurata et al. [6] explored the first attempt to use multi-detector CT (MDCT) to characterize myocardial perfusion defects in human under stress, using adenosine stress on a 16-detector

MDCT scanner. The study showed a good agreement between myocardial CT perfusion (CTP) and thallium-201 myocardial perfusion scintigraphy. However, CT perfusion at that time had limitations in the temporal resolution and was not sufficient to provide diagnostic image quality at higher heart rates, which occur during adenosine stress acquisition [6]. Newer generations of scanners show improved results in the evaluation of the feasibility of stress myocardial CTP in both animal models and humans [5][7].

The introduction of 64-detector CT improves the performance of adenosine CT perfusion imaging. Hence, it led to a notable reduction of the scan time, motion artefacts, use of contrast agent, and radiation dose exposure. This yields to a higher spatial and temporal resolution at the same time and widened the application of CT from anatomical detection of CAD to physiological assessment of myocardial ischemia [8]. Several clinical studies have established the value of myocardial CT perfusion (CTP) compared to reference standards as SPECT, invasive coronary angiography (ICA) (with or without fractional flow reserve (FFR)) and stress perfusion MRI [9].

Nonetheless, there are still some limitations of dynamic CT myocardial perfusion imaging. Due to the dynamic scans, a long breath-hold time for whole-heart scanning ($>$ 30 seconds) is necessary, which can lead to patient movement and therefore to motion-artifacts. Further, spatial misalignments resulting from table movements are possible. These limitations may influence the image quality of the CT scans and therefore the results of the perfusion calculation. Besides, the higher radiation dose in the dynamic scanning, compared to static scanning, has to be kept in mind (see Section 2.4.5).

1.1 Motivation and Goal

The goal of this master thesis is to find and determine suitable quality parameters for both, the image quality and the evaluation of myocardial perfusion imaging using computed tomography. Further it would be interesting, if the image quality of the myocardium is depended on the myocardial location. The myocardial perfusion was calculated using two different methods, in particular the Upslope [10] and the Fermi [11] method. The upslope method, which requires curve fitting algorithms, was used as a quality criterion. This algorithm was applied to five different regions of interest (ROI) of the myocardium to compare these aforementioned quality parameters.

Toifl, 2014 [12] has done the groundwork in his master thesis in terms of signal processing for perfusion calculation. Therefore, he provided a Matlab-workflow for myocardial perfusion calculation. This workflow was used for the perfusion calculation here. Additionally, image quality parameter calculation methods were integrated.

Many of the recent researchers use post-processing methods like temporal or spatial filtering, de-noising, segmentation, registration and so on, to achieve better image quality results and therefore better perfusion quantification results. But, the focus on this work lies on image quality assessment of axial reconstructed CT scans without any of these post-processing methods. Hence, it is possible to detect image quality degrading factors like artifacts.

1.2 Thesis Structure

This thesis is structured as follows: Firstly, the section *Related Research* gives an overview of myocardial perfusion imaging with computed tomography and demonstrates quantification methods for the perfusion calculation. It also gives an overview of image quality in CT and describes image quality assessment tools for CT. Next, in the *Methods* section, the methods for the qualitative and quantitative assessment of image quality using CT are described. Besides, curve fitting methods and their quality criterion's are presented in this section. After that, the *Result* section shows the results of the quality parameter for a ROI comparison prepared in graphics and text. Afterwards, these results are discussed in the *Discussion* section. Finally, the results are summarized in the *Conclusion* section.

2 Related Research

The first two sections of this chapter give an overview about the medical background for the evaluation of myocardial perfusion using CT and introduce to the the static and dynamic perfusion imaging protocols. The focus of section 2.3 lies on the explanation of nondeconvolution-based and deconvolution-based methods: Both methods are used for the quantification of CT myocardial perfusion. The last two sections deal with the topic image quality. On the one hand the technical aspects that have an impact on image quality and on the other hand image quality assessment tools.

2.1 Myocardial Perfusion Imaging with Computed Tomography

Since the introduction of MDCT more than 15 years ago, coronary computed tomography angiography (CTA) has become the mainly used noninvasive imaging modality for the detection and exclusion of significant coronary stenosis [8], [9]. Because of its high sensitivity and negative predictive value (NPV) ($\geq 95\,\%$) for the detection of significant coronary stenosis, CTA is currently recommended as the first diagnostic test on symptomatic patients with low-to-intermediate probability of coronary artery disease (CAD) [8][9]. Furthermore, CTA has also a prognostic value providing information on the total plaque burden, with a better outcome when there is no evidence of atherosclerosis and a worse prognosis depending on the extent and severity of CAD [8].

The actual limit of CTA is the evaluation of the hemodynamic significance of CAD due to the lack of functional information for a given stenosis [9] related

to its moderate positive predictive value (about 50 %) in detecting inducible myocardial ischemia [8]. It is important to improve the physiological evaluation, because it influences the outcome of CAD more than its anatomical detection [8]. In fact, studies have demonstrated that a strategy guided by the invasive hemodynamic parameter fractional flow reserve (FFR) may be superior to a angiography-guided strategy alone. Thus, revascularization should be guided by functional assessment of myocardial ischemia. In absence of myocardial ischemia, revascularization offers no symptomatic or prognostic benefit for patients, while it is effective in patients with moderate to severe ischemia (total myocardial ischemia >10 %) [8]. Therefore, functional tests such as single photon emission computed tomography (SPECT), stress echocardiography or stress perfusion MRI are necessary to guide coronary revascularization [8][9]. Stress myocardial CTP provides both anatomic and physiological information [5].

The classic ischemic cascade is useful to understand the relationships of pathophysiology of myocardial ischemia leading to infarction. Although it was developed on a temporal scale of minutes after occlusion of a coronary artery, it helps to understand the relationship between the severity of ischemia and its resulting abnormalities [13]. At first, perfusion abnormalities occur, before metabolic alterations, wall motion abnormalities, ECG changes, and symptoms [8]. Because of coronary autoregulation myocardial perfusion at rest is normal until the luminal diameter narrowing of a coronary artery exceeds 85-90 %. In presence of coronary stenosis greater than 45 % maximal coronary hyperemia, which is induced by coronary arteriolar vasodilator, leads to a progressive decrease in the hyperemic response [14]. Under this condition, exercise or pharmalogical vasodilation of subepicardial resistance vessels results in a reduction in distal coronary pressure that redistributes flow away from the subendocardium that leads to a "transmural steal" phenomenon. The pharmacological stress agents adenosine and dipyridamole are used to induce the myocardial hyperemia. Two intravenous

(IV) lines are crucial for the injection of contrast media and of the vasodilator agent, respectively [8].

The application of adenosine requires an infusion pump with an infusion rate of 140 µg/kg/min for 3 to 5 minutes. The most common side effects are flushing, chest pain, dyspnea, or nausea. Because of the short half-life of 30 s most side effects resolve in a few seconds after discontinuation of the adenosine infusion [8]. Dipyridamole can be applied manually at a slow rate in a dose of 0.56 mg/kg to 0.84 mg/kg over a 4 to 6- minute period. Caused by its longer half-life of approximately 30 min, in some patients the administration of aminophylline for reversal of persistent symptoms may be required [15][9].

Recently, regadenoson has been introduced as a pharmacological stress vasodilator, which has a safer side effect profile in comparison to adenosine and dipyridamole, especially for patients with asthma or severe chronic obstructive pulmonary disease. However, it is limited by its cost and it is not widely available [8].

2.2 CT Perfusion Imaging Protocols

The protocol of CTP imaging is similar to other noninvasive imaging techniques such as nuclear imaging and stress cardiac MRI. It includes the evaluation of myocardial perfusion during both rest (baseline) and stress (hyperemia) conditions in order to differentiate reversible from fixed myocardial perfusion defects [8]. After intravenous administration of iodinated contrast agent (typically via antecubital vein), CTP imaging analysis is performed by imaging the left ventricular (LV) myocardium during the first pass of the contrast bolus as a surrogate marker of myocardial blood flow (MBF), similar to stress perfusion MRI [9]. Because iodinated contrast agents attenuates X-ray directly proportionally to iodine content in tissue, myocardial perfusion defects can be directly visualized as hypoattenuated or nonenhancing myocardial regions. For the reason that

a rapid wash-out of contrast agent due to diffusion to the extravascular space after about 1 min is expected, imaging during the early portion of first-pass circulation is critical. To optimize the strength of enhancement in the first-pass of the arterial phase, the contrast injection needs a high flow rate of at least 5 ml/s [8].

A combined coronary CTA/CTP imaging protocol could be performed. The two protocols mostly used are named according to sequence of scan acquisition: rest/stress or stress/rest. These two sequences should be separated by an interval of 10-15 minutes to provide an optimal contrast wash-out.

The **rest/stress protocol** is the preferred approach for patients with low-to-intermediate probability, because it uses the ability of coronary CTA to rule out obstructive CAD. Stress CTP imaging is performed only in the presence of anatomically defined CAD of intermediate or obstructive coronary stenosis to assess the physiological significance of CAD. Further radiation and iodinated contrast exposure can be avoided in absence of coronary artery stenosis. However, this protocol is limited by the risk of cross-contamination of contrast in the stress phase and the use of beta-blockers before the rest acquisition may confound perfusion defects and leads to underestimation of myocardial ischemia. For patients with high pre-test probability of CAD or patients with known CAD, the **stress/rest protocol** could be more suitable. The advantage is the reduced risk of contrast media contamination from the rest phase that may confound perfusion defects, which may decrease sensitivity for infarction. Moreover, beta-blocker and nitrates may be administrated after the stress and before the rest protocol to avoid interfering with the stress perfusion evaluation [9]. Certainly, the best protocol should be tailored on the patients risk profile [8].

There are two approaches for the evaluation of CT myocardial perfusion imaging: Static CT myocardial perfusion which can further be divided into single energy and dual energy techniques, and dynamic CT myocardial perfusion [16] [17].

2.2.1 Static CT Myocardial Perfusion Imaging

Static CTP imaging is based on a static evaluation of contrast medium distribution in the myocardium during early attenuation [17]. It allows visual qualitative assessment of a single snapshot, which encompasses the entire left ventricle, of myocardial iodine contrast attenuation. The acquisition is performed during the early arterial phase of first-pass contrast enhancement, at the moment of peak contrast concentration in the coronary arteries, to detect early contrast uptake differences. Bischoff, Bamberg, Marcus, *et al.* [18] found that the optimal time frame for stress CT-MPI is between 8 and 16 s after contrast enhancement in the ascending aorta exceeds 100 HU. These acquisition parameters can also be used for the evaluation of coronary artery stenosis and myocardial blood supply. So it is possible to perform static single-shot myocardial CT-MPI using any CT scanner capable of acquiring diagnostic-quality coronary CT angiography (CTA) [16].

To evaluate the static myocardial perfusion at rest, generally, coronary CTA image sets, already obtained for the morphologic assessment of the coronary arteries, are used and no additional radiation or acquisition time is necessary. For the assessment of myocardial perfusion at stress, an additional acquisition during pharmacologic stress can be obtained [16].

The qualitative assessment is performed by visual evaluation of left ventricular myocardial contrast enhancement, which is sometimes complemented by attenuation measurements of the ischemic and nonischemic myocardium. It is also possible to make a semi-quantitative assessment of myocardial perfusion by using the transmural perfusion ratio, which is the ratio between subendocardial and subepicardial ratio [16].

Limitations of Static Myocardial Perfusion Imaging

There are some limitations of static myocardial perfusion imaging. The timing of image acquisition significantly influences diagnostic accuracy because the peak of contrast attenuation may be missed [18]. Additionally, artifacts like beam hardening, motion artefacts, and partial scan artifacts may occur when using the static technique.

2.2.2 Dynamic CT Myocardial Perfusion Imaging

To determine the perfusion related parameters a 4D cardiac image data set is required to create time-attenuation curves (TACs) for the region of interest (ROI) (see figure 2.1). Therefore, a focus-centered 2D detector and an X-ray source are moving on a circular path around the anatomy acquiring continuously projection data to obtain the images. The ECG is recorded in parallel to the circular scan [19].

Dynamic CT-MPI uses serial acquisitions of the myocardium through the whole cardiac cycle to track the kinetics of contrast media distribution during the initial pass, arterial phase and microcirculation. It takes up to 32 s after the administration of contrast medium for differences between normal and abnormal myocardium to show.

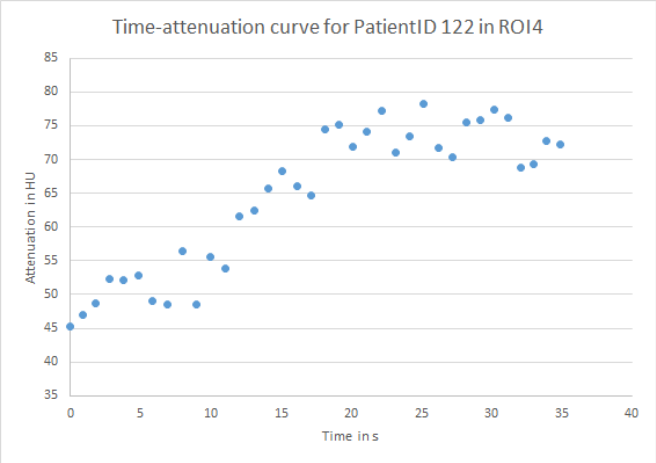

Figure 2.1: Time-attenuation curve for PatientID 122 in Myocardium ROI 4.

For a dynamic CT perfusion imaging study, a greater volume coverage of the left ventricle must be attained [17]. There are two major approaches available for dynamic imaging. One approach uses a MDCT with 256 or 320 detectors and a stationary table. It is necessary that the detector width covers the whole heart. The other approach uses a second-generation DSCT and the scanner's table shuttle mode, which enables whole-heart coverage (73 mm) by moving the table back and forth between two scanning positions. Scanning during the systolic cardiac phase provides some advantages like - sufficient coverage of the whole heart - because the apicobasal length of the heart is shorter and myocardial wall is thicker, length of the systolic phase is relatively constant. Furthermore, images acquired in systole are less susceptible to beam-hardening artifacts, because of the lower amount of contrast material in this phase [8]. The introduction of third-generation DSCT enables a high temporal resolution dynamic myocardial perfusion imaging with an extended coverage of 105 mm. A whole-heart-coverage even in larger dilated hearts can be obtained [16].

There are some limitations of dynamic CT myocardial perfusion imaging like the high radiation dose, the long breath-hold time for whole-heart scanning ($>$ 30 s) and spatial misalignments resulting from table movements [16][8].

2.3 Quantification of CT Myocardial Perfusion

Currently the primary mode for clinical assessment of myocardial perfusion is the qualitative visual assessment. For an accurate assessment of CT myocardial perfusion images, the images have to be acquired during or shortly after peak myocardial contrast enhancement and during a quiescent period of the cardiac cycle. The gray scale of the images has to be optimized for the visualization of low-attenuation myocardial areas which signify perfusion defects. A careful survey of the images should be performed to identify whether any relevant artifacts are present.

Perfusion defects are visually evaluated using the American Heart Association 17-segment model and can be "scored" as transmural ($> 50\,\%$) or non-transmural ($< 50\,\%$), with reversibility graded on a 0 to 3 scale for none, minimal, partial, or complete, respectively.

Additional approaches have been proposed with a 0 to 4 scale: 0 indicates uniform CT attenuation, 1 indicates reduced attenuation of $< 50\,\%$ of the myocardial segment, 2 indicates reduced attenuation involving $> 50\,\%$ of the myocardium, 3 indicates reduced attenuation in 50 - 75 % of the myocardium, and 4 indicates reduced attenuation in $> 75\,\%$ of the myocardium [20].

For the quantification of the myocardial perfusion different methods are available. They can be grouped into nondeconvolution-based and deconvolution-based methods. The theory of these perfusion calculation method is the indicator dilution method. The indicator in this instance is the iodinated contrast medium. There have to be certain fundamental assumptions to be fulfilled which are: complete mixing of the indicator; the volume of indicator injected is negligible; the indicator does not perturb hemodynamic equilibrium; there is no extravascular loss of indicator; the indicator is administrated as a bolus; the contrast density

can be accurately measured [21]. The following two sub-sections give a short overview of the nondeconvolution-based and deconvolution-based methods.

2.3.1 Nondeconvolution-based Methods for Perfusion Calculation

The upslope method, the maximum enhancement method and the full width at half maximum method are three representatives for the nondeconvolution-based method for perfusion calculation. These three methods will be described at present.

Upslope Method

The upslope method is the most commonly used method for a semi-quantitative analysis. This method assumes that there is no venous outflow from the tissue volume under consideration during the time of observation. Hence, this requires a faster contrast agent bolus injection rate in order to approximately fulfill this condition [10]. The upslope method is also called maximum slope method, because the perfusion can be estimated by dividing the maximal slope of the tissue time-concentration curve by the maximum value of the contrast agent concentration in the feeding artery (see figure 2.2) [10]. In the case of myocardial perfusion computation, as shown in equation 2.1, the tissue time-concentration curve corresponds to the myocardial time-concentration curve c_{myo}. The contrast agent concentration in the feeding artery equates to the contrast agent concentration in the ventricle $c_{ventricle}$.

$$MBF = [\frac{\mathrm{d}c_{myo}(t)}{\mathrm{d}t}]_{max} \cdot \frac{1}{[c_{ventricle}(t)]_{max}} \text{ [ml/100g/min]} \tag{2.1}$$

An advantage of the upslope method is the shorter overall acquisition time, because only the upslope of the time-concentration curve is required [10], [17]. A disadvantage of the upslope methode is that it delivers accurate MBF values only if the maximum gradient is reached earlier than the transit time of the tissue [22]. However, if the maximum gradient is reached later, it leads to MBF values that will increasingly be underestimated. The maximum tissue gradient is reached simultaneously with the peak of the arterial input function (AIF) or the ventricle time-attenuation curve, respectively. So the accuracy directly depends on the ratio of the injection time and the tissue transit time [22]. Hence, in high quality CT images this method gives comparable as good results as deconvolution-based approaches. Contrary, like in terms of noise, deconvolution-based methods provide superior results in poor quality CT images [10].

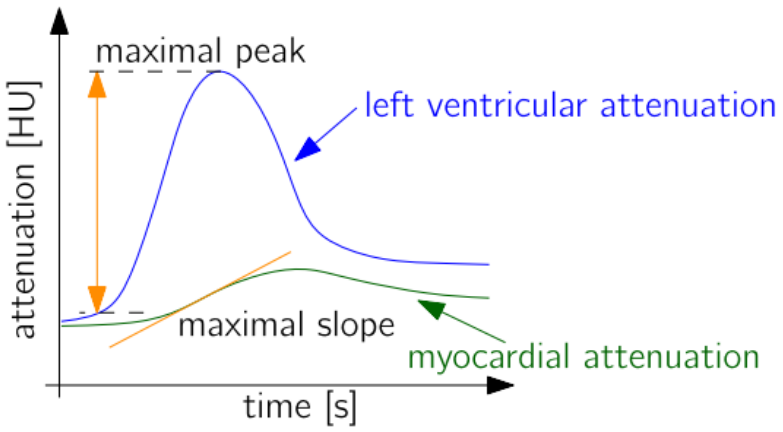

Figure 2.2: Upslope model for myocardial perfusion calculation. Perfusion can be estimated by dividing the maximal slope (orange line) of the myocardial attenuation curve (green) by the maximum value of the contrast agent concentration in the left ventricular attenuation curve (blue) [12].

Maximum enhancement (Mullani-Gould) Method

A similar approach to the upslope method is used by Rumberger [21] who calculates the myocardial perfusion with the modified formula 2.2 from Mullani and Gould [23]:

$$MBF = \frac{C_{PH}}{A_{LV}} \text{ [ml/100g/min]} \tag{2.2}$$

C_{PH} denotes the myocardial opacification peak and A_{LV} is the area under the left ventricular attenuation curve until this peak is reached. The disadvantage of this method are the severe restrictions. An agreement with comparison techniques was achievable only by using a large, relatively arbitrary empirical correction factor [22].

Full Width/Half Maximum Method

The full width at half maximum method has also been mentioned by Rumberger [21]. For this method the time points at which the myocardial curve reaches half maximum value at either side of its peak have to be found. The empirical transit time t_{et} is the timespan between these two time points. Additionally the areas under the myocardial and the ventricular curves, A_{myo} and A_{ventr}, respectively, have to be calculated. Then the perfusion is:

$$MBF = \frac{F}{V} = \frac{A_{myo} \cdot t_{et}}{A_{ventr}} \text{ [ml/100g/min]} \tag{2.3}$$

2.3.2 Deconvolution-based Methods for Perfusion Calculation

The principle of the deconvolution-based methods is that the system response of contrast transport within a tissue is linear and stationary [24]. With this assumptions the contrast concentration curve of the tissue $y(t)$ can be expressed as a convolution of the arterial input function $u(t)$ and an impulse response function $h(t)$ shown in the following equation:

$$y(t) = u(t) * h(t). \tag{2.4}$$

The impulse response function $h(t)$ is a probability density function and can be obtained through a reverse process of deconvolution. The shape of this function is fitted with a mathematical model, because deconvolution is sensitive to noise. The Fermi function is the most commonly used function in this overall process called model-constrained deconvolution [24]. This function was introduced by Axel [25] and was chosen based on the perception that its shape resembles the expected shape of an impulse response for an intra-vascular tracer. The mathematical formulation is presented in [26]:

$$R_F(t) = \frac{A}{\mathrm{e}^{\left(\frac{t-\mu}{k}\right)} + 1} \tag{2.5}$$

where the parameter t represents time, and the parameters μ, k, and A, represents shape parameters which have no physiological interpretation. The parameter μ defines the width of the initial plateau before the function decays at a rate set by the parameter k. Only the amplitude of $R_F(t = 0)$ corresponds to the blood flow according to the Central Volume Theorem. Figure 2.3 illustrates the Central Volume Principle [26].

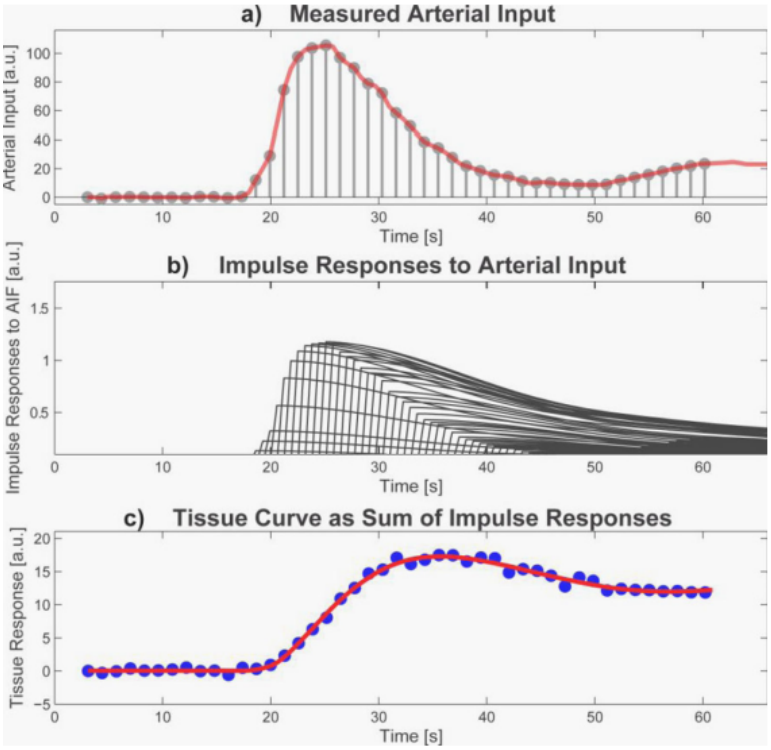

Figure 2.3: Measured arterial input, impulse responses to arterial input and the tissue curve as a sum of impulse responses. a) To illustrate the Central Volume Principle the arterial input can be considered as a sequence of impulses (gray lines with circles at top), whose amplitudes reproduce the measured arterial input (red line). b) Each of the impulses in the arterial input generates an impulse response in the tissue. These are all identical, however, each is scaled according to the amplitude of the corresponding impulse in the arterial input. Each impulse response is shifted so that its start coincides with the location of the arterial input pulse. c) The sum of the contributions from each impulse response correspond to the total tissue response. This sum is the numerical equivalent of the convolution integral of the arterial input with the impulse response. For deconvolution one tries to reverse the above process. The form of the impulse response can be estimated from the signal curves in (a) and (b) [26].

2.4 Image Quality in CT

Image quality in CT depends on 4 basic factors: image contrast, spatial resolution, image noise and artifacts [27]. One definition for image quality is that it is a nonspecific and subjective measure of the readability of a visual image [28]. For a better understanding of the term image quality, this section gives an overview of the basic principles of CT and image reconstruction techniques at the beginning. Next, the image parameters spatial resolution, contrast resolution, and temporal resolution are explained. Additionally, the most common types of artifacts which can usually degrade the quality of CT images are discussed. At the end of this section the fundamental dose parameter, dose affecting factors, and dose reduction systems are described.

2.4.1 Basic Principle in Computed Tomography

The following subsection is mainly taken from [29]. The basic principle in computed tomography consists of measuring the spatial distribution of a physical quantity to be examined from different directions and to compute superposition-free images from these data. The intensity I of X-rays attenuated by the object and the primary intensity I_0 has to be measured in CT to calculate the attenuation value along each ray from source to detector, called linear attenuation coefficient μ(x,y). The physical quantity μ is not very descriptive and strongly depends on the used spectral energy. To directly compare images obtained by scanners with different voltages and filtration, the computed attenuation coefficient is displayed as a so-called CT value relative to the attenuation of water μ_{water}.

CT values, often also referred to as CT numbers, are specified in Hounsfield units (HU). For an arbitrary tissue T with attenuation coefficient μ_T the CT value is defined as

$$CT\ value = (\mu_T - \mu_{water})/\mu_{water} \cdot 1000\ [\text{HU}]. \tag{2.6}$$

The CT value of water is 0 HU by definition, air corresponds to a CT value of -1000 HU. These are the two fixed points for the CT value scale, because the CT values of water and air are independent of the energy of the X-rays.

Figure 2.4 displays the CT values and the corresponding tissues. Lung tissue and fat show negative CT values due to their lower density that result in lower attenuation. Muscle, connective tissue and most soft tissue organs exhibit positive CT values. Bone and calcification have higher CT values of typically up to 2000 HU, because of the higher effective atomic number of calcium and the increased density. CT values of bone or contrast media are more strongly dependent on x-ray energy than water, which leads to an increase of CT values with reduced high voltage settings.

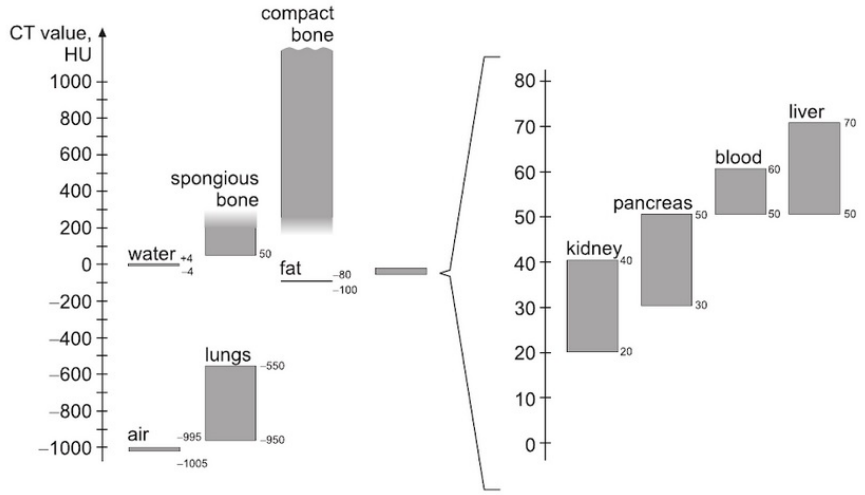

Figure 2.4: Hounsfield Scale. CT values display the attenuation coefficient of a tissue relatively to the μ of water[29].

Although the Hounsfield scale has no upper limit, a range from -1024 HU to +3071 HU is provided for medical scanners. As a result, 4906 ($=2^{12}$) different grey levels are available. Human observers can distinguish at maximum only

about 60 - 80 gray levels. For that reason, the complete grey scale is assigned to the CT value interval of interest only. This is called windowing. Values above the window are displayed as white, values below as black. The desired CT value interval can be adjusted by choosing the right center an width of the window [29].

2.4.2 Image Reconstruction Techniques

Filtered back projection (FBP) has become the standard reconstruction method for diagnostic CT because it is very fast though less than perfect. On the other hand, iterative reconstruction (IR) CT algorithms have their renaissance due to the advances in CT hardware and increases in computing power [30]. These two reconstruction methods are described in more detail in the following subsection.

Filtered Back Projection

FBP is an analytical reconstruction algorithm which is based on the premise that both the measurement process and the projection data are represented by continuous functions. For a simplification of the data acquisition model, the x-ray beam can be thought as collimated to a pencil shape and moved subsequently parallel to a linear x-ray detector array. Next, the x-ray source is rotated by an angle α and the process is repeated. The resulting intensity profiles are measured by the detector and can be mathematically described as an integral function for a certain angle α and a specific linear shift position of the x-ray tube. The reconstruction process can be described as the solution of the resulting integral equations by inversion (back projection)[29][30]. A so-called low-pass blur occurs because of the different numbers of projections passing through the center and periphery of an object, respectively. Therefore, the back projection that describes the propagation of the measured projection data into the image domain is combined with a filter component (eg, Ram-Lak filter).

Further variations of the filter (kernel) can be chosen. They are contingent upon a compromise between spatial resolution and image noise. With increasing compensation of the low-pass blur, the "sharpness" of the image but also the image noise increases. A characteristic of FBP is that sharpness and image noise are directly coupled: that means, the sharper the image, the higher the image noise. The main advantages of FBP consists in its robustness and speed. A major limiting feature is that it fails to account for image noise that results from Poisson statistic variations of the photon number across the image plane. This means that a reduction in radiation dose translates into an increase in image noise. Certain minimal radiation dose requirements need to be fulfilled to generate a diagnostic CT data set, because high image noise interferes with the delineation and low-contrast detectability. Choosing "smoother" kernels for image reconstruction to lower image noise will result in impaired spatial resolution with the use of a conventional FBP technique [30].

FBP has the ability to generate CT studies of adequate image quality in a robust and fast manner [30]. But they can be affected by high image noise, artifacts, or poor low-contrast detectability in specific clinical scenarios. Data acquisition with reduced tube output or CT imaging of obese patients is often compromised by high image noise; high density structures, such as calcifications or stents result in blooming artifacts; metallic implants or bone structures might lead to severe streak artifacts [30].

Iterative Reconstruction

IR methods have re-emerged in transmission x-ray computed tomography. The concept of iterative reconstruction was already established in single photon emission CT in the 1960s and also used in the first transmission CT efforts in the early 1970s. In the first clinical CT products relatively small amounts of measured data were generated per scan and reconstructed into crude 128 x

128 image matrices. They were given up because of the higher computational demands of IR compared to analytic methods when the amount of measured data increased. Since large computational capacities in normal workstations are availably nowadays and the ongoing efforts towards lower doses in CT the situation has changed. The commonly used filtered back projection is an analytical algorithm which is based on only a single reconstruction. Because iterative algorithms use multiple repetitions in which the solution converges towards a optimum solution, the computational demands are much higher. Different concepts of IR methods exist. They can be distinguish between pure iterative methods without any modeling, statistical methods with modeling of the photon counting statistics, and model-based methods which go beyond statistical modeling [31].

All IR methods have three major steps in common which are repeated iteratively. Figure 2.5 shows the principle steps of the iterative image reconstruction. In a first step, a forward projection of the volumetric object estimate creates artificial raw data. In a second step, this raw data is compared to a real measured data in order to compute a correction term which, in a last step, is back projected onto the volumetric object estimate. The iteration process can be initiated with an empty image estimate or using prior information like a standard FBP reconstruction or a volume of a similar object. The better the prior images match the final images, the faster the progress converges towards a stable solution. The iterative process ends when either a fixed number of iterations is reached, or the update for the current image estimate is considered small enough or when a predefined quality criterion in the image estimate is fulfilled [31].

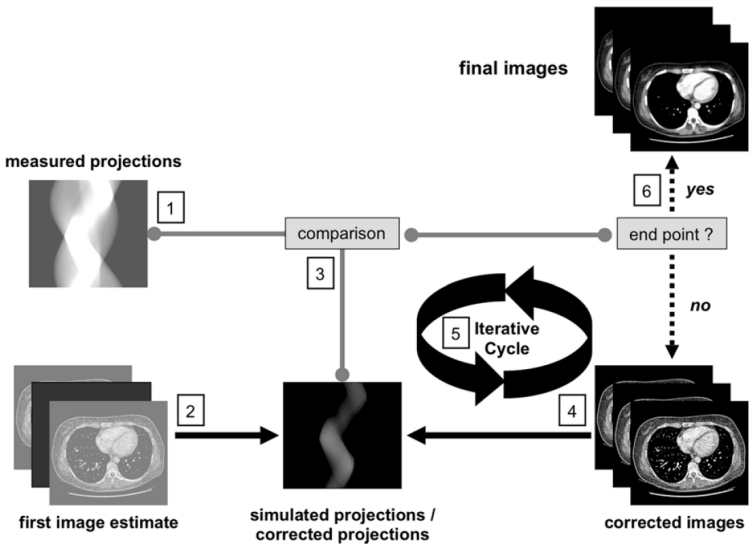

Figure 2.5: Principle steps of iterative image reconstruction. After getting measured projections (1) from the CT acquisition process, a first image (2) can be estimated. Via forward projection a x-ray beam is simulated that acquires simulated projection data. These simulation projection data are then compared (3) with the measured projection data. If there is a discrepancy, the first image estimate is updated (4) depending on the characteristic of the underlying algorithm. This adjustment of image and projection data iterates (5) until a predefined condition is satisfied and the final image (6) is generated [30].

2.4.3 Image Parameters

The following section gives an overview of parameters that influence the image quality like spatial and contrast resolution. Additionally, in the case of imaging the heart, the understanding of the temporal resolution is also very important.

Spatial Resolution

Spatial resolution is the ability of an imaging system to distinguish two adjacent objects in the two spatial dimensions of an image (length and width) from one another. Spatial resolution measures the ability of a system to distinctly delineate

two objects as they become smaller and closer together. The closer they are together with the image still showing them as separate, the better the spatial resolution [28] [32]. Spatial resolution depends on the following parameters that can not be modified [33]:

- focal spot size
- detector width
- minimal slice thickness
- object to detector distance
- matrix size

And on parameters that can be modified in the reconstruction phase [33]:

- reconstruction thickness
- reconstruction increment
- field of view
- convolution kernels

The resolution properties of an imaging system are described by the modulation transfer function (MTF), which describes the percentage of an object contrast that is recorded by the imaging system as a function of its size (spacial frequency) [28].

Contrast Resolution

Contrast resolution of an imaging system determines the contrast detail that can be visibly reproduced when there is a small difference in density relative to the surrounding area, implying that more subtle objects can bee seen on the image.

Contrast resolution is highly degraded by noise. To reliably identify a structure, the signal to noise ratio (SNR) needs to be better than 5:1. The SNR is thus the best descriptor of contrast resolution which is easily determined from measures of regions of interest within the test object and surrounding noise [28][32].

Noise

Noise in CT is the uncertainty in the measurement of the attenuation of an x-ray beam passing through the patient and should be so low as to not influence the presentation of the resultant image. Noise depends on the number of x-ray photons falling on the detector referred to as quantum noise. Quantum noise is the statistical fluctuation or standard deviation of CT numbers of a homogeneous region of interest and is measured by calculating the standard deviation from the mean HU over an area 10 % of the cross-sectional area of a test object. A standard range for noise for spiral CT scanners is $\pm$ 4 HU.

The number of photons reaching the detectors is determined by the milliampere-seconds (mAs) while their energy is determined by the kilo-voltage (kV). A decrease of the mAs and kV leads to increasing image noise but reduces the patients dose [28].

When increasing the kV, the kinetic energy of the accelerated electrons bombarding the anode target also increases. This results in more x-ray photons being generated from the x-ray tube even though tube current remains constant. Therefore, whenever kV is increased this should be compensated by a reduction in mA. The basis in image quality optimization in CT is finding the acceptable amount of noise generated without impairing diagnosis when dose reduction measures are implemented, because a certain amount of noise is always present in an image [28].

Temporal Resolution

A sharp image of an organ in motion can only be obtained, if the acquisition time or speed is less or equal to the speed of the organ. In CT scanners the temporal resolution depends largely on the gantry rotation speed and the geometry of the image reconstruction algorithm, which is dependent on the segments available for the reconstruction of the image. To generate an image, a 180° acquisition is required. This can be obtained from a single cardiac cycle, so-called single segment reconstruction or from several consecutive cardiac cycles which is called multisegmental reconstruction. The image quality is inversely proportional to the speed of the object [33].

2.4.4 Artifacts

The term image artifact is not clearly defined, but artifacts can degrade the quality of CT images. This term is applied to any systematic discrepancy between the CT numbers in the reconstructed image and the true attenuation coefficients of the object. To optimize image quality, the knowledge about how artefacts occur and how they can be prevented or suppressed is necessary [34]. Artifacts can be classified into four broad categories: motion-related artifacts caused by cardiac, pulmonary or other body motion; beam-hardening artifacts caused by metallic implants, severe calcifications, or air bubbles in the pulmonary artery; structural artifacts produced by adjacent contrast material-filled structures and overlaying vessels; and artifacts that result from technical errors or limitations [35].

Motion Artifacts

Motion artifacts can be caused by voluntary and/or involuntary and/or intrinsic motion of the patient or the organ which is being examined.
Patient motion leads to misregistration artifacts, that can be seen as shading

or streaking in the reconstructed image. Voluntary motion can be avoided, but some involuntary motion may not be preventive during body scanning. However, some scanners have special features to minimize the resulting artifacts [34].

Cardiac Motion-related Artifact

Coronary CTA can be obtained by using a ECG-gated reconstruction algorithm, but image quality can still be affected by cardiac motion. The reasons for that is e.g. a heart rate greater than 70 - 75 beats per minute, variations in heartrate during the breathholding, arrhytmia, and unsuitable selection of pitch. These artifacts result in motion blurring or stepladder effects. Blurring takes place when the movement of the cardiac structure is faster than the temporal resolution of the scanner. The reasons can either be a fast heart rate or an unsuitable reconstruction window selection. Therefore, the easiest way to reduce cardiac motion artifacts is to lower the heart rate [35].

Pulmonary and Voluntary Motion-related Artifact

A typical example for a voluntary artifact is the interruption of breath-hold by the patient during the scan phase and so they are generally due to errors or failed compliance by the patient. These artifacts generate clear and severer changes in image quality: on one hand physical motion leads to blurring and intense gaps and overlaps between sections, on the other hand respiratory and voluntary movements causes a phase-missmatch artifact. This is similar to the artifact that is produced by acceleration of the heart rate towards the end of a long breath hold. Therefore, respiratory artifacts can be similar to artifacts which occur when scanning is performed over a relativity long time period. Voluntary motion artifacts are present as stepladder effect in the anterior thoracic wall and along the border of the heart and can be distinguished from the artifacts related to cardiac motion [35].

Partial Volume Effects

Partial volume effect can lead to image artifacts in a number of ways, which are a separate problem from partial volume averaging, because a CT number represents the average attenuation of the material within a voxel.
One type of partial volume effect occurs when a dense object lying off-center sticks out part of the way into the x-ray beam. Because of the divergence of the x-ray beam which increases along the z axis the dense object is "seen" by the detectors, when the tube is pointing from for example left to right, but not seen by the detector when the tube is pointing from right to left. Shading artifacts appear in the image because of the inconsistencies between the views. The best way to avoid partial volume artefacts is to use a thin acquisition section width [34].

Photon Starvation

Photon starvation is a potential source of streaking artifacts. They can occur in highly attenuated areas like the shoulders as shown in figure 2.6. The attenuation is greatest when the x-ray beam is travelling horizontally and insufficient photons can reach the detector. In these angulations the produced projections are very noisy. In the reconstruction process these noisy projections become magnified and result in horizontal streaks in the image. The problem of photon starvation can be overcome by increasing the tube current, but this would lead to an unnecessary increase of dose to the patient. Techniques like automatic tube current modulation and adaptive filtration minimize photon starvation [34].

Figure 2.6: CT image of a shoulder phantom shows streaking artifacts caused by photon starvation [34].

Beam Hardening Artifacts

An x-ray beam consists of individual photons with polychromatic energies. As the beam passes through an object, the lower-energy photons are absorbed more rapidly than the higher-energy photons and so its mean energy increases, it becomes "harder". This effect results in the so-called cupping artefacts and the appearance of streaks and dark bands between dense objects in the image.
Cupping artefacts occur because x-rays passing through the middle portion of a uniform cylindrical phantom are hardened more, because they are passing more material, than those passing through the edges. As the beam becomes harder, the rate at which it is attenuated decreases. This leads to a more intense beam when it reaches the detector than it would be expected if it had not been hardened. The resultant attenuation profile differs from the ideal profile that would be obtained without beam hardening.
Streaks and dark bands can appear in very heterogeneous cross sections between two dense objects in an image. The portion of the beam that passes through both objects at certain tube positions is hardened more than when it passes through one of the objects at other tube positions. This type of artefact can occur in bony regions of the body and in scans where a contrast medium has been used (see figure 2.7) [34].

Examples of dense objects:

- pacemaker leads, metal valvular protheses, metal surgical clips, indicators of the site of bypass grafts (metal clips), metal sternal sutures and coronary stents.
- the presence of calcified atherosclerotic plaque

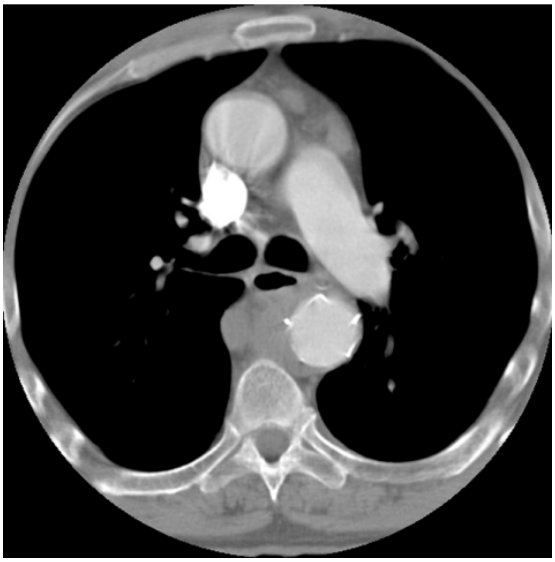

Figure 2.7: CT image shows streaking artifacts due to the beam hardening effects of contrast medium [34].

Manufacturers minimize beam hardening by using built-in features like filtration, calibration correction and beam hardening correction software. A flat piece of attenuating material is used to "pre-harden" the beam, which filters out the lower-energy components before the beam passes through the patient. The edges of the beam, which will pass through the thinner parts of the patient are hardened by an additional "bowtie" filter.
With phantoms in a range of sizes manufacturers calibrate their scanners, the detectors are calibrated with compensation tailored for the beam hardening

effects of different parts of the patient. In clinical practise there may be either a slight residual cupping artefact or a slight "capping" artefact, because patient anatomy never exactly matches a cylindrical calibration phantom. This leads to a higher central CT value due to overcorrection.
Beam hardening correction software uses an iterative correction algorithm which may be applied when images of bony regions are being reconstructed. This helps to reduce the appearance of dark bands in inhomogeneous cross sections.
To avoid beam hardening artefacts it is important to select the appropriate scan field of view to ensure that the scanner uses the correct calibration and beam hardening correction data and, on some systems, the appropriate bowtie filter.

Scanner-based Artifacts

Scanner-based artifacts arise from the incorrect functioning of the scanner at the time of data acquisition or during the reconstruction process [33].

Ring Artifact

Ring artifacts occur if a detector fails to function correctly or is out of calibration with the rest of the system (see figure 2.8). On a third-generation scanner, where the rotating x-ray tube and detector assembly, a consistently erroneous reading at each view of the tube detector system will lead to a circular artifact. The visualization depends on the width of the window and is less evident in wide windows. Ring artifacts (see figure 2.9) are rarely be mistaken with diseases, however, they can reduce the diagnostic quality of an image. This is more likely when central detectors are involved and leads to a dark smudge at the center of the image. Scanner with solid-state detectors (all the detectors are separate entities) are more vulnerable to ring artifacts than scanners with gas detectors (single xenon-filled chamber subdivided by electrodes). Nonetheless, solid-state

detectors are more stable and therefore the preferred technique [34].

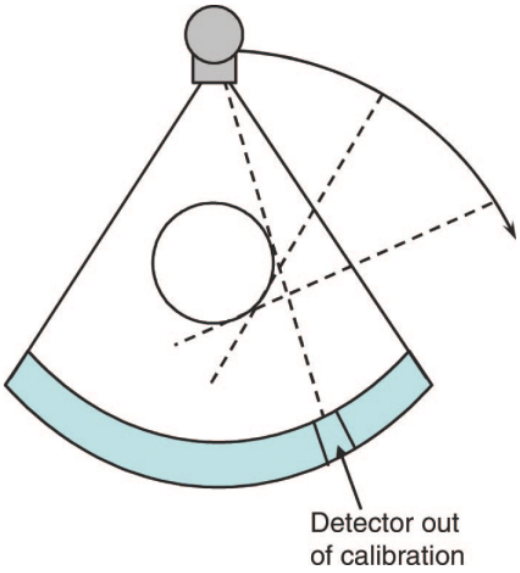

Figure 2.8: Formation of a ring artifact when a detector is out of calibration [34].

Figure 2.9: Image of ring-artifact in PatientID 67

If circular artifacts appear in an image the detector gain needs recalibration or may need repair services. The selection of the correct scan field of view may

reduce the artifact, because calibration data is used that fit more closely to the patient's anatomy. Software that recognizes and corrects detector variations reduces the potential for ring artifacts [34].

Cone Artifact

Cone artifacts occur in helical scanning, when the object changes rapidly in the z-direction, e.g. at the top of the skull, and are worse for higher pitches. The cone-shaped phantom produces artifacts in form of distortion because of the weighting function used in the helical interpolation algorithm. According to projection angles, the image is influenced more by contributions from wider or narrower parts of the cone in front or behind the scan plane predominate, respectively. For that reason, the orientation of the artifact changes depending on the tube position at the center of the image plane. This artifact can easily be misinterpreted as disease e.g. in series of liver images. A minimization of this artifact is possible by using a low pitch, a 180° interpolation rather than a 360° interpolation if there is a choice and thin slice acquisition [33], [34].

Helical (Windmill) Artifact

The helical interpolation process produces a more complicated form of axial image distortion if a multidetector scanner is used than a single-detector scanner. This artifact has a typical windmill-like appearance - radial bands which rotate around high attenuation structures along the volume [33]- because several rows of detectors intersect the plane of reconstruction with each rotation (see figure 2.10). When increasing the pitch, the windmill artifact increases, because a greater number of detectors intersect the reconstruction plane with each rotation. Z-filter interpolation is used to reduce the intensity of windmill artifacts when the image reconstruction width is wider than the detector acquisition width. Another way to reduce this artifact is to use non-integer pitch values relative to detector acquisition width, because z-axis sampling density is optimized for non

integer pitches [34][33].

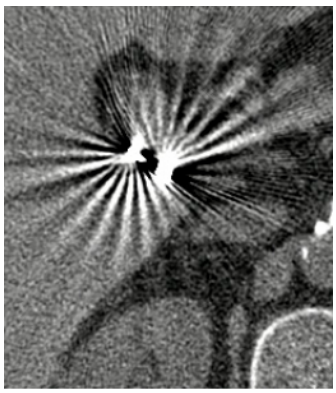

Figure 2.10: CT image shows smoothly undulating streaks around cholecystectomy clips due to windmill artifacts [36].

Cone Beam Effect

The number of detectors has increased and a wider collimation is required so that the X-ray beam becomes more cone-shaped than fan-shaped. The tube and the detectors rotate around the patient, but the data collected by each detector does no longer correspond to an ideal flat plan but rather to a volume contained between two cones. The outcome of this is similar to those caused by partial volume around off-axis objects. Outer detector rows are more affected than inner ones, where the data collected agree more closely to a plane. The severity of this effect is proportional to the number of detector rows. Manufacturers solve this problem by new dedicated reconstruction algorithms [34].

Stair-step and Zebra Artifact

Stair-step artifact occurs around edges of structures in multiplanar and 3D reformatted images when an acquisition is performed with wide collimations and non overlapping reconstruction. This artifact typically does not appear in helical scanning, because it permits reconstruction of overlapping sections. For that, no

additional dose to the patient is necessary when compared to overlapping axial scans. Zebra artifact appear as weak stripes in multiplanar and 3D reformatted images from helical data. The reason for that is that the helical interpolation process leads to noise inhomogeneity along the z-axis. The noise inhomogeneity is worse off-axis therefore, it gets more notably away from the axis of rotation [34].

2.4.5 Radiation Exposure

Radiation dose can be divided into three fundamental dose parameters: absorbed dose; effective dose; equivalent dose. They can be expressed in different units which make it often difficult to compare studies published in the literature [33]. This section gives an overview of these parameters for a better understanding [27].

Absorbed dose

The absorbed dose represents the quantity of energy absorbed per unit of mass. The unit of absorbed dose is Gray (Gy).

Technical measures of the dose output of CT scanners

The CT dose index (CTDI) is a measure of the CT scanner's radiation output normalized to a tube current time product, usually quotes in units of mGy/100mAs. An exposure rate characteristic for a volume exam is always higher than the dose measured for a single-slice exposure because of the scattered radiation contributions from the surrounding media.

The CTDI is measured in polymethyl methacrylate cylinders of 15 cm cm length and diameters of 16 and 32 cm considered representative for a standard head and body section, respectively, with one central and four peripheral bore holes in which a 100 mm long ionization chamber is inserted. The measurement position

can be central (c), peripheral (p) or in air (central in the field of measurement but without a phantom). A weighted CTDI was agreed to take the inhomogeneity of dose distribution into account [37] [38].

$$\mathrm{CTDI_w} = 1/3 \cdot \mathrm{CTDI_c} + 2/3 \cdot \mathrm{CTDI_p} \tag{2.7}$$

The CTDI concept was the standard for acceptance and constancy testing of CT apparatus, since about 2005. When wider CT detectors were introduced with collimation widths nearing or exceeding the 100 mm length of the standard CT ionization chamber, primary radiation is not registered completely and multiple scatter contributions only had a limited extent [38][37].

Technical descriptors of exam-specific dose levels

Dose estimates are intended to provide values in mGy, therefore the applicable normalized CTDI value is multiplied by the mAs product Q used in the exam. To take the spiral CT acquisition into account the division by the pitch factor p is necessary and yields to the so-called 'volume CTDI' or $\mathrm{CTDI_{vol}}$ [38]:

$$\mathrm{CTDI_{vol}} = \mathrm{CTDI_w} \cdot Q/p \ [\mathrm{Gy}]. \tag{2.8}$$

There is a quantity equivalent to $\mathrm{CTDI_{vol}}$ for sequential CT in an analogous manner. In the standard case of contiguous gapless scans $p = 1$ applies directly to equation 2.8; p can be set accordingly for differences in spacing of scans. Statements of $\mathrm{CTDI_{vol}}$ values are obligatory for each CT exam. They have to be provided by the manufactures on the CT scanner console. However, $\mathrm{CTDI_{vol}}$ does not take the patient size, cross-section and the length of the scanned volume into account. More information is provided by the dose-length product (DLP). It is obtained by multiplying the $\mathrm{CTDI_{vol}}$ value with the scan range R [37]:

$$DLP = \mathrm{CTDI_{vol}} \cdot R \; [\mathrm{mGy \cdot cm}] \tag{2.9}$$

The quantity DLP does not provide a dose value, but it is a useful quantity which serves a surrogate for patient dose, which is especially meaningful in efforts to compare dose levels. It became accepted through the establishment of diagnostic reference levels (DRL) [38].

Effective Dose

The effective dose includes the probability of stochastic effects of radiation that depends on the type and energy of radiation. For this correction a so-called radiation weighting factor W_r is multiplied by the dose D. Therefore, the effective dose E is given by the following equation:

$$E = D \cdot W_r \tag{2.10}$$

$W_r = 1$ by definition for X-rays . The unit for effective dose E is Sievert (Sv) which is expressed as Joules per kilogram in SI-units [38].

Equivalent Dose

The probability of the stochastic effects also depends on the organ or tissue irradiated. The organ dose equivalent H_T takes into account that there are differences in the susceptibility of tissues to the effects of radiation. The tissue weighting factor W_T is used to weigh the dose equivalent in a tissue or an organ T. Therefore the equivalent dose can be calculated by:

$$H_T = E \cdot W_T, \tag{2.11}$$

where the unit for H_T is also Sievert (Sv) [39].

Dose Affecting Factors

The background noise in a CT examination corresponds to the graininess overlying the useful information. It is defined as the standard deviation of attenuation values assumed by a pixel in a homogeneous region of known density like water or air. This error can not be eliminated from CT images but it can be statistically limited. Therefore, background noise influences the quality of reconstructed images and reduces the potential diagnostic accuracy of an examination. Equation 2.12 shows the relationship between background noise σ, patient attenuation B, pixel size W, slice thickness used h and the surface dose D_0 [33].

$$\sigma = \sqrt{\frac{B}{W^3 h D_0}} \tag{2.12}$$

Equation 2.12 highlights the strong correlation between dose and image quality, since σ is proportional to $\sqrt{\frac{1}{D_0}}$. This means that a fourfold increase in patient dose is required to halve noise. Another conclusion is that an increase in slice thickness produces a reduction in σ by a factor to the second power. A further scan parameter that influences background noise in MDCT is the spiral pitch. This parameter shows an inversely proportional relationship, because a reduction in table feed leads proportionately to an improvement of the signal-to-noise ratio (SNR), but on the other hand to a significant increase in radiation dose received by the patient.
D_0 depends on operator-dependent parameters as well as scanner specific factors [33].

Operator-dependant Parameters:

- Tube current [mA]
  is a measure of the electric current flowing through the X-ray tube. It can be described as the number of electrons accelerated by the potential difference. The exposure time and the absorbed dose are directly proportional to the

mA.

- Tube voltage [kVp]

  is a measure of the electrical potential between the anode and the cathode. It correlates to the speed to which the photons are accelerated. Tube voltage proportionally influences D_0 approximately by a quadratic factor.

- Spiral pitch

  Under condition that mAs and kVp are constant: spiral pitch is inversely proportional to the absorbed dose. Examinations performed with pitch $<$ 1 produces partially overlapping scans which increase the examination time and radiation exposure.

- Gantry rotation time

  it influences the scan duration ergo the exposure time of the patient.

Scanner specific factors:

- Scanner Geometry

  is a specific property of the used scanner model and cannot be modified by the operator. Recent MDCT scanner have their X-ray tube as close to the patient as possible to reduce the centrifugal forces. Hence, this causes a proportionally increasing exposure of the patient according to the so-called inverse square law, which says that the dose is equal to the inverse square of the distance of the patient from the electron source.

- Geometric Efficiency of the Scanner

  is given by the percentage of photons emitted by the X-ray tube and are effectively used to form the image. It is expressed in terms of the geometric efficiency of the scanner in the z-axis, or width of the radiation dose profile, and the efficiency of the detector array.

Dose Reduction Systems

All the manufacturers of MDCT scanners had the aim to reduce the exposure of the patient while maintaining an adequate level of diagnostic image quality. They use different approaches of automatic dose reduction systems based on either direct modification of the scan parameters, like reduction in mAs, kVp, pitch, etc., or modulation according to individual patient characteristics, like ECG pulsing and automatic exposure control.

The manual reduction of the current intensity (mAs) and/or voltage (kVp) leads to a reduction in the number and mean energy of the photons, respectively, which interact with the detector array. A reduction in voltage reduces the patient exposure and the dose to target organs, however, the use of lower energy photons tends to increase the attenuation values of elements with a high atomic number and with a greater absorption coefficient. This increases the interactions produced by the photoelectric effect. The diagnostic accuracy can be reduced caused by an increase in beam hardening artifacts. To overcome this disadvantage the overall dose can be reduced by using an ECG-controlled modulation of the current emitted by the X-ray tube. The best phase of cardiac cycle for image reconstruction is the mid- to end-diastolic, because in this phase the cardiac motion is at a minimum. For this reason, the X-ray tube current is maximized in the mid- to end-diastole and progressively reduced towards end-systolic during data acquisition. Controversially, recent studies have demonstrate that systole is often the best phase for image reconstruction. That is especially true for patients with elevated heart rates and for the analysis of cardiac volumes and regional wall motion. A different approach uses the automatic regulation of tube current intensities depending on the individual patient characteristics obtained by the initial scout images. The tube current will be lower in subjects with a lower anterio-posterior diameter and greater in obese patients. This leads to optimal image quality [39].

Radiation CT Dose Values for CT-MPI

The contemporary estimated effective dose of coronary CTA and myocardial static CTP imaging typically ranges between approximately 1.5 and 5.0 mSv [8]. Seitun et al. [8] summed up average CT dose values in dynamic CTP imaging from eight human studies. These radiation exposures depend on protocol optimization with an average value of 9.23 mSv (versus 5.93 mSv for static CTP). This is comparable with that of traditional nuclear imaging approaches. The goal is directed towards further reducing radiation exposure while preserving a high diagnostic performance using recent technical innovations like automated tube current modulation and iterative reconstruction [8].

2.5 Image Quality Assessment Tools for CT

This section gives an overview of image quality assessment tools for CT. First, the physical parameters are described, which are assessed by specific quality control tests using phantoms. Next, psychophysical tests are explained which are evaluated with psychophysical phantoms. Finally, observer and diagnostic performance measurements are presented.

2.5.1 Physical Parameters

One definition of image quality in CT refers to how accurately the CT image reproduces the three dimensional attenuation distribution of the X-ray beam through the patient. There are specific quality control tests performed on a regular basis to ensure that the CT unit does not deviate from accepted standards of quality ensuring the systems consistency over time. The International Electrotechnical Commission recommends the expression of the quality of CT images in terms of objective physical tests as measures of diagnostic performance of a system like uniformity, linearity and measures of the detective quantum

efficiency of the imaging system using psychophysical evaluation [28].

Uniformity

CT values are scaled by the Hounsfield unit (HU), while the value of water is 0 HU and the value of air is -1000 HU. These values are checked regularly during normal quality control tests of the CT system to check for uniformity by using an appropriate water phantom. The HU value for water should not differ over time. The accepted tolerance range for different measures over time of the mean CT value of the water phantom is usually 0 ± 4 HU and ± 2 HU for uniformity [28].

Linearity

Linearity is the relationship between the calculated CT number for uniformity and the linear attenuation coefficient of each different element in the scanned object. The different linear attenuation coefficients of tissues within the body are reflected in the corresponding CT values in the image. The phantom used for linearity tests consists of several materials of different compositions and linear attenuation coefficients but with known CT numbers placed in different positions throughout a water phantom. To ensure the accuracy of the CT numbers for each material and primarily for water routine checks and calibrations are necessary. The accepted tolerance range for linearity is ± 5 HU from the known CT numbers of the elements within the phantom [28].

Detective quantum efficiency (DQE)

CT scanning is a digital imaging modality which uses image detectors for the acquisition of image data. An overexposure of the digital image detector can still produce excellent results since the electronics of the system compensate large

fluctuations in exposure. Therefore, a quality control program should be in place to monitor proper exposure levels. DQE is directly related to the exposure necessary to produce good images. Detectors with high DQE need less exposure for adequate signal to noise ratios because they make more efficient use of X-rays. DQE describes the imaging system in terms of noise, resolution and contrast [28]. The DQE as a function of dose (D) and frequency (f) is given by

$$DQE(D, f) = \frac{(\text{large area signal})^2 MTF(f)^2}{NPS(D, f) SNR_{in}^2} \tag{2.13}$$

where MTF is the Modulation Transfer Function (describing the resolution properties of the system) and NPS is the Noise Power Spectrum (describing the noise properties of the system). The "large area signal" comes from normalising the NPS, and the signal-to-noise ratio squared describes the photon- or energy-weighted variance of the incident beam [40].

The physical characteristics of a CT system predict the outcome of the possible quality results of the observer or subjective tests. Evaluation of image quality in radiology is not complete without subjective methods using observer psychophysical measurements [28].

2.5.2 Psychophysical tests

Psychophysical measurements are obtained from the response of an observer to visual stimuli where test images from the psychophysical phantom are evaluated. The quantitative measure of the spatial resolution is tested by line pairs as visual stimulus. Contrast resolution is measured by identifying discs of different densities within a phantom containing cylinders of different attenuation

coefficients. Objective information concerning the image quality of the CT system give the measurements of DQE and MTF. These measurements do not take into account patient related parameters influencing image quality so their effect on diagnosis still has to be investigated. The evaluation of image quality in CT is associated with detecting pathologies therefore it is necessary to evaluate the diagnostic performance of the CT system by measuring the diagnostic accuracy of the images within the clinical setting [28][40].

2.5.3 Observer and Diagnostic Performance

Observer performance measures and diagnostic performance measurements are obtained from images of patients in the clinical settings and/or phantoms. There are several established methods to perform observer and diagnostic performance tests while it is possible to measure image quality in terms of a specific set of criteria [28].
Such methods include those that consider the detection of abnormal conditions (i.e., receiver operating characteristic (ROC) analysis), visual grading analysis (VGA) and alternative forced choice (AFC). Although all of these methods can be valuable in image quality assessment it is necessary to choose the correct tool depending on the research question [41].

Visual grading characteristics (VGC) analysis

Visual grading techniques can be used to evaluate the quality of images by grading the clarity of reproduction of anatomic or pathological structures. The methods are characterised by their simplicity and reliability and can be divided into "visual grading analysis (VGA)" and the "image criteria (IC) study". Bath and Mansson [42] introduced a method called "visual grading characteristic (VGC) analysis". It is a non-parametric rank-invariant statistical method for

statistical analysis of VGA-data.

There are two ways to perform VGA:

- as relative grading
- as absolute grading

For relative visual grading studies there are one or several reference images necessary to which all other test images are compared based on predetermined criteria. The observer compares the display quality of the target structure of the test image with the corresponding landmark of the reference image. To categorize the observer decision a scale with 3, 5, or 7 points is used (e.g. a 5-step scale comparing visibility would appear thus: +2 = much better, +1 = slightly better, 0 = equal, -1 =slightly worse, -2 = much worse).
For absolute visual grading studies there is no reference image used. The observer states his opinion an the visibility of a certain feature using an absolute scale. This consists typically of 4 to 7 points. [41] [43]

VGA-studies can be used to evaluate anatomical or pathological structures and physical quality parameters [43]. They are generally performed in the absence of any disease, pathology, or lesion as these can create non-standard image appearances that are difficult to compare [41]. The assessment of anatomical structures is often based on quality standards which have been established for a variety of examinations (CEC Report EUR 16262 EN for computed tomography) [43].
The results of a VGA study can be summarised in a VGA-score (VGAS):

$$VGAS = \frac{\sum_{O,I} S_C}{N_i N_o} \tag{2.14}$$

where S_C is the given individual score for observer (O) and image (I), N_i is the total number of images, and N_o is the total number of observers [40].

To calculate the significance of differences between different systems in a VGA study the analysis of variance (ANOVA) is used in conjuction with a method for multiple comparisons in order to reduce risk of random significance, e.g. the Newman-Keuls test [40].

Receiver operating characteristic (ROC) analysis

The state-of-the art observer performance methodology today is Receiver Operating Characteristics (ROC) analysis. ROC analysis originates from Signal Detection Theory, where one describes the detection of low contrast signals in a noisy background. In the clinic it is the detection of abnormal cases against the background of normal cases. This method is applicable only to tasks that call for binary decision on the part of the observer: is the image normal or abnormal [40]?

Mansson [40] outlines the following six prerequisites for a successful ROC study:

1. There has to be a clear purpose for the study comparing two or more imaging systems or techniques.

2. The images should faithfully represent the clinical situation. This is usually realised by using anthropomorphic phantoms with simulated pathology or software simulating pathology on images.

3. With a sufficient number of readers, it is possible to evaluate the quality of the images and limit down variations between readers.

4. The true state of each case (image) must be known against which the readers' results are compared. This is easy by using phantom studies but hard in clinical studies. Late follow-up, gold standard, and consensus decisions are common usage.

5. If the lesions are too obvious or too conspicuous the ROC study will become worthless. There have to be borderline cases in the set of images. Again, this is easier in phantom studies than with clinical images.

6. If modalities are compared, the statistical analysis will be strengthened considerably.

There are different ROC methods:

- Localization ROC (LROC)

  The LROC method deals only with no or one lesion per image. The observer is asked to make a localisation decision even if it is given a very confident normal score.

- Free-response ROC (FROC)

  The 'free-response' in the FROC method is the spatial location uncertainty of lesions in a medical image. In an FROC experiment, several lesions may be used in each image. The observers are asked to localize each lesion, and a rating reflecting the observers certainty of the lesion and its location must be given.

- Alternative free-response ROC (AFROC)

  This is an alternative way of analysing FROC data. It uses a false-positive image that produces one or more false positive responses.

- Free-response forced error (FFE)

  In an FFE experiment, the observer has to rank the test structures in decreasing order of confidence until they make an error. A false positive image is caused to be produced. The FFE method can also be used to analyse image sets with only zero or one lesion per image. It could be regarded as an empirical detection accuracy measure independent of any observer performance models. A system is superior, if a greater fraction of lesion is detected with this system before making the false-positive error.

- Differential ROC (DROC)

  This method is used to determine the differences between two modalities and is a common procedure in observer performance tests. It produces the differences between the systems, but no absolute values for single modalities. DROC has a superior statistical power to classic ROC.

3 Methods

This chapter describes the setups for qualitative and quantitative image quality assessment in perfusion calculation, which are applied on axial CT scan images in 14 patients with valvular aortic stenosis.
Quantitative measurements were obtained by using Fiji-ImageJ and Matlab R2016a (Mathworks Inc., Natick, USA). The qualitative image quality was assessed by four radiologists.

3.1 Overview and Workflow

3.1.1 Patients

This study contains 14 patients (3 female and 11 male) with valvular aortic stenosis. They were selected because patients with valvular aortic stenosis have a minor likelihood to have perfusion defects. These patients had undergone their CT scans either in Moscow, Russia (10 patients) or in Tashkent, Uzbekistan (4 patients) between February 21, 2015 and December 26, 2017. The range of the patients age was between 28 and 78 years with an average age at 56.9 years.

3.1.2 Scanning Technique

CT examinations of the myocardium were performed with a Philips iCT 256 scanner after administration of a weight dependent amount (0.5 ml/kg body weight) of an intravenous contrast medium (Iodixanol). The images were dynamically acquired during the first-pass of the contrast medium with scanning parameters optimized for the patients weight (see table 3.1) and reconstructed from the raw data at a 5 mm slice thickness.

Patients Weight [kg]	Tube Voltage [kV]	Exposure [mAs]	Tube Current [mA]
< 70	80	50	276
70 - 90	80	60	331
> 90	100	40	221

Table 3.1: Weight-depending Scan Parameters

The Philips specific iterative reconstruction technique, called iDose, level 6, was used for the reconstruction of the raw data. The scan arc is 240° and the duration of X-ray exposure is 180 ms, while the exposure can be calculated by multiplying the tube current and the exposure time.

3.1.3 Placement of ROIs

The myocardium is divided into five regions as shown in Figure 3.1 to find out if there are differences in myocardial perfusion dependent on the location in the myocardium. The first region (blue) is the septobasal part of the myocardium , the second region (green) is the septoapical part. So, these two regions lie between the right heart and the ventricle. The next three regions of the myocardium are surrounded by the lung: Region three lies apical (red), region four lateroapical (magenta), and region five laterobasal (cyan). The ventricle region (yellow) is located between the septobasal and laterobasal region of the myocardium.
The aforementioned regions (see A.1) were assessed by the radiologists to evaluate the qualitative image quality. Quantitative image quality was evaluated by processing the ROIs in Fiji-ImageJ and Matlab.

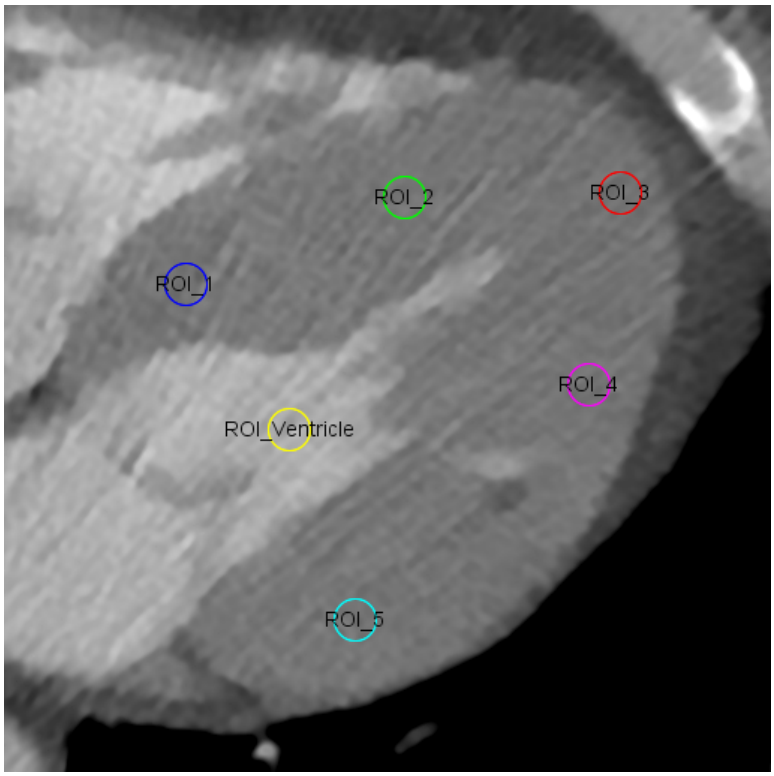

Figure 3.1: Placement of ROIs in Myocardium and Ventricle in Patient ID 122

3.2 Qualitative Assessment

The images were qualitatively assessed by four radiologists with different CT experience (one radiologist 5-8 years, one 13-17 years and two more than 25 years). The radiologists had to evaluate image contrast, image noise and the three following artifacts: streak-artifacts; ring-artifacts; motion-artifacts. The axial reconstructed images were viewed in Fiji-ImageJ as a hyperstack saved in tiff-format. The structure of the questionnaire for the assessment was adopted from [44] and is shown in A.1.

3.2.1 Assessment of Image Contrast

The image contrast or rather the enhancement between the Myocardium ROI 1-5 in the native image and image with maximal contrast was ranked and evaluated using a five-point scale (5 = excellent image contrast, 4 = above average contrast, 3 = acceptable image contrast, 2 = suboptimal image contrast, and 1 = very poor contrast).

3.2.2 Assessment of Image Noise

The subjective image noise for the Ventricle ROI and for Myocardium ROI 1-5 was assessed using a five-point scale (5 = minimal image noise, 4 = less than average noise, 3 = average image noise, 2 = above average noise, and 1 = unacceptable image noise).

3.2.3 Evaluation of Artifacts

The evaluation of artifacts was subdivided into the three following types:

Streak-artifacts

The observer had to evaluate the streak-artifacts for the Ventricle ROI and for Myocardium ROI 1-5. Artifacts are graded using a four-point scale: 1 = artifacts affecting diagnostic information, 2 = major artifacts affecting visualization of major structures but diagnosis still possible, 3 = minor artifacts not interfering with diagnostic decision making, and 4 = No artifacts.

If there were any streak-artifacts, the observer had to mark the cause of streak-artifacts for each corresponding ROI. The possible choices for the cause were: right coronary artery (RCA); left anterior descending (LAD); left circumflex (LCX); aortic valve; mitral valve; rib; vertebral body; contrast medium in

aorta; contrast medium in right heart; pacemaker leads; ECG leads; none of the aforementioned.

Ring-artifact

Ring-artifacts seen on the CT scans in the Ventricle ROI and/or in Myocardium ROI 1-5 were graded using a four-point scale: 1 = artifacts affecting diagnostic information, 2 = major artifacts affecting visualization of major structures but diagnosis still possible, 3 = minor artifacts not interfering with diagnostic decision making, and 4 = No artifacts.

Motion-artifact

Motion-artifact seen on the CT scans in the Ventricle ROI and/or in Myocardium ROI 1-5 were graded using a four-point scale: 1 = artifacts affecting diagnostic information, 2 = major artifacts affecting visualization of major structures but diagnosis still possible, 3 = minor artifacts not interfering with diagnostic decision making, and 4 = No artifacts.

3.3 Quantitative Assessment

The open source image processing tool Fiji-ImageJ was used for the quantitative assessment. An axial reconstructed slice of the CT scans nearby the mitral valve was chosen. Five circular ROIs were placed in the regions of the myocardium and one circular ROI in the ventricle as explained in 3.1.3 on page 50 and shown in figure 3.1 to measure the HU values. The image of the first time-frame was assigned to be the native one for the myocardium and the ventricle. The images at maximum contrast for the ventricle and the myocardium have different instances of time, since the maximum of the ventricle appears earlier. A so-called z-plot was produced to find the time-frame at maximum contrast. The z-plot shows the

mean HU value in a ROI over the time.

The measured values for the native and maximum contrast images were: ROI area, ROI mean, ROI standard-deviation (SD), ROI minimum, ROI maximum, ROI skew, image slice, image frame.

3.3.1 Contrast-to-Noise Ratio

The contrast-to-noise ratio (CNR) was calculated using the formula:

$$CNR = \frac{Contrast}{Noise} = \frac{|\mu_{contrast} - \mu_{native}|}{\sqrt{\sigma^2_{contrast} + \sigma^2_{native}}} \tag{3.1}$$

where $\mu_{contrast}$ is the ROI's mean in the contrast image, μ_{native} the ROI's mean in the native image, $\sigma_{contrast}$ the ROI's standard-deviation in the contrast image and σ_{native} the ROI's standard deviation in the native image [45].

3.3.2 Signal-to-Noise Ratio

The signal-to-noise ratio (SNR) was calculated using the formula:

$$SNR = \frac{Signal}{Noise} = \frac{HU_{Mean}}{HU_{SD}} \tag{3.2}$$

where HU_{Mean} is the mean HU-value of the ROI and HU_{SD} is the standard deviation HU-value of the ROI.

3.4 Curve Fitting Assessment

The calculations of image quality parameters for the curve fitting assessment were done in MATLAB. The required functions for these calculations were integrated into an exiting MATLAB-GUI for myocardial perfusion measurement.

This program loads the ventricle and myocardium data from an EXCEL-file. The used dataset is equal to the dataset evaluated as explained in 3.1.3.

3.4.1 Model Functions for Curve Fitting

The following model functions were used for curve fitting. The residual error was calculated for each fit as a parameter for the quality of the fit, thereby specifying the most suitable model function.

Weibull Distribution

The Weibull distribution might be one of the most widely used lifetime distribution models [46]. This distribution is positive only for positive values of the time t, and zero otherwise. For positive values of the shape parameter β and scale parameter α, the weibull distribution is defined by [47]:

$$f(t) = \frac{\beta}{\alpha} \cdot \left(\frac{t}{\alpha}\right)^{\beta-1} \cdot \mathrm{e}^{-\left(\frac{t}{\alpha}\right)^{\beta}} \tag{3.3}$$

Gamma-Variate Function

Thompson Howard K., Starmer C. Frank, Whalen Robert E., *et al.* proposed to model time-concentration curves, which are based on indicator dilution theory, with the gamma variate function. This function is suitable for modelling ventricular and myocardial time-intensity curves during the first pass of the contrast agent [49]. A simplified formulation of the gamma variate has been established by Madsen in 1992 [50]:

$$f(t) = h_{max} \cdot (t_{max})^{-\beta} \cdot t^{\beta} \cdot \mathrm{e}^{\left(\beta - \frac{\beta \cdot t}{t_{max}}\right)} \tag{3.4}$$

where h_{max} is the maximal height of the curve, t_{max} is the time at peak and the parameter β is varied by the fitting algorithm.

Low-Pass of n^{th} Order

Baumgartner, 1998 [51] has already used the low-pass of fourth order, because it can be easily transformed to the Laplace domain. The following formula defines the function in the time domain and its Laplace transformation, respectively.

$$f(t) = at^{(n-1)} \cdot \mathrm{e}^{-tb} \circ\!\!-\!\!\bullet\, F(s) = \frac{6a}{(s+b)^n}, n \in \mathbb{N} \tag{3.5}$$

The two parameter a (gain) and b (decrease) are varied to fit the data in the time domain and in the Laplace domain. Figure 3.2 shows an example for curve fitting with a low-pass model function.

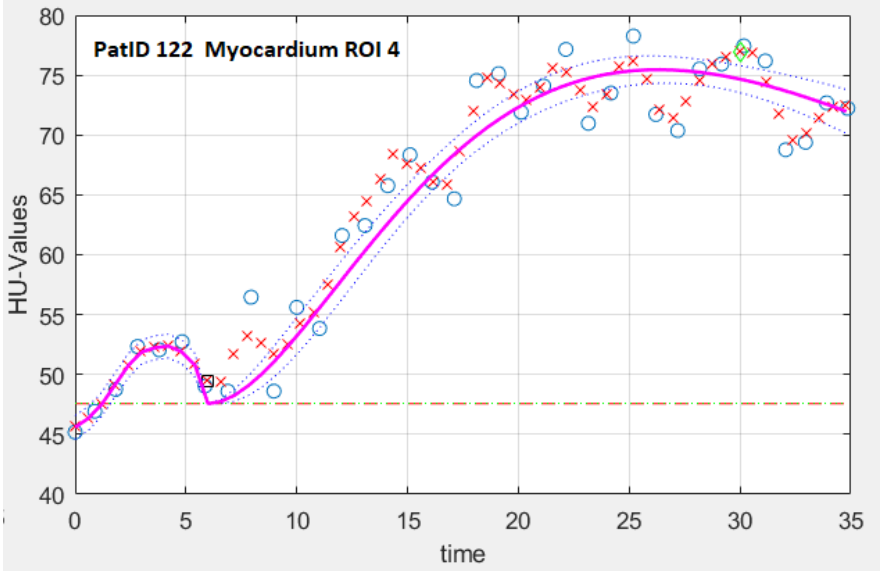

Figure 3.2: Time attenuation curve for the myocardium of Patient ID 122 ROI 4 with a low-pass model function. Blue circles indicate the raw data, red crosses are the interpolated data, the magenta line shows the model curve fit, red dashed line in the right plot shows the myocardial baseline, red dashed line the ventricle baseline. The blue dotted lines shows the 95% confidence interval.

3.4.2 Baseline Detection

The basic formulas of the introduced fitting models have no constant parameter for non-zero baselines. However, the native ventricular and myocardial tissues have CT-values higher than zero. Qanadli, Jouannic, Dehmeshki, *et al.* [52] found that the mean CT-values for the lateral myocardial wall is 39 HU (10 - 82 HU). Before starting the curve fitting process this native baseline-values for the myocardium and ventricular curve have to be subtracted to shift all CT-values against the time axis. As shown in equation 3.13 the perfusion result depends on the peak hight of the ventricular attenuation curve. Therefore, the baseline values for the myocardium and the ventricle should be the same. In noisy datasets or if the scan was started too late it is very difficult to find the real baseline CT-value. A wrong determination of the baseline may result in bad perfusion results. Therefore, finding the right baseline might be a quality criterion for perfusion measurement. The MATLAB code for the baseline detection was already implemented in the provided MATLAB GUI.

3.4.3 Mean Square Error

A further criterion for the goodness of the model curve fit is the so-called estimated mean squared error (MSE) and is given by [53]:

$$MSE = E([T - \Theta]^2) \tag{3.6}$$

where T is the estimator and Θ the measured data. Equation 3.6 can be converted to:

$$MSE = Var(T) + Bias(T)^2 \tag{3.7}$$

As can be seen, the estimated squared error can be written as the sum of the variance of the estimator T and the squared bias of T. The lowest MSE indicates

the fit with the best model curve [53].

3.4.4 Signal Range Raw Data versus Model Data

As explained in chapter 2, perfusion calculation methods require good model fitting of the raw data. In case of data with high noise levels and especially in the case of outliers, the signal range between the raw data and the model data can diverge. The minimum and maximum CT-value of the raw data and the model data were determined using the MATLAB functions $min()$ and $max()$. The signal ranges $Range_{CT-Value}$ for the raw data or the model data were calculated as follows:

$$Range_{CT-Value} = MAX_{CT-Value} - MIN_{CT-Value} \quad [\text{HU}] \tag{3.8}$$

where $MAX_{CT-Value}$ is the maximum CT-value and $MIN_{CT-Value}$ is the minimum CT-value of the raw data or the model data.

3.4.5 Image Quality Parameter Calculation

According to the quantitative assessment of image quality as described in 3.3 the contrast-to-noise ratio and the signal-to-noise ratio of the time-attenuation-curves can be calculated. They can be formulated as follows:

Contrast-to-Noise Ratio of Time-Attenuation-Curves

The contrast-to-noise ratio of the curve was calculated using the formula:

$$CNR_{Curve} = \frac{[HU_{peaktime} - HU_{baseline}]}{noise_{baseline}} \tag{3.9}$$

where $HU_{peaktime}$ is the maximum HU-value of the fitted curve, $HU_{baseline}$ is the

HU-value of the fitted curve baseline and $noise_{baseline}$ is the standard deviation in the baseline.

Signal-to-Noise Ratio of Time-Attenuation-Curves

The assumption for the calculation of the signal-to-noise ratio was that the $Signal$ is defined by the curve of the model data and the $Noise$ is defined by the error between the model data and the raw data.

The signal power P_{Signal} is calculated by equation 3.10 and noise power P_{Noise} by equation 3.11.

$$P_{Signal} = \frac{1}{N} \cdot \Sigma \left(Signal - Signal_{Mean} \right)^2 \tag{3.10}$$

$$P_{Noise} = \frac{1}{N} \cdot \Sigma \left(Noise - Noise_{Mean} \right)^2 \tag{3.11}$$

where $Signal_{Mean}$ is the mean of the $Signal$, $Noise_{Mean}$ is the mean of the $Noise$ and N is the number of data points.

Therefore, the SNR_{Curve} was calculated using the formula:

$$SNR_{Curve} = 10 \cdot log \left(\frac{P_{Signal}}{P_{Noise}} \right) \tag{3.12}$$

3.4.6 Perfusion Calculation

In 2.2 different methods for perfusion calculation are presented. Two of them were chosen to enable a comparison between the perfusion results: the upslope method as a representative for the nondeconvolution-based methods and the fermi method for a representative for the deconvolution-based method. The equations for these perfusion calculation methods are shown again in equation 3.13 and 3.14 to improve readability.

Upslope Method

$$MBF = [\frac{\mathrm{d}c_{myo}(t)}{\mathrm{d}t}]_{max} \cdot \frac{1}{[c_{ventricle}(t)]_{max}} \text{ [ml/100g/min]} \tag{3.13}$$

where c_{myo} corresponds to the myocardial time-concentration curve and $c_{ventricle}$ to the contrast medium concentration in the ventricle.

Fermi Method

$$R_F(t) = \frac{A}{\mathrm{e}^{\left(\frac{t-\mu}{k}\right)} + 1} \tag{3.14}$$

where the parameter t represents time, and the parameters μ, k, and A define the shape of the model function.

3.5 Statistical Evaluation

The data of the image quality parameters was stored in an Excel-file and imported into Matlab. The Likert-scales for observer assessment were calculated an visualized in Excel. The boxplots and regression lines were calculated and visualized in Matlab.

The statistically significance calculations were also done in Matlab. Therefore, a Kruskal-Wallis test was performed as to decide if the data set of each ROI corresponds to the same distribution (test of the null hypothesis). The alternative hypothesis is that the data set of the ROI's correspond to different distributions [54].

4 Results

The focus on this work lies on image quality evaluation of dynamic CT scans for myocardial perfusion measurement. These axial CT scans were reconstructed from the raw data set and there was no further image processing applied like temporal or spatial corrections. The left heart was divided into five different myocardium ROIs and one ventricle ROI, as described in chapter 3.1.1. Each of these ROIs were evaluated regarding native/contrast enhanced signal intensity, native/contrast enhanced signal noise, native/contrast enhanced SNR, and CNR, as the quantitative image quality parameters. For the qualitative evaluation, observer assessed the aforementioned ROIs in relation to contrast enhancement, noise, and artifacts. The detailed evaluation of streak-artifacts and their causes, as well as motion- and ring-artifacts, were done. The last part of this section presents the results for MSE, SNR, and CNR in the curve fitting which were evaluated by using the upslope method.

4.1 Perfusion Calculation

Figure 4.1 visualizes the results for the myocardial perfusion evaluation for the upslope and the fermi method side by side. The results for the upslope method in table 4.1 show that, Myocardium ROI 1 has the lowest range (67.56 ml/100g/min), the lowest median (76.74 ml/100g/min) and the lowest IQR (37.62 ml/100g/min). The highest range (449.75 ml/100g/min) can be found in ROI 3. ROI 5 has the highest median at 100.78 ml/100g/min and the highest IQR at 73.18 ml/100g/min. Outlier can be found in ROI 3 and ROI 5. There was no statistically significant difference between the MBF in the Myocardium ROIs (p-value=0.156) for a 1 % significance level for the upslope method.

The results for the fermi method displayed in table 4.2 were that, ROI 5 has the highest range at 356.73 ml/100g/min, the highest median at 123.53 ml/100g/min and the highest IQR at 75.74 ml/100g/min. ROI 3 shows the lowest median at 79.13 ml/100g/min and the lowest IQR at 30.73 ml/100g/min. The lowest range (74.99 ml/100g/min) was found in ROI 1. Outlier was found in ROI 2, ROI 3 and ROI 5. There was no statistically significant difference between the MBF in the Myocardium ROIs (p-value=0.034) in a 1 % significance level for the fermi method. Table 4.3 summarizes the mean and standard-deviation of the perfusion results for the upslope and fermi method. Figure B.30 - B.34 in the appendix show the correlation between the upslope and fermi method for each ROI.

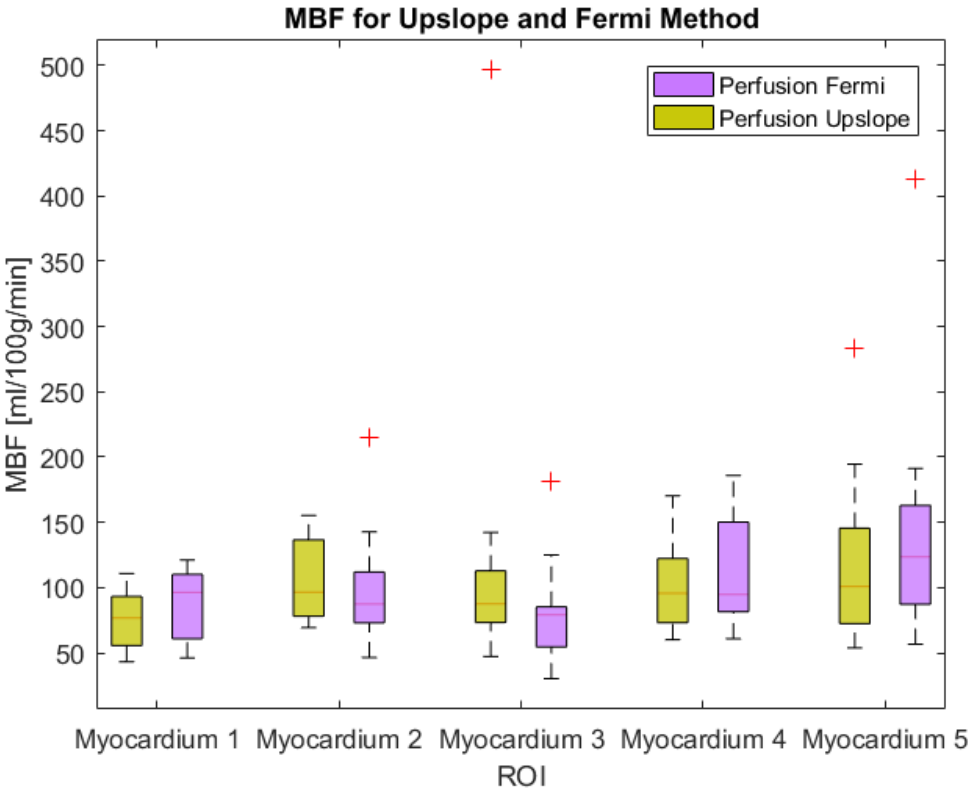

Figure 4.1: Boxplot of the myocardial perfusion calculation results using Upslope and Fermi Method

Table 4.1: Result of the boxplot for myocardial perfusion using the upslope method. Min = minimum value, Max = maximum value, Range = maximum value - minimum value, Q_25 = 25th-quartile, Median = median of the values, Q_75 = 75th-quartile, IQR = interquartile-range. All values in [ml/100g/min].

ROI	**Min**	**Max**	**Range**	**Q_25**	**Median**	**Q_75**	**IQR**
Myocardium 1	43.13	110.69	67.56	55.51	76.74	93.14	37.62
Myocardium 2	69.29	155.28	85.99	77.98	96.52	136.56	58.58
Myocardium 3	47.15	496.90	449.75	73.29	87.46	112.84	39.55
Myocardium 4	60.06	170.27	110.22	73.10	95.54	122.24	49.14
Myocardium 5	53.68	282.73	229.05	72.37	100.78	145.55	73.18

Table 4.2: Result of the boxplot for myocardial perfusion using the fermi method. Min = minimum value, Max = maximum value, Range = maximum value - minimum value, Q_25 = 25th-quartile, Median = median of the values, Q_75 = 75th-quartile, IQR = interquartile-range. All values in [ml/100g/min].

ROI	**Min**	**Max**	**Range**	**Q_25**	**Median**	**Q_75**	**IQR**
Myocardium 1	46.10	121.09	74.99	60.81	96.31	110.14	49.32
Myocardium 2	46.38	215.49	169.11	72.93	87.33	111.86	38.94
Myocardium 3	30.16	181.39	151.23	54.43	79.13	85.16	30.73
Myocardium 4	60.80	185.83	125.03	81.48	94.73	150.19	68.71
Myocardium 5	56.64	413.37	356.73	87.13	123.53	162.87	75.74

Table 4.3: Mean and Standard-deviation (SD) of the MBF for Upslope and Fermi Method. All values are given in [ml/100g/min].

	MBF Upslope		**MBF Fermi**	
	Mean	SD	Mean	SD
Myocardium 1	76.12	22.81	86.16	26.78
Myocardium 2	106.58	31.43	97.47	43.26
Myocardium 3	118.70	111.53	80.49	36.92
Myocardium 4	102.92	33.87	110.81	41.68
Myocardium 5	118.44	63.10	140.21	88.27

4.2 Image Signal Intensity

The image signal intensity corresponds to the mean value in the measurement of the CT value within the ROI. Figure 4.2 shows the boxplots of the signal intensities in the five myocardium ROIs for all 14 patients. The intensities at the first time step of the dynamic CT acquisition were assigned to be the native image signal intensity. The CT-values for the signal intensity of contrast enhanced images are also shown in Figure 4.2. These were measured at the time step at maximum contrast enhanced ROIs in the myocardium. Due to the higher signal intensity in the contrast enhanced ventricle, the ventricle ROI was excluded in the native and contrast enhanced boxplots to make the results better comparable for the myocardium ROIs. The average CT-value for the native signal intensity was 53.45 $\pm$ 10.95 HU and for the contrast enhanced signal intensity 124.08 $\pm$ 22.11 HU. Table 4.4 shows the corresponding values of the results for the native images visualized in figure 4.2. ROI 3 has the lowest median (49.115 HU) and ROI 1 the highest median (57.605 HU). ROI 4 has the lowest range (17.54 HU) and the lowest IQR (8.1 HU), ROI 5 has the highest range (51.17 HU) and the highest IQR (13.76 HU) of the myocardium. The ventricle

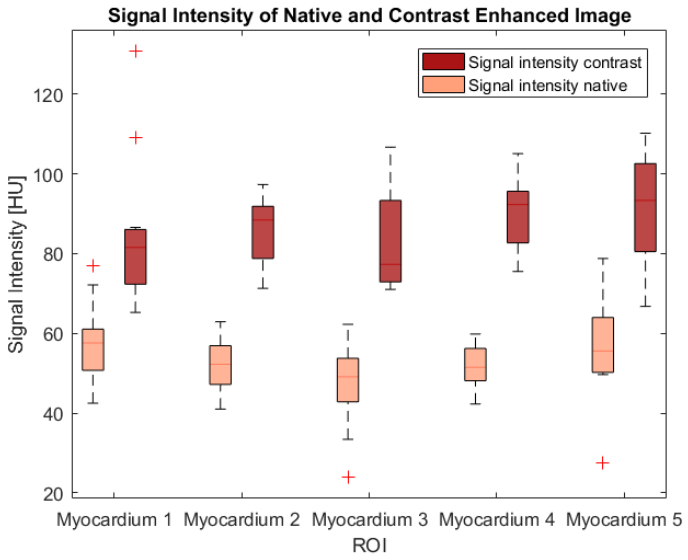

Figure 4.2: Boxplot of the Signal Intensity in the native and contrast enhanced image for each Myocardium ROI

ROI show higher ranges (54.4 HU) and IQR (26.93 HU) than the myocardium. Outlier can be found in the native images in ROI 1, ROI 3, and ROI 5. The results of the boxplot for the contrast enhanced image in figure 4.2 are shown in table 4.5. In the contrast enhanced image ROI 3 has the lowest and ROI 5 the highest median at 77.285 HU and 93.31 HU, respectively. The lowest IQR can be found in ROI 4 at 12.95 HU and the highest IQR in ROI 5 at 22.07 HU. The highest range (65.53 HU) in the contrast enhanced image can be found in ROI 1 due to the outlier. There are no statistical significant differences in the ROIs of the native image (p-value=0.0574) nor in the contrast enhanced ROIs of the myocardium (p-value=0.1588) on a 1 % significance level.

Table 4.4: Result of the boxplot for signal intensity of native images. Min = minimum value, Max = maximum value, Range = maximum value - minimum value, Q_25 = 25th-quartile, Median = median of the values, Q_75 = 75th-quartile, IQR = interquartile-range. All values in [HU].

ROI	**Min**	**Max**	**Range**	**Q_25**	**Median**	**Q_75**	**IQR**
Myocardium 1	42.5	77.06	34.56	50.74	57.605	61.07	10.33
Myocardium 2	41.03	62.9	21.87	47.18	52.25	56.91	9.73
Myocardium 3	23.95	62.25	38.3	42.84	49.115	53.76	10.92
Myocardium 4	42.29	59.83	17.54	48.13	51.485	56.23	8.1
Myocardium 5	27.61	78.78	51.17	50.23	55.56	63.99	13.76
Ventricle	34.58	88.98	54.4	40.25	48.425	67.18	26.93

Table 4.5: Result of the boxplot for signal intensity of contrast enhanced images. Min = minimum value, Max = maximum value, Range = maximum value - minimum value, Q_25 = 25th-quartile, Median = median of the values, Q_75 = 75th-quartile, IQR = interquartile-range. All values in [HU].

ROI	**Min**	**Max**	**Range**	**Q_25**	**Median**	**Q_75**	**IQR**
Myocardium 1	65.24	130.77	65.53	72.32	81.55	86.04	13.72
Myocardium 2	71.3	97.29	25.99	78.78	88.41	91.84	13.06
Myocardium 3	71.02	106.67	35.65	72.9	77.285	93.31	20.41
Myocardium 4	75.51	105.06	29.55	82.67	92.285	95.62	12.95
Myocardium 5	66.76	110.15	43.39	80.49	93.31	102.56	22.07
Ventricle	237.87	494.54	256.67	243.48	298.24	331.72	88.24

4.3 Image Noise

The quantitative image noise for the native and contrast enhanced image was evaluated by the standard deviation of the signal intensity. The qualitative assessment contains the evaluation of image noise and image artifacts. Image artifact assessment was subdivided into streak-artifacts, ring-artifacts and motion-artifacts. For the determination of the streak-artifacts, a list of possible causes were prepared in the questionnaire.

4.3.1 Quantitative Assessment of Image Noise

Figure 4.3 shows the boxplot for the comparison of the noise in the native and the contrast enhanced images for each of the five myocardium ROIs and the ventricle. The corresponding results of the boxplot for the noise in the native image are shown in table 4.6. The results for image noise in the native image show that ROI 2 has the lowest median at 13.18 HU and the highest range at 23.25 HU. ROI 3 shows the lowest range (14.88 HU) and the lowest IQR (5.54 HU). ROI 1 has the highest median at 16.51 HU. The highest IQR can be found in ROI 5 at 10.41 HU.

In the boxplot for the image noise in the contrast enhanced image, one outlier can be observed in myocardium ROI 2. Additionally, ROI 2 has the highest range at 32.21 HU. The highest IQR can also be found in ROI 2 (9.65 HU). The lowest IQR of the noise in the contrast enhanced image shows ROI 3 (6.08 HU). The lowest median is 13.905 HU and can be found in ROI 4, the highest median in ROI 5 (17.825 HU). The corresponding results of the boxplot for the noise in contrast enhanced images can be found in table 4.7. There were no statistically significant differences in both the noise of the native (p-value=0.6105) and the noise in the contrast enhanced image (p-value=0.817) on the 1 % significance

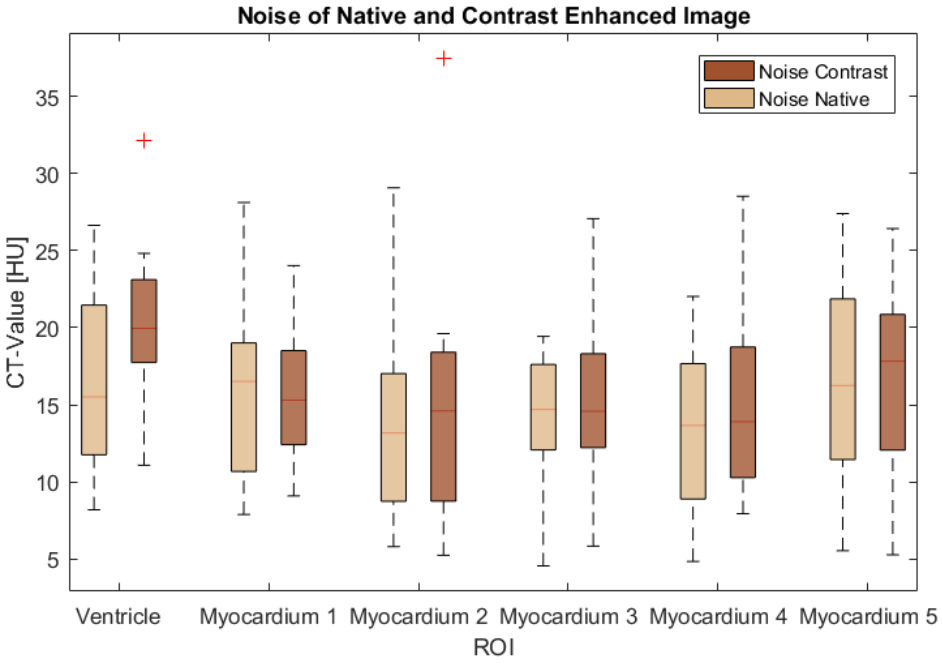

Figure 4.3: Boxplot of the Noise in the native and contrast enhanced Images

level.

Table 4.6: Result of the boxplot for image noise in the native images. Min = minimum value, Max = maximum value, Range = maximum value - minimum value, Q_25 = 25th-quartile, Median = median of the values, Q_75 = 75th-quartile, IQR = interquartile-range. All values in [HU].

ROI	**Min**	**Max**	**Range**	**Q_25**	**Median**	**Q_75**	**IQR**
Myocardium 1	7.89	28.11	20.22	10.68	16.515	19.01	8.33
Myocardium 2	5.81	29.06	23.25	8.75	13.18	17.02	8.27
Myocardium 3	4.56	19.44	14.88	12.08	14.70	17.62	5.54
Myocardium 4	4.85	22.02	17.17	8.90	13.66	17.67	8.77
Myocardium 5	5.55	27.39	21.84	11.46	16.255	21.87	10.41
Ventricle	8.20	26.63	18.43	11.76	15.51	21.46	9.70

Table 4.7: Result of the boxplot for image noise in contrast enhanced images. Min = minimum value, Max = maximum value, Range = maximum value - minimum value, Q_25 = 25th-quartile, Median = median of the values, Q_75 = 75th-quartile, IQR = interquartile-range. All values in [HU].

ROI	**Min**	**Max**	**Range**	**Q_25**	**Median**	**Q_75**	**IQR**
Myocardium 1	9.1	24.02	14.92	12.42	15.305	18.52	6.1
Myocardium 2	5.25	37.46	32.21	8.76	14.6	18.41	9.65
Myocardium 3	5.84	27.07	21.23	12.23	14.58	18.31	6.08
Myocardium 4	7.95	28.51	20.56	10.28	13.905	18.75	8.47
Myocardium 5	5.28	26.42	21.14	12.07	17.825	20.86	8.79
Ventricle	11.09	32.12	21.03	17.74	19.95	23.11	5.37

4.3.2 Observer Assessment of Image Noise

Figure 4.4 shows the histogram of the results for noise assessment by observers for all patients. The following list shows the results in a descent order of their incidence:

- 'average image noise' with n=123 (36.61 %) observations.
- 'above average image noise' with n=98 (29.17 %) observations.
- 'less than average image noise' with n=49 (14.58 %) observations.
- 'minimal image noise' with n=45 (13.39 %) observations.
- 'unacceptable image noise' with n=21 (6.25 %) observations.

Figure 4.5 shows the Likert scale of the observer assessment for each ROI. There is no significant difference in the observer assessment of noise for each ROI but the bars are shifted a little bit more to the 'above image noise' direction.

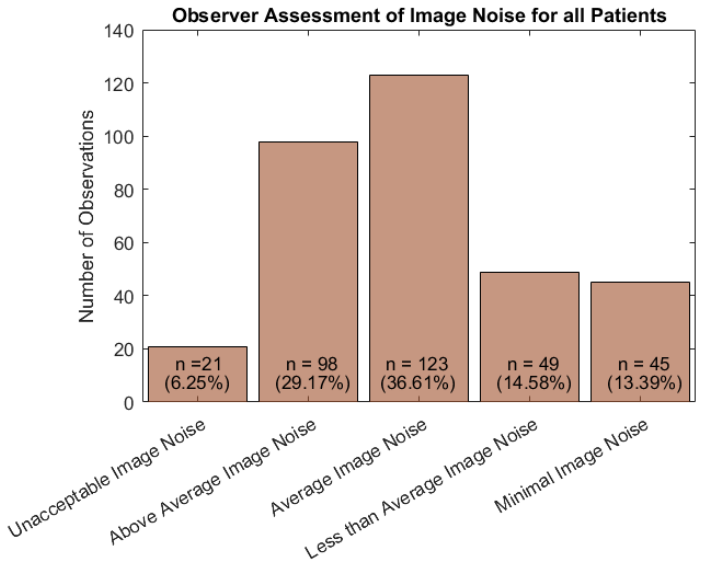

Figure 4.4: Histogram of Noise Assessment by Observers

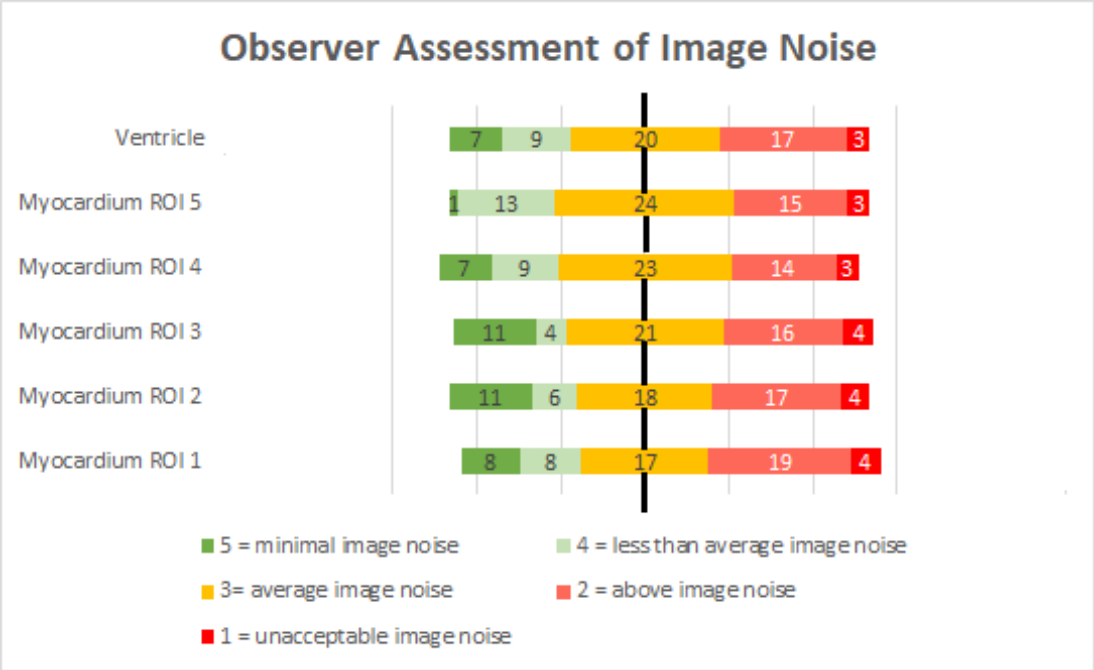

Figure 4.5: Likert Scale for noise observer assessment for all ROIs. Image Noise was graded using a five-point scale: 5 = minimal image noise, 4 = less than average noise, 3 = average image noise, 2 = above average noise, and 1 = unacceptable image noise. The numbers in the bars indicate the number of observations

4.4 Artifacts

Artifacts may be the reason for image noise. Therefore, the observer assessment for streak-artifacts, motion-artifacts and ring-artifacts will be shown next.

4.4.1 Streak-artifacts

Figure 4.6 shows the histogram for streak-artifact observations for each ROI in all patients. The following list shows the results in a descent order of their incidence:

- 'minor artifacts' with n=112 (33.33 %) observations.
- 'major artifacts' with n=108 (32.14 %) observations.
- 'no artifacts' with n=86 (25.6 %) observations.
- 'artifacts affecting diagnostic information' with n=21 (8.93 %) observations.

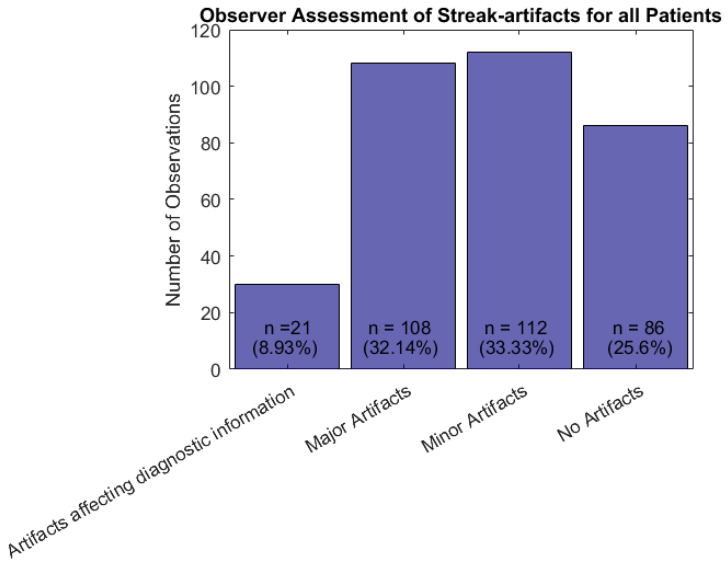

Figure 4.6: Histogram of Streak-artifact Assessment by Observers for all Patient

Figure 4.7 shows the Likert scale of the streak-artifact assessment by the observers. Streak-artifacts have the least impact on Myocardium ROI 5, followed

by Myocardium ROI 4 and the Ventricle. The impact of streak-artifact on Myocardium ROI 1 and ROI 2 are very similar and observer assessed them a little bit more shifted into the minor artifacts direction. Only Myocardium ROI 3 is shifted to the major artifacts direction and is therefore the ROI which is influenced at most by streak artifacts.

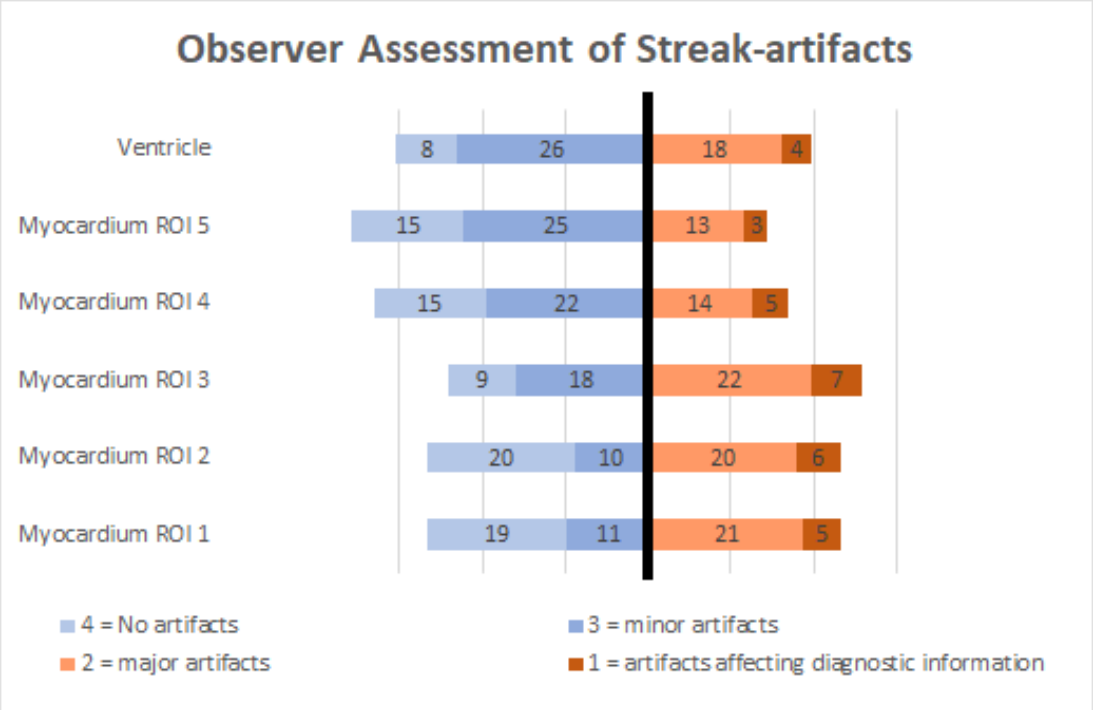

Figure 4.7: Likert scale of the Streak-artifact Observer Assessment for all ROIs. Artifacts were graded using a four-point scale: 1 = artifacts affecting diagnostic information, 2 = major artifacts affecting visualization of major structures but diagnosis still possible, 3 = minor artifacts not interfering with diagnostic decision making, and 4 = No artifacts. The numbers in the bars indicate the number of observations.

4.4.2 Causes of Streak-artifacts

The causes of streak-artifacts for all patients are visualized in Figure 4.8. The following list shows the result in a descent order of their incidence:

- The vertebral body (29 %)
- The aortic valve (22 %)
- None of the default origins (19 %)
- The mitral valve (9 %)
- The contrast medium in the right heart (8 %)
- Contrast medium in the aorta; rib; RCA; LAD; ECG leads (2 %)
- Pacemaker leads; no artifact (1 %)

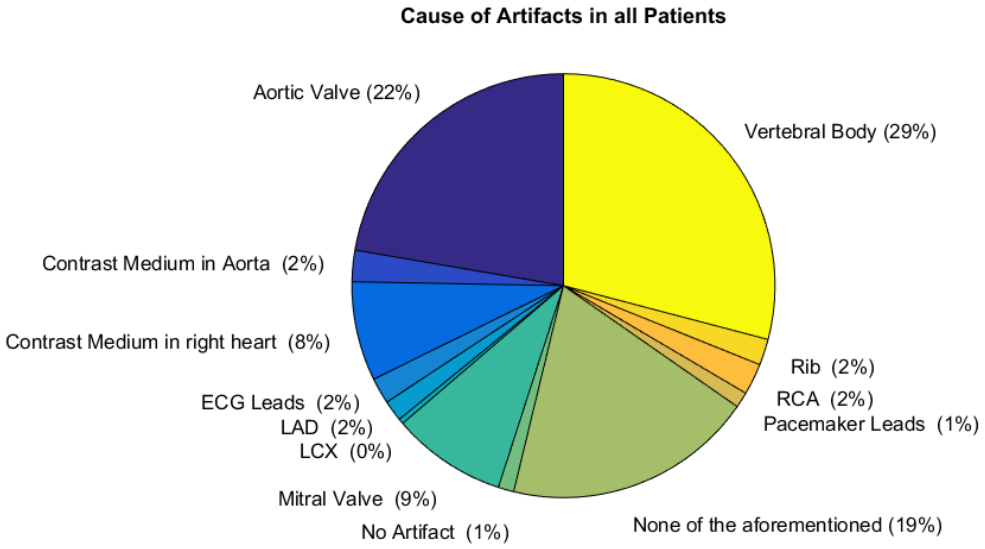

Figure 4.8: Pieplot for the causes of Streak-artifacts for all Patients

The pieplots for each myocardium ROI and the ventricle ROI are displayed in the appendix in B.1 - B.6.

4.4.3 Motion-artifacts

Figure 4.9 shows the histogram of the motion-artifact assessment for all patients and can be listed in a descent order of their incidence as follows:

- 'no artifacts' with n=279 (36.61 %) observations
- 'minor artifacts' with n=42 (12.5 %) observations.
- 'major artifacts' with n=10 (2.98 %) observations.
- 'artifacts affecting diagnostic information' with n=5 (1.49 %) observations.

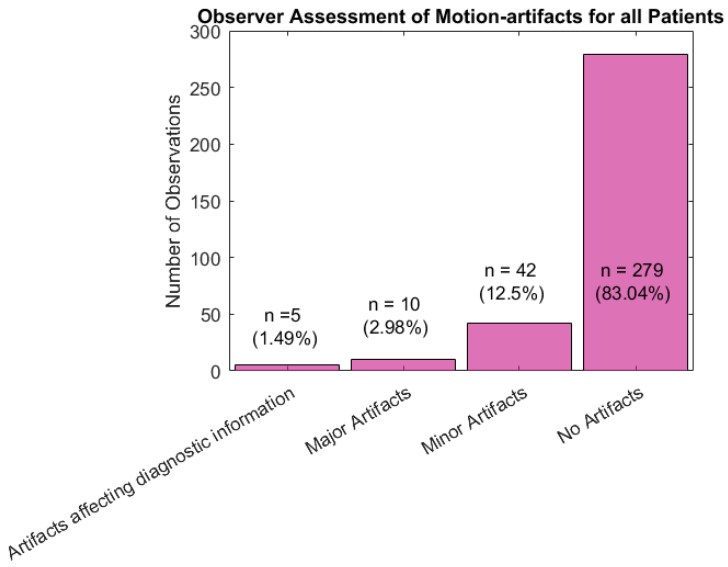

Figure 4.9: Histogram of Motion-artifact Assessment by Observers for all Patient

Figure 4.10 shows the Likert scale for the assessment of motion-artifact by observers. The observer mainly evaluated that in the most ROIs no motion-artifacts are recognisable. Some ROIs were assessed to show minor motion-artifacts. Only a few observations of major motion-artifacts or artifacts affecting diagnostic information have been evaluated.

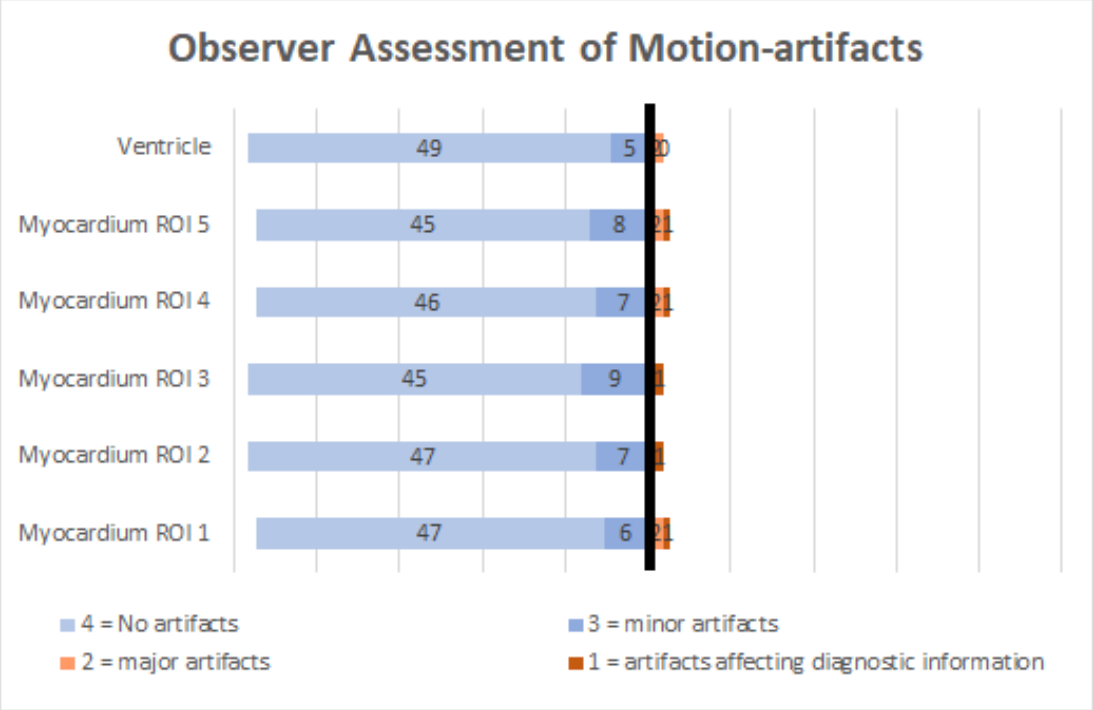

Figure 4.10: Likert scale of the Motion-artifact Observer Assessment for all ROIs. Artifacts were graded using a four-point scale: 1 = artifacts affecting diagnostic information, 2 = major artifacts affecting visualization of major structures but diagnosis still possible, 3 = minor artifacts not interfering with diagnostic decision making, and 4 = No artifacts.

4.4.4 Ring-artifacts

Figure 4.11 shows the histogram of the ring-artifact assessment by the observer for all patients and can be listed in a descent order of their incidence as follows:

- 'no artifacts' with n=284 (1 %) observations
- 'minor artifacts' with n=37 (11.01 %) observations.
- 'major artifacts' with n=11 (3.27 %) observations.
- 'artifacts affecting diagnostic information' with n=4 (1.19 %) observations.

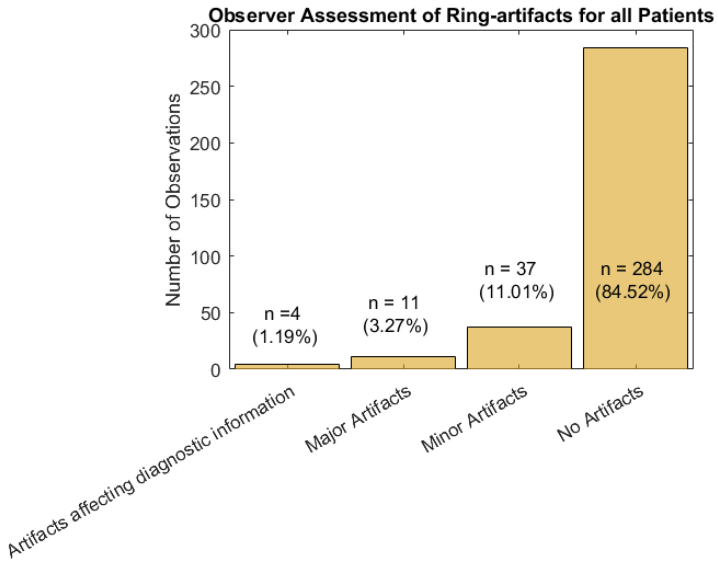

Figure 4.11: Histogram of Ring-artifact Assessment by Observers for all Patient

Figure 4.12 shows a Likert scale for the ring-artifact assessment. The most ring-artifacts appear in the ROI 1 and the ventricle. They do not appear in ROI 2, ROI 3 and ROI 4.

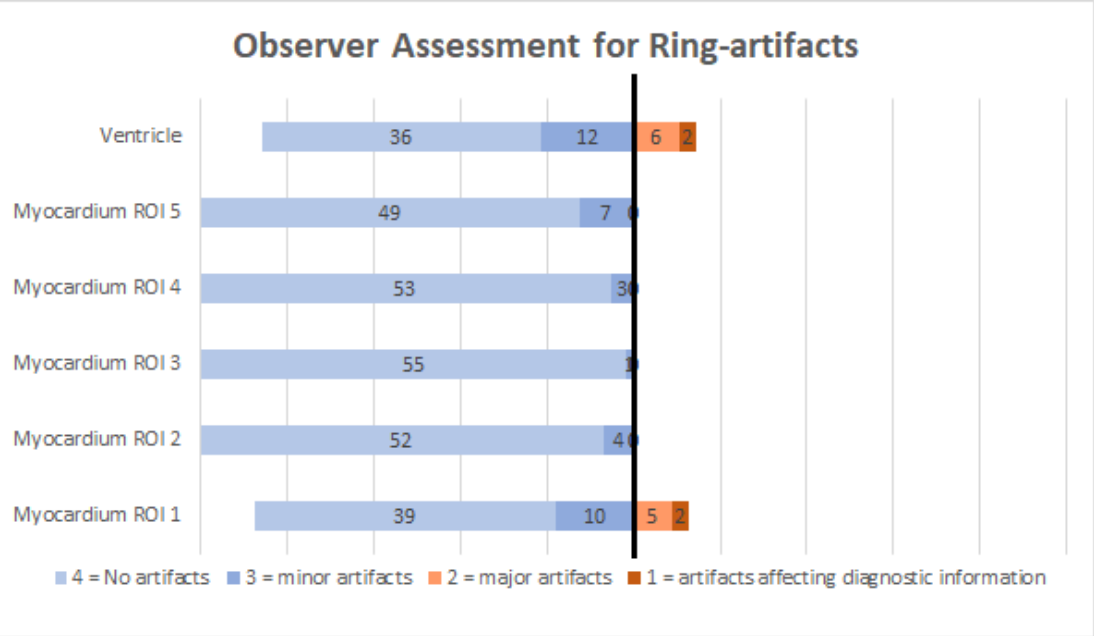

Figure 4.12: Likert scale of the Ring-artifact Observer Assessment for all ROIs. Artifacts were graded using a four-point scale: 1 = artifacts affecting diagnostic information, 2 = major artifacts affecting visualization of major structures but diagnosis still possible, 3 = minor artifacts not interfering with diagnostic decision making, and 4 = No artifacts.

4.5 Signal-to-Noise Ratio

Figure 4.13 shows the boxplot of the SNR in the native and contrast enhanced image. Table 4.8 provides the corresponding results for the SNR of the native image. There is no statistically significant difference between the SNR of the Myocardium ROIs in the native image (p-value=0.7239) on a 1 % significance level. Myocardium ROI 3 has the lowest median (3.098) and the lowest IQR (0.667), but the highest range (9.847) due to the outliers. The smallest range (3.907) can be found in ROI 1. ROI 2 has the highest median (4.070) and ROI 4 the highest IQR (3.139). Outliers can also be found in Myocardium ROI 3 and ROI 5.

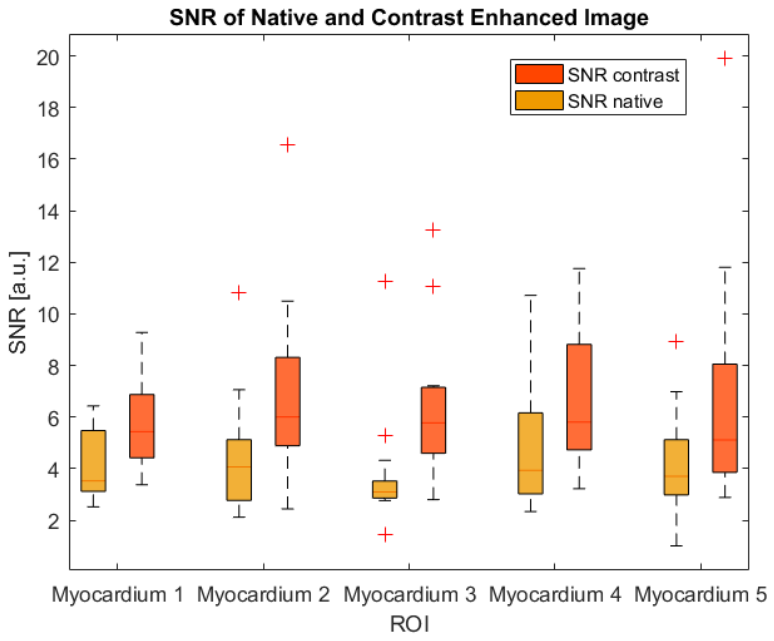

Figure 4.13: Boxplot of the signal-to-noise ratio of the native and contrast enhanced image for each ROI

Table 4.8: Result of the boxplot for signal-to-noise ratio of native images. Min = minimum value, Max = maximum value, Range = maximum value - minimum value, Q_25 = 25th-quartile, Median = median of the values, Q_75 = 75th-quartile, IQR = interquartile-range. All values in [a.u.].

ROI	**Min**	**Max**	**Range**	**Q_25**	**Median**	**Q_75**	**IQR**
Myocardium 1	2.524	6.431	3.907	3.123	3.528	5.482	2.359
Myocardium 2	2.122	10.826	8.704	2.772	4.070	5.126	2.354
Myocardium 3	1.429	11.276	9.847	2.860	3.098	3.527	0.667
Myocardium 4	2.342	10.724	8.381	3.028	3.938	6.167	3.139
Myocardium 5	1.008	8.951	7.943	2.982	3.708	5.129	2.147
Ventricle	1.703	6.192	4.489	2.764	3.293	4.292	1.528

Table 4.9 provides the results of the boxplot shown in figure 4.13 for the SNR

of the contrast enhanced image. There is no statistically significant difference between the SNR of the Myocardium ROIs in the contrast enhanced image (p-value=0.7643) on a 1 % significance level. ROI 5 has the highest range (17.025), the highest IQR (4.199) and the lowest median (5.113). The lowest range (5.899) and the lowest IQR (2.455) can be found in ROI 1. The highest median (6.007) was shown in ROI 2. Outliers can be found in Myocardium ROI 2, ROI 3 and ROI 5.

Table 4.9: Result of the boxplot for signal-to-noise ratio of contrast enhanced images. Min = minimum value, Max = maximum value, Range = maximum value - minimum value, Q_25 = 25th-quartile, Median = median of the values, Q_75 = 75th-quartile, IQR = interquartile-range. All values in [a.u.].

ROI	**Min**	**Max**	**Range**	**Q_25**	**Median**	**Q_75**	**IQR**
Myocardium 1	3.381	9.280	5.899	4.423	5.439	6.878	2.455
Myocardium 2	2.444	16.535	14.092	4.894	6.007	8.317	3.424
Myocardium 3	2.802	13.265	10.463	4.600	5.776	7.155	2.556
Myocardium 4	3.229	11.761	8.532	4.735	5.808	8.823	4.088
Myocardium 5	2.888	19.913	17.025	3.859	5.113	8.058	4.199
Ventricle	9.436	26.398	16.961	12.550	14.497	21.399	8.850

Figure 4.14 shows the boxplot of the SNR in the curvefit for the Myocardium ROIs and the Ventricle ROI and table 4.10 the corresponding results. There is no statistically significant difference between the Myocardium ROIs (p-value=0.6465) on a 1 % significance level. Myocardium ROI 1 and ROI 5 have SNR values in their interquartile range lower than zero. That means, that the power of the noise is higher than the power of the signal. In Myocardium ROI 2 and ROI 4 the lower whiskers reach into the negative range. Myocardium ROI 3 contains one outlier in the negative range. ROI 3 has the highest median (9.964 dB) and the lowest IQR (5.975 dB). The highest IQR (13.907 dB) can be

found in ROI 1. The lowest median (5.320 dB) has ROI 5. ROI 2 has the lowest range (21.804 dB) and ROI 4 has the highest range (29.823 dB).

Table 4.10: Result of the boxplot for signal-to-noise ratio of the curvefit. Min = minimum value, Max = maximum value, Range = maximum value - minimum value, Q_25 = 25th-quartile, Median = median of the values, Q_75 = 75th-quartile, IQR = interquartile-range. All values in [dB].

ROI	**Min**	**Max**	**Range**	**Q_25**	**Median**	**Q_75**	**IQR**
Myocardium 1	-11.474	18.030	29.504	-3.537	8.430	10.369	13.907
Myocardium 2	-5.111	16.693	21.804	1.942	7.444	12.656	10.714
Myocardium 3	-4.736	20.292	25.029	6.566	9.964	12.541	5.975
Myocardium 4	-3.157	26.666	29.823	1.929	9.543	12.463	10.534
Myocardium 5	-11.170	16.520	27.690	-1.088	5.320	9.410	10.498
Ventricle	2.993	41.959	38.966	17.295	21.148	31.642	14.347

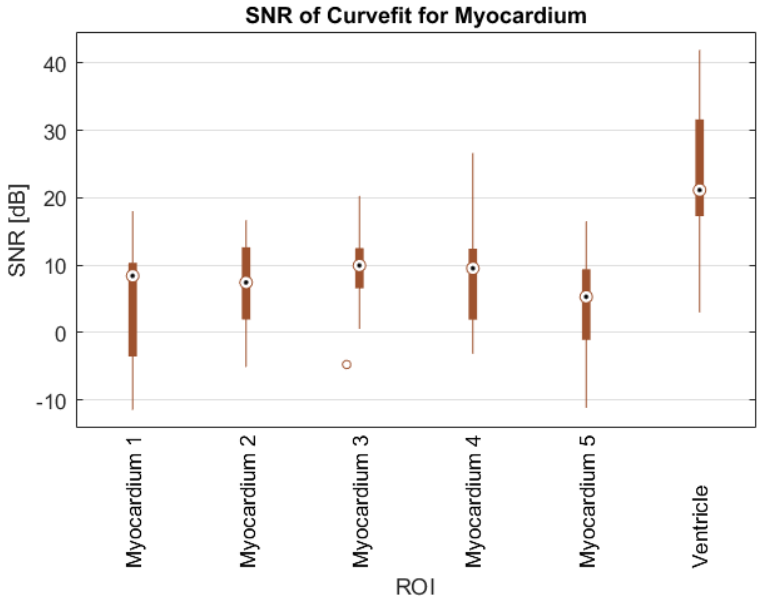

Figure 4.14: Boxplot of SNR in the myocardial curve fit for each ROI

The correlation between the quantitative evaluation of the SNR and the SNR of the curvefit is not significant ($R^2 = 0.104$). It is shown in Figure 4.15.

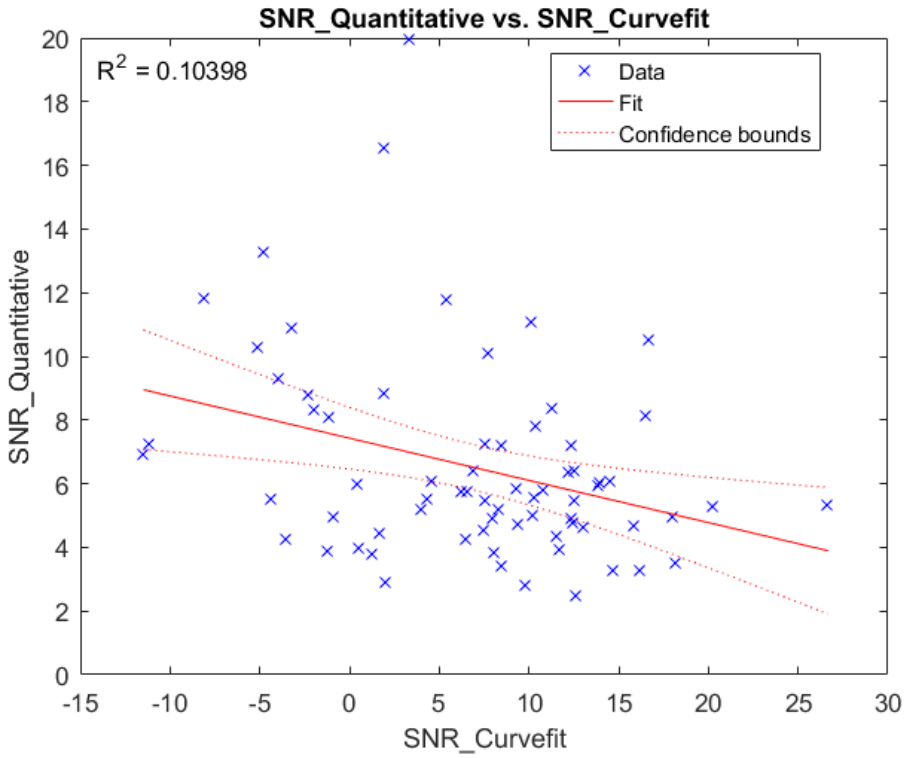

Figure 4.15: Correlation between SNR quantitative and SNR of the curvefit for myocardium ROIs (blue crosses). Regression line (red line), 95 % confidence interval (red dotted lines) and R^2.

4.6 Image Contrast

Figure 4.16 displays the boxplot for the CNR of the Myocardium ROIs. There is no statistically significant difference between the Myocardium ROIs (p-value=0.1122) on a 1 % significance level. ROI 1 has the lowest median (1.060) and the lowest IQR (0.698). ROI 2 has the lowest range (2.259), the highest range is found in ROI 5 at 7.188. The highest median (1.892) shows ROI 4 and the highest IQR (1.610) ROI 3. Outliers are found in Myocardium ROI 1, ROI 4

and ROI 5. Table 4.11 shows the results of the boxplot in figure 4.16.

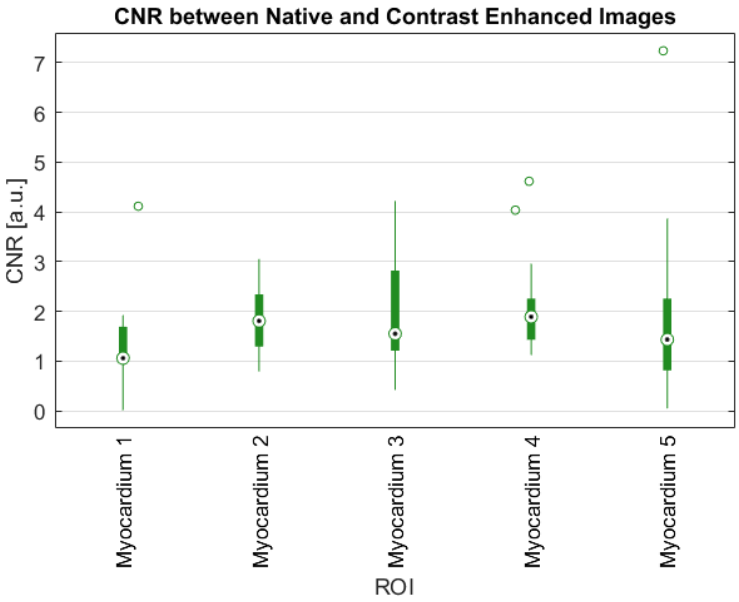

Figure 4.16: Boxplot of CNR in native and contrast enhanced images

Table 4.11: Result of the boxplot for image contrast. Min = minimum value, Max = maximum value, Range = maximum value - minimum value, Q_25 = 25th-quartile, Median = median of the values, Q_75 = 75th-quartile, IQR = interquartile-range. All values in [a.u.].

ROI	**Min**	**Max**	**Range**	**Q_25**	**Median**	**Q_75**	**IQR**
Myocardium 1	0.013	4.115	4.102	0.993	1.060	1.691	0.698
Myocardium 2	0.795	3.053	2.259	1.294	1.809	2.343	1.049
Myocardium 3	0.421	4.222	3.801	1.210	1.550	2.820	1.610
Myocardium 4	1.124	4.616	3.492	1.431	1.892	2.259	0.827
Myocardium 5	0.052	7.240	7.188	0.816	1.435	2.259	1.442
Ventricle	5.500	18.441	12.941	7.331	9.520	13.827	6.496

The boxplot for the CNR of the curvefit for the Myocardium ROIs is shown

in figure 4.17 and table 4.12 provides the corresponding results. There is no statistically significant difference between the Myocardium ROIs (p-value=0.3021) on a 1 % significance level. Myocardium ROI 3 has the highest median at 4.210 followed by Myocardium ROI 4 at 3.776 and ROI 2 at 3.511. Myocardium ROI 5 (3.159) and ROI 1 (3.087) have the lowest median. ROI 4 has the highest range (9.801) and the highest IQR (3.249). ROI 5 has the lowest range (5.704) and the lowest IQR (1.797). Outliers are found in Myocardium ROI 1, ROI 2, ROI 4 and ROI 5.

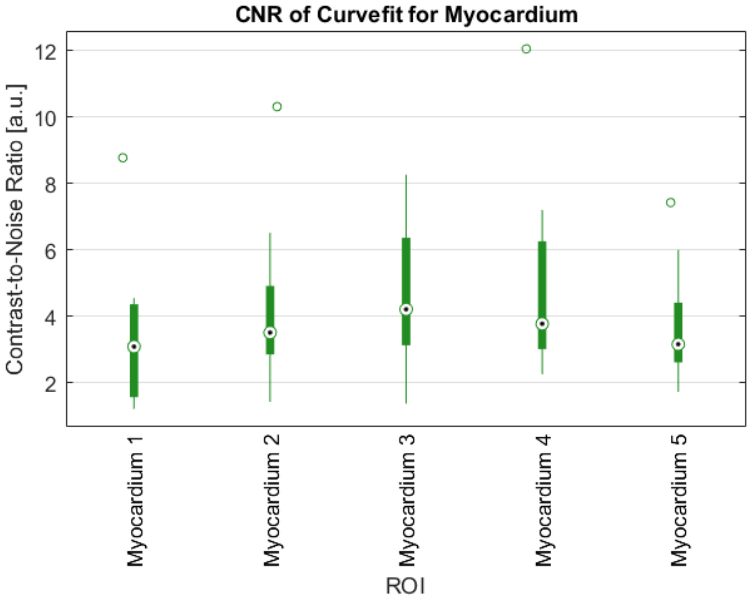

Figure 4.17: Boxplot of CNR in the myocardial curve fit

The correlation between the quantitative evaluation of the CNR and the CNR of the curve fit is not statistically significant ($R^2 = 0.0144$). This is shown in figure 4.18

Table 4.12: Result of the boxplot for the CNR of the curvefit. Min = minimum value, Max = maximum value, Range = maximum value - minimum value, Q_25 = 25th-quartile, Median = median of the values, Q_75 = 75th-quartile, IQR = interquartile-range. All values in [a.u.].

ROI	**Min**	**Max**	**Range**	**Q_25**	**Median**	**Q_75**	**IQR**
Myocardium 1	1.210	8.780	7.570	1.564	3.087	4.364	2.801
Myocardium 2	1.422	10.321	8.899	2.852	3.511	4.918	2.066
Myocardium 3	1.371	8.267	6.897	3.129	4.210	6.366	3.236
Myocardium 4	2.261	12.062	9.801	3.015	3.776	6.263	3.249
Myocardium 5	1.725	7.429	5.704	2.614	3.159	4.411	1.797
Ventricle	6.064	83.814	77.750	16.279	25.421	41.649	25.369

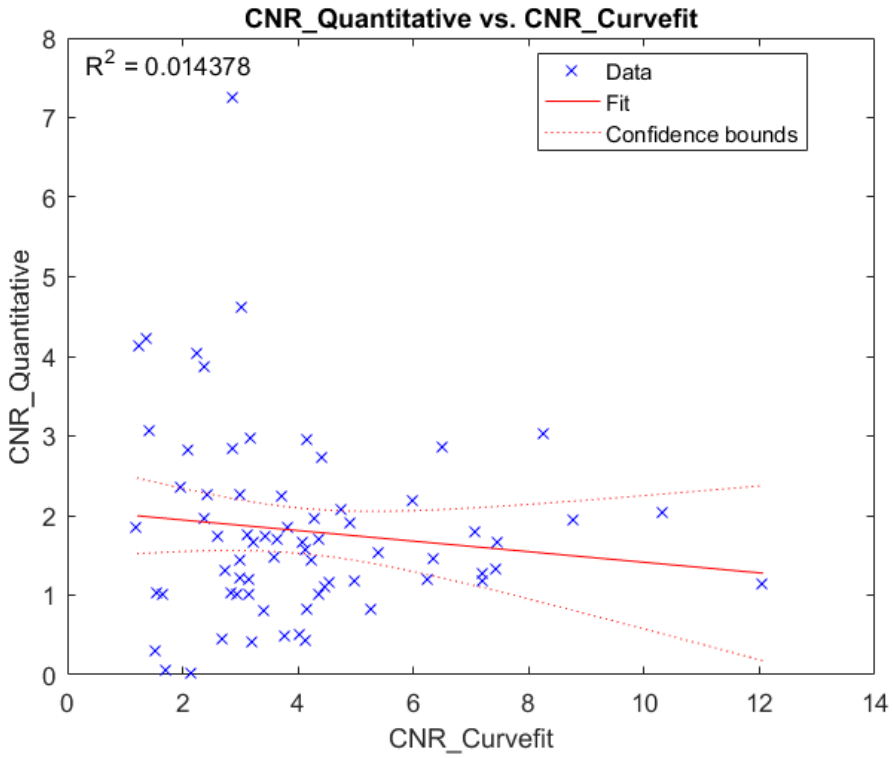

Figure 4.18: Scatterplot of the data (blue crosses), regression line (red line), 95 % confidence interval (red dotted lines) and R^2 for CNR Quantitative vs. CNR of the curve fit for Myocardium

Figure 4.19 shows the histogram of the observer assessment of image contrast for all patients. The results can be listed in a descent order of their incidence as follows:

- 'acceptable image contrast' with n=98 (35 %) observations.
- 'above image contrast' with n=55 (19.64 %) observations.
- 'excellent image contrast' with n=52 (18.57 %) observation.
- 'suboptimal image contrast' with n=48 (17.14 %) observation.
- 'very poor image contrast' with n=27(9.64 %) observations

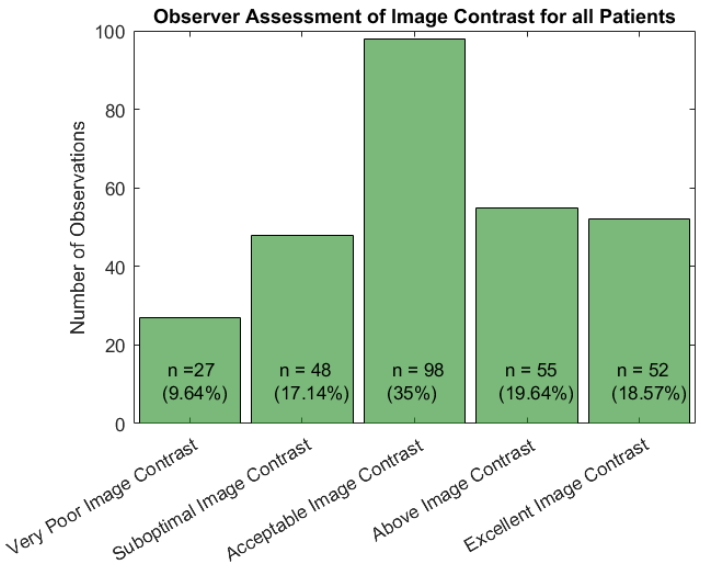

Figure 4.19: Histogram of contrast assessment for all Patients

Figure 4.20 shows that Myocardium ROI 4 was assessed to be the ROI with the best image contrast. Next, Myocardium ROI 5 shows a similar result like ROI 4. The last three ROIs can be ranked: Myocardium ROI 3, ROI 2 and ROI 1, whereas the differences are minimal.

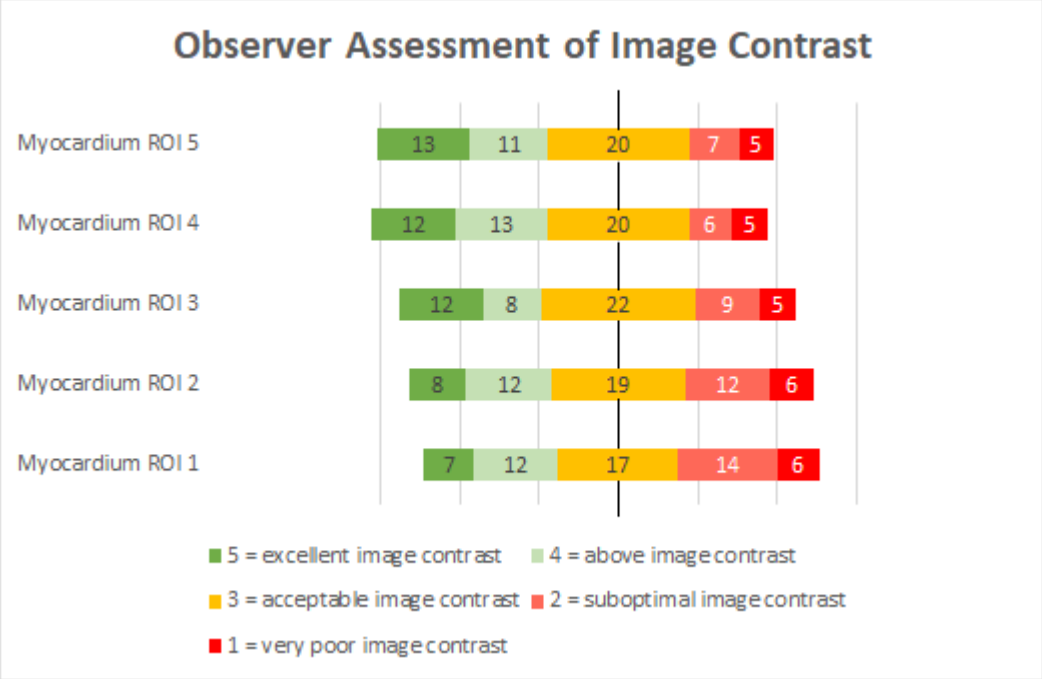

Figure 4.20: Likert Scale for Contrast Observer Assessment for all ROIs. Image Contrast was graded using a five-point scale: 5 = excellent image contrast, 4 = above image contrast, 3 = acceptable image contrast, 2 = suboptimal image contrast, and 1 = very poor image contrast.

4.7 Curve Fitting Assessment

For the myocardial perfusion quantification a model function has to be found that fits the raw data of the myocardium and the ventricle. One assumption for the perfusion quantification is that the model function for the myocardium and the ventricle have the same baseline.

4.7.1 Ventricle Baseline vs. Myocardial Baseline

Figure 4.21 shows a boxplot of the difference between ventricle baseline and myocardium baseline for each myocardium ROI. The corresponding results are

summarized in table 4.13. There is no statistically significant difference between the Myocardium ROIs (p-value=0.1168) on a 1 % significance level. The lowest median was found in Myocardium ROI 1 at 0.30 HU as well as the lowest range (31.32 HU) and the lowest IQR (8.00 HU), but there are outliers. The highest median shows ROI 4 at 7.58 HU. ROI 3 has the highest range (35.66 HU) and the highest IQR (16.94 HU). Outliers were found in ROI 2.

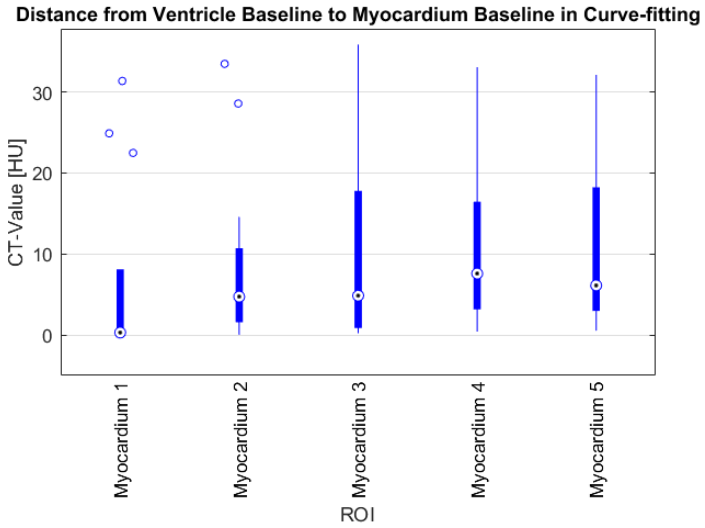

Figure 4.21: Boxplot of the difference between Ventricle baseline and Myocardium baseline for each ROI

Table 4.13: Result of the boxplot for the baseline difference between myocardium and ventricle. Min = minimum value, Max = maximum value, Range = maximum value - minimum value, Q_25 = 25th-quartile, Median = median of the values, Q_75 = 75th-quartile, IQR = interquartile-range. All values in [HU].

ROI	**Min**	**Max**	**Range**	**Q_25**	**Median**	**Q_75**	**IQR**
Myocardium 1	0.05	31.37	31.32	0.11	0.30	8.11	8.00
Myocardium 2	0.02	33.48	33.46	1.57	4.73	10.70	9.14
Myocardium 3	0.21	35.87	35.66	0.85	4.85	17.79	16.94
Myocardium 4	0.41	33.07	32.66	3.15	7.58	16.45	13.30
Myocardium 5	0.53	32.12	31.58	2.97	6.12	18.23	15.26

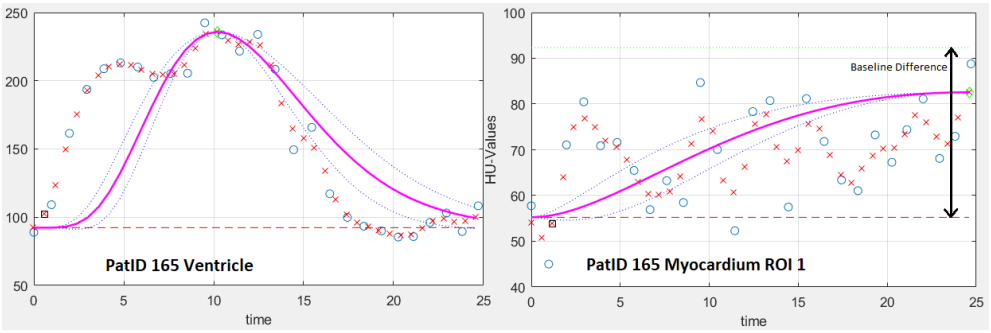

Figure 4.22: Difference between Ventricle baseline and Myocardium baseline for PatID 165 ROI 1. Blue circles indicate the raw data, red crosses are the interpolated data, magenta line shows the model curve fit, red dashed line in the right plot shows the myocardial baseline, red dashed line in the left plot the ventricle baseline. Green dotted line in the right plot shows the ventricle baseline. The blue dotted lines shows the 95 % confidence interval.

4.7.2 Minimum Raw Data vs. Minimum Model Data

The minimum CT-values of the raw data are used for the computation of the baseline. The minimum CT-values of the model data correspond to the baseline data. Therefore, the difference between the minimum of the raw data and the minimum of the model data should be as small as possible to get meaningful perfusion results. The distance between the minimum CT-values of the raw data and the model data are shown in figure 4.23 and table 4.14. Myocardium ROI 2 has the greatest range at 35.14 HU and the lowest IQR at 4.34 HU. The lowest median was found in ROI 4 (5.46 HU) and the highest median in ROI 1 (9.40 HU). The lowest range shows ROI 3 at 17.00 HU and the highest IQR (13.12 HU) in ROI 5. There is no statistically significant difference between the Myocardium ROIs (p-value=0.581) on a 1 % significance level.

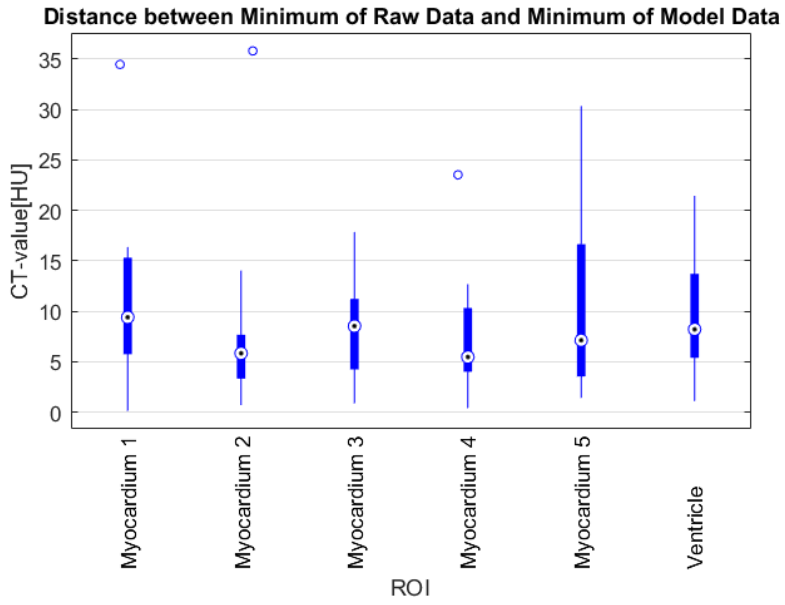

Figure 4.23: Boxplot of the difference between the Minimum CT-value in the raw data and the model data for each ROI

Table 4.14: Result of the boxplot for difference between the minimum of raw data and the minimum of model data. Min = minimum value, Max = maximum value, Range = maximum value - minimum value, Q_25 = 25th-quartile, Median = median of the values, Q_75 = 75th-quartile, IQR = interquartile-range. All values in [HU].

ROI	**Min**	**Max**	**Range**	**Q_25**	**Median**	**Q_75**	**IQR**
Myocardium 1	0.11	34.48	34.37	5.74	9.40	15.31	9.57
Myocardium 2	0.68	35.82	35.14	3.32	5.83	7.66	4.34
Myocardium 3	0.86	17.86	17.00	4.22	8.53	11.22	7.00
Myocardium 4	0.39	23.53	23.14	4.01	5.46	10.33	6.32
Myocardium 5	1.41	30.36	28.95	3.53	7.12	16.65	13.12
Ventricle	1.09	21.45	20.36	5.38	8.21	13.71	8.34

4.7.3 Maximum Raw Data vs. Maximum Model Data

The boxplot in figure 4.24 and table 4.15 shows the results for the difference of the maximum in the raw data and model data. The ventricle shows the lowest median at 3.34 HU and the lowest IQR (2.93 HU). But there are outliers in the ventricle, therefore the range is 18.49 HU. The comparison of the myocardium ROIs show, that ROI 1 hast the lowest median at 7.16 HU. ROI 4 has the lowest range (12.03 HU), the lowest IQR (5.91 HU) and the highest median (11.21 HU). The highest range can be found in ROI 5 (34.16 HU) and the highest IQR in ROI 3 (10.28 HU). There is no statistically significant difference between the Myocardium ROIs (p-value=0.711) on a 1 % significance level.

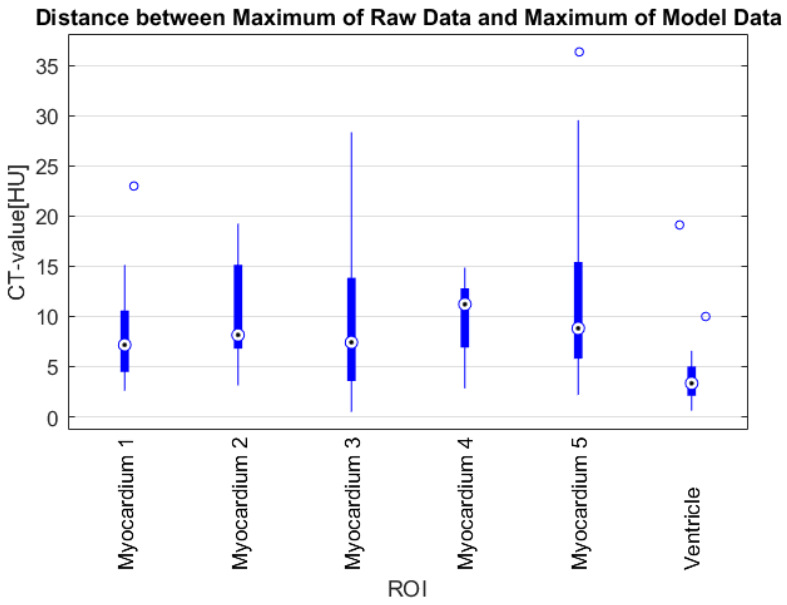

Figure 4.24: Boxplot of the difference between the maximum CT-value in the raw data and the model data for each ROI

Table 4.15: Result of the boxplot for the difference between the maximum of the raw data and the maximum of the model data. Min = minimum value, Max = maximum value, Range = maximum value - minimum value, Q_25 = 25th-quartile, Median = median of the values, Q_75 = 75th-quartile, IQR = interquartile-range. All values in [HU].

ROI	**Min**	**Max**	**Range**	**Q_25**	**Median**	**Q_75**	**IQR**
Myocardium 1	2.59	22.98	20.39	4.46	7.16	10.58	6.12
Myocardium 2	3.12	19.24	16.12	6.78	8.14	15.13	8.35
Myocardium 3	0.48	28.34	27.85	3.56	7.41	13.85	10.28
Myocardium 4	2.83	14.86	12.03	6.89	11.21	12.80	5.91
Myocardium 5	2.18	36.34	34.16	5.80	8.81	15.42	9.63
Ventricle	0.61	19.10	18.49	2.09	3.34	5.01	2.93

4.7.4 Signal Range Raw Data vs. Signal Range Model Data

Figure 4.25 shows the boxplot of the difference between the signal range of the raw data and the model data. A small difference between those ranges could be a criterion for perfusion results because they would show a good correspondence. As shown in table 4.16, the ventricle has a median at 10.49 HU, a range at 27.15 HU and an IQR at 10.09 HU. When comparing the myocardium, ROI 3 has the lowest median at 11.95HU. ROI 4 has the lowest range (32.07 HU) and the lowest IQR (7.58 HU). ROI 5 shows the highest range (60.39 HU) and the highest median (17.52 HU). The highest IQR was found in ROI 1 at 17.78 HU. Outliers are in ROI 2, ROI 3, ROI 4, ROI 5 and in the ventricle ROI. There is no statistically significant difference between the Myocardium ROIs (p-value=0.659) on a 1 % significance level.

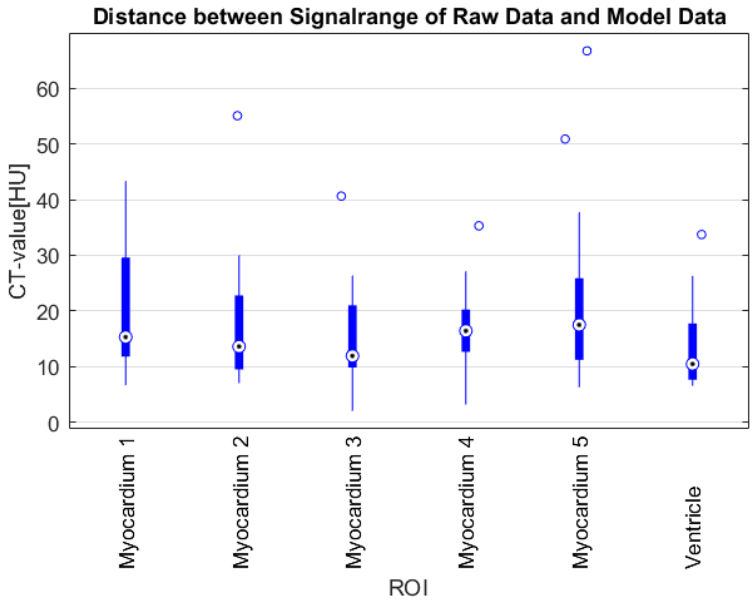

Figure 4.25: Boxplot of the Difference of the Signal range in the raw data and the model data for each ROI

Table 4.16: Result of the boxplot for the difference between signal range of the raw data and the model data. Min = minimum value, Max = maximum value, Range = maximum value - minimum value, Q_25 = 25th-quartile, Median = median of the values, Q_75 = 75th-quartile, IQR = interquartile-range. All values in [HU].

ROI	**Min**	**Max**	**Range**	**Q_25**	**Median**	**Q_75**	**IQR**
Myocardium 1	6.68	43.33	36.65	11.82	15.33	29.60	17.78
Myocardium 2	7.05	55.06	48.01	9.52	13.62	22.80	13.28
Myocardium 3	2.07	40.63	38.56	9.85	11.95	21.03	11.18
Myocardium 4	3.22	35.29	32.07	12.68	16.45	20.26	7.58
Myocardium 5	6.32	66.70	60.39	11.25	17.52	25.90	14.65
Ventricle	6.59	33.73	27.15	7.66	10.49	17.76	10.09

4.7.5 Mean Square Error

Figure 4.26 displays the boxplot of the MSE of the curvefit for all myocardium ROIs and for the ventricle ROI. The result of the boxplot are shown in table 4.17. The ventricle ROI has a range of 0.127, a median of 0.040 and an IQR of 0.050. Myocardium ROI 1 has the highest range (3.648) due to the highest outlier. ROI 4 has the lowest range (0.181), the lowest median (0.013) and the lowest IQR (0.012). ROI 3 has the highest median at 0.020 and the highest IQR at 0.025. There is no statistically significant difference between the myocardium ROIs (p-value=0.934) on a 1 % significance level.

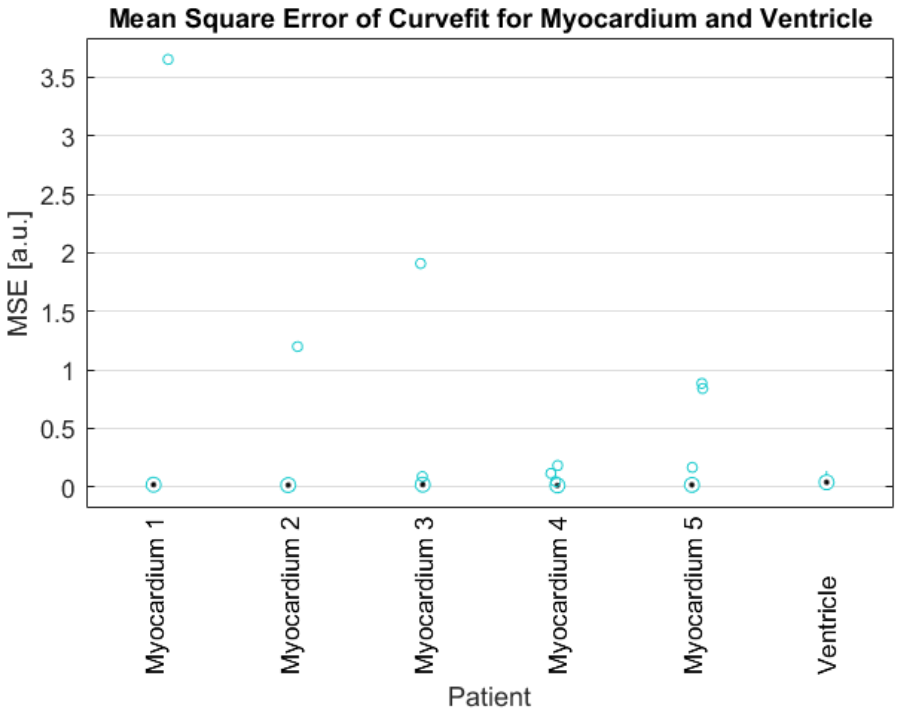

Figure 4.26: Boxplot of MSE in the myocardial curvefit for each ROI

Table 4.17: Result of the boxplot for MSE in the myocardial and ventricle curvefit. Min = minimum value, Max = maximum value, Range = maximum value - minimum value, Q_25 = 25th-quartile, Median = median of the values, Q_75 = 75th-quartile, IQR = interquartile-range. All values in [dB].

ROI	**Min**	**Max**	**Range**	**Q_25**	**Median**	**Q_75**	**IQR**
Myocardium 1	0.005	3.653	3.648	0.011	0.019	0.032	0.021
Myocardium 2	0.004	1.199	1.195	0.012	0.016	0.027	0.015
Myocardium 3	0.005	1.909	1.904	0.010	0.020	0.035	0.025
Myocardium 4	0.002	0.183	0.181	0.010	0.013	0.022	0.012
Myocardium 5	0.006	0.885	0.879	0.014	0.018	0.033	0.019
Ventricle	0.010	0.137	0.127	0.026	0.040	0.075	0.050

Figure 4.27 shows the scatterplot for the correlation between MSE and SNR of the curvefit. SNR of the curvefit higher than zero leads to a MSE that is nearly zero. The correlation between MSE and SNR of the curvefit was R^2=0.13831 and therefore not statistically significant.

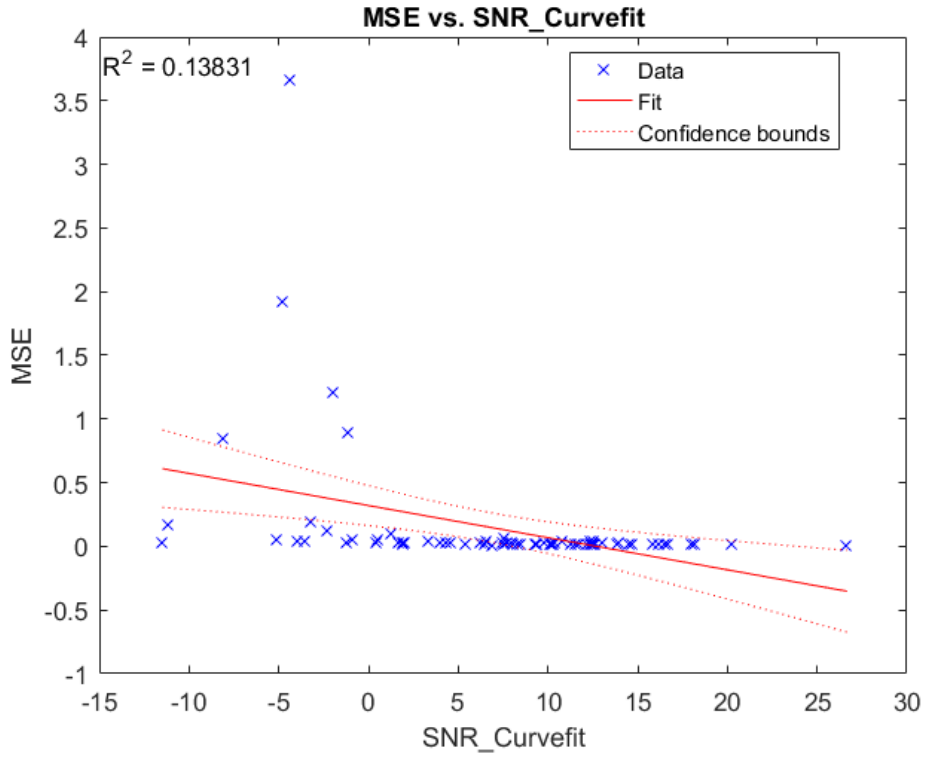

Figure 4.27: Scatterplot of the data (blue crosses), regression line (red line), 95 % confidence interval (red dotted lines) and R^2 for MSE vs. SNR of the curvefit for myocardium

5 Discussion

The aim of this thesis was to determine and compare image quality parameter of axial reconstructed CT scans for quantitative myocardial perfusion calculation in 5 different ROIs of the myocardium.

5.1 Perfusion Calculation

The results for the MBF using the upslope and fermi method are comparable to the results in the literature, which have a range of 46.37 - 138.490 ml/100g/min for the global MBF at rest and a range of 76.37 - 208.43 ml/100g/min for the global MBF at stress [55]. The standard-deviation for the upslope method in Myocardium ROI 3 (SD =111.53 ml/100g/min) is at highest. The outlier in Myocardium ROI 3, when using the upslope method, occurred in PatientID 51. The reason for this outlier were streak-artifacts which were caused by the aortic valve and the vertebral body. Myocardium ROI 5 shows a high standard-deviation in the upslope method (SD= 63.10 ml/100g/min). These outlier can also be found using the fermi method for MBF calculation. Using the fermi method, the outlier in ROI 5 has more impact on the MBF results. This outlier in ROI 5 occurred in PatientID 165 where the baseline difference was 29.31 HU. The reason for this baseline difference was that the scan started too late. Additionally, ROI 2 and ROI 3 show outliers when using the fermi method, but no outlier can be found in ROI 2 when using the upslope method. The outliers in ROI 2 and ROI 3 occurred in PatientID 1024, where the baseline differences were 28.58 HU and 33.89 HU, respectively. Again, the scan was started too late. Therefore, it seems that baseline differences have more impact on the perfusion results when using the fermi method.

5.2 Image Signal Intensity

In Myocardium ROI 1 outliers can be found in both the native and the contrast enhanced image. These outliers occurred in PatientID 67 where a ring-artifact was found. Further outliers are in the native image in ROI 3 and ROI 5. They occurred in PatientID 51 and PatientID 78, respectively. The range of the signal intensities are highest for the contrast enhanced images in ROI 3 and ROI 5.

5.3 Image Noise

The ranges for image noise in the quantitative evaluation are very similar for all ROIs. In the observer assessment there are also very similar results for each ROI. The quantitative evaluation for image noise by determining the standard-deviation is not difficult. On the other hand, the observer assessment of image noise is not that easy, since it is hard to define. Some may interpret noise only as appearance of artifacts, others may interpret it as the graininess in the image. Summed up, the images are very noisy because only 28 % of the ROIs were assessed better than average noise and 35 % were assessed worse than average image noise. It also depends on the choice of the window.

5.4 Artifacts

Artifacts were only assessed by radiologists. There was no quantitative evaluation for artifacts per se, but the idea was that it would be comparable to the quantitative image noise assessment.

5.4.1 Streak-artifacts

The observer assessed that streak-artifacts have the most impact on ROI 3 and the least on ROI 5. When comparing those two ROIs, ROI 3 is additionally influenced by contrast medium in the aorta, contrast medium in the right heart and the rib. On the other hand, ROI 5 is additionally influenced by LAD and LCX.

The most frequent origin is the vertebral body followed by the aortic valve and 'none of the aforementioned' origin. The reason for the frequent observation of the aortic valve may be that patiens with aortic valve stenosis were selected for this work. Calcifications in the aortic valve can lead to this stenosis and therefore, artifacts like beam-hardening can occur.

The category 'none of the aforementioned' includes origins that were either not by default selectable or written by hand on the questionnaire. E.g., one radiologist writes that the contrast medium in the left ventricular cavity causes streak-artifacts. Another radiologist writes that detector defects cause streak-artifacts.

5.4.2 Motion-artifacts

The results for the motion-artifact assessment showed that 16.96 % of the ROIs were affected by motion-artefacts. Although the breath-hold time can last until 30 s, motion-artifacts due to respiration were rare. Besides, motion-artifacts may lead to shift the ROIs out of the myocardium and therefore have an impact on image quality degradation. On the other hand, motion-artifacts can also occur when the heart beats too fast. This can lead to i.e. blurring of the border between the heart and the lung.

5.4.3 Ring-artifacts

Ring-artifacts affect diagnostic information or show major artifacts in the ventricle and ROI 1. Minor artifacts can be assessed in descending order as follows: ROI 5, ROI 2, ROI 4 and ROI 3. That is because ring-artifacts occur if a detector fails to function or is out of calibration [34], as described in section 2.4.4. These artifacts occur in the center of the FOV and therefore in the adjacent ROIs. These ring-artifacts appeared in the scans acquired in Moscow in PatientID 25 and PatientID 45, which were scanned on 26/02/2015 and 21/02/2015, respectively. Also in PatientID 66 and PatientID 67, which were scanned on the same day (11/06/2015). Scans acquired in Tashkent show ring-artifacs too. PatientID 1018 was scanned on 16/12/2016 and PatientID 1037 one year later on 26/12/2017. In between, the scanner may have been calibrated.

5.5 Signal-to-Noise Ratio

The lowest SNRs of the native images can be found in ROI 3 and ROI 5, but in the contrast enhanced images these differences are negligible. Therefore, the outliers in the results for the MBF can not be explained by the result of the SNR. On the other hand, the results for the SNR of the curvefit show negative values for nearly every myocardial ROI. Only ROI 3 has just an outlier in the negative. The scatterplot for the quantitative SNR and the SNR of the curvefit show no statistical significant correlation. This difference may occur due to the different calculation methods. The quantitative estimation of the SNR in native and contrast enhanced images represents only two fixed moments. The calculation of the SNR of the curvefit includes the volatility over time.

5.6 Image Contrast

The term 'image contrast' in this work can be misinterpreted. Not only the difference of the density in the myocardium and the adjacent ventricle in one slice was meant, but the contrast enhancement of the myocardium during the first pass of the contrast medium. Myocardium ROI 3 shows highest CNR in both the quantitative evaluation and the curvefit. On the other hand, observer assessed that ROI 4 and ROI 5 show the best contrast.

5.7 Curve Fitting

The distance between the baselines in the ventricle and the myocardium show that the medians of the ROIs are in a range from 0.30-7.58 HU. Therefore, the baselines for the ventricle and the myocardium had a good agreement for one half of the patients. But the other half of the patients show distances up to more than 30 HU. A significant result for MBF calculation in distances up to more than 30 HU is disputable.

The distance between the minimum of the raw and the model data shows medians in a range from 5.46-9.40 HU. The extreme outliers in Myocardium ROI 1, ROI 2 and ROI 4 occur in PatientID 51. The highest value in ROI 5 belongs to PatientID 78.

The distance between the maximum of raw and model data has medians in a range from 7.16-11.21 HU. The outlier in Myocardium ROI 1 occurs in PatientID 1023, and the outlier in ROI 5 occurs in PatientID 78.

The distance between the signal range of raw and model data has medians in a range from 11.95-17.52 HU. Therefore, finding the suitable minimum for the model data seems to work better than finding the suitable maximum. This discrepancy in finding the suitable minimum and maximum is reflected in the results for the distance of the signal range. These results are comparable to the range

of image noise.

The extreme outlier of the mean square error in ROI 1, ROI 2 and ROI 3 occur in the same patient, namely PatientID 51. These ROI's were affected by motion-artifacts and streak-artifacts. The causes for these streak-artifacts were: The aortic valve, the vertebral body and contrast medium in the right heart. The mild outlier in ROI 4 occur in PatientID 78. The outlier in ROI 5 came from PatientID 51 and PatientID 78, and one mild outlier came from PatientID 165. Therefore, only three patients are reliable for these outlier. ROI 4 and ROI 5 in PatientID 78 were affected by motion-artifacts. Occasionally, these ROIs slipped into the ventricle. This led to a noisy data set in these ROIs and further to a high mean square error. ROI 5 in PatientID 165 was also affected by motion-artifacts but did not slip into the ventricle. Additionally, a ring-artifact occurred in this ROI.

6 Conclusion

The quantitative evaluation of myocardial perfusion using computed tomography is a promising modality. However, the results of the perfusion calculation depend on the image quality of the CT scans. In particular, image noise due to streak-artifacts degrades the image quality at most. The streak-artifacts were mainly caused by the vertebral body. Furthermore, the calcifications of the aortic valve and the mitral valve led to streak-artifacts. Besides, the image quality of the myocardium depends on the location. The apical region of the myocardium is most affected by streak-artifacts followed by the interseptal region whereas the lateral region is the least affected.

Motion-artifacts that influenced the diagnostic information occurred only in one patient and concerned the entire myocardium. Therefore, it could be shown that motion-artifacts are rare, but if they occur, they have a great impact on the perfusion results.

Ring-artifacts were also rare but had hardly an effect on image quality. They occurred only in the ventricle and the basoseptal region of the myocardium. The reason for this location is the consistently erroneous reading at each view of the detector system in which the central detectors were involved. This artifact can easily be fixed by recalibration or repair service. The subjective image contrast also depends on the localization, because the lateral region of the myocardium was rated better in terms of image contrast than the septal region. The reason for this is probably that the contrast of the lateral region, which is surrounded by the lungs, is subjectively felt more strongly than the contrast between the myocardium and the right ventricle.

The perfusion of the myocardium was calculated using two different methods, the

Upslope and the Fermi method. The Upslope method requires model curves that fit the raw data. Therefore, the result of the perfusion calculation depends on how accurate the raw data is fitted by the model curve. To determine this accuracy the mean square error was calculated, where the smaller the mean square error the better the accuracy. The reasons for high mean square errors were high image noise due to motion-artifacts in one patient and streak-artifacts in two patients, which led to overestimated results in the perfusion evaluation. Nevertheless, there were patients with low mean square errors and overestimated perfusion results. The reason for that was the difference between the myocardial and ventricular baseline. The baselines were not recognized correctly either because the data had high noise or because the timing between the contrast agent application and scanstart was not chosen correctly.

In order to improve the quality of the perfusion evaluation special attention should be paid to the avoidance of scanner-based artifacts that could be avoided by calibrating the scanner. Since the vertebral body apparently has the greatest influence on the emergence of streak artefacts, correction algorithms could be developed which counteract this influence. Another step to improve the perfusion results is to optimize the timing between contrast agent and scanstart. By improving the image quality, the evaluation of the left ventricular myocardial perfusion using computed tomography could be given a higher priority.

A Appendix

A.1 Questionnaire

Questionnaire: Assessment of Image Quality

1. Introduction

My name is Michaela Hawranek and I am writing my masterthesis with the topic „Quantitative Evaluation of Left Ventricular Myocardial Perfusion Using Computed Tomography – Assessment of Image Quality".

This questionnaire is divided into 3 parts, *Assessment of Image Contrast*, *Assessment of Image Noise* and *Assessment of Artifacts*, respectively.

The Assessment of Artifacts is subdivided into *Streakartifacts*, *Ringartifacts* and *Motionartifacts.*

To assess the Image Quality the following questions for 14 patients are provided. To answer the questions please circle your choice.

Thank you very much!

The picture on the right side shows an example of ROI-Arrangement in the Myocardium:

ROI 1…septobasal

ROI 2… septoapical

ROI 3…apical

ROI 4…lateroapical

ROI 5…laterobasal

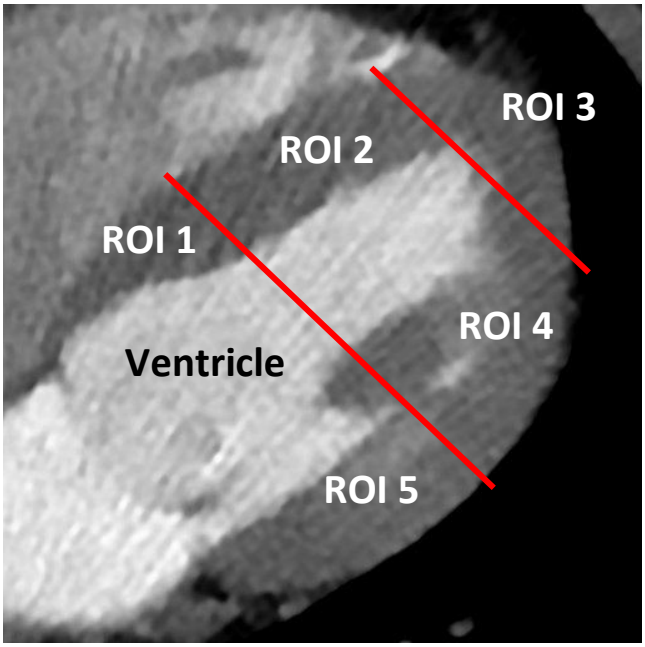

2. Beginn of Questionnaire:

Years of CT Experience

5-8	9-12	13-17	18-25	> 25

Patient Nr. 25

1. Assessment of Image Contrast

Please assess the Image Contrast between the Myocardium ROI 1-5 in the native Image and Image with maximal Contrast.

Image contrast is ranked and assessed by using a five-point scale (5 = excellent image contrast, 4 = above average contrast, 3 = acceptable image contrast, 2 = suboptimal image contrast, and 1 = very poor contrast).

	Excellent Image Contrast	Above Image Contrast	Acceptable Image Contrast	Suboptimal Image Contrast	Very Poor Image Contrast
ROI 1	5	4	3	2	1
ROI 2	5	4	3	2	1
ROI 3	5	4	3	2	1
ROI 4	5	4	3	2	1
ROI 5	5	4	3	2	1

2. Assessment of Image Noise

Please assess the Image Noise for the Ventricle ROI and for Myocardium ROI 1-5.

Subjective image noise is assessed by using a five-point scale (5 = minimal image noise, 4 = less than average noise, 3 = average image noise, 2 = above average noise, and 1 = unacceptable image noise).

	Minimal Image Noise	*Less than Average Image Noise*	*Average Image Noise*	*Above Average Noise*	*Unacceptable Image Noise*
ROI Ventricle	5	4	3	2	1
ROI 1	5	4	3	2	1
ROI 2	5	4	3	2	1
ROI 3	5	4	3	2	1
ROI 4	5	4	3	2	1
ROI 5	5	4	3	2	1

3. Assessment of Artifacts

3.1 Streak-artifacts

Please assess the Streak-artifact for the Ventricle ROI and for Myocardium ROI 1-5.

Artifacts are graded using a four-point scale: 1 = artifacts affecting diagnostic information, 2 = major artifacts affecting visualization of major structures but diagnosis still possible, 3 = minor artifacts not interfering with diagnostic decision making, and 4 = No artifacts

Streak-artifact	*Artifacts affecting diagnostic information*	*Major artifacts*	*Minor artifacts*	*No artifacts*
ROI Ventricle	1	2	3	4
ROI 1	1	2	3	4
ROI 2	1	2	3	4
ROI 3	1	2	3	4
ROI 4	1	2	3	4
ROI 5	1	2	3	4

If there are any Streak-Artifacts, what are their origin? Please mark with a cross the origin of Streak-artifacts and the corresponding ROI in the lists below.

Calcification/Implants in:	*RCA*	*LAD*	*LCX*	*Aortic Valve*	*Mitral Valve*
Appear in which ROI:					
ROI Ventricle	☐	☐	☐	☐	☐
ROI 1	☐	☐	☐	☐	☐
ROI 2	☐	☐	☐	☐	☐
ROI 3	☐	☐	☐	☐	☐
ROI 4	☐	☐	☐	☐	☐
ROI 5	☐	☐	☐	☐	☐

	Rip	*Vertebral Body*	*Contrast Medium in Aorta*	*Contrast Medium in Right Heart*	*Pacemaker Leads*	*ECG Leads*	*None of the afore-mentioned*
Appear in which ROI:							
ROI Ventricle	☐	☐	☐	☐	☐	☐	☐
ROI 1	☐	☐	☐	☐	☐	☐	☐
ROI 2	☐	☐	☐	☐	☐	☐	☐
ROI 3	☐	☐	☐	☐	☐	☐	☐
ROI 4	☐	☐	☐	☐	☐	☐	☐
ROI 5	☐	☐	☐	☐	☐	☐	☐

3.2 Ring-Artifact

Please assess the **Ring-artifact** for the Ventricle ROI and for Myocardium ROI 1-5.

Artifacts are graded using a four-point scale: 1 = artifacts affecting diagnostic information, 2 = major artifacts affecting visualization of major structures but diagnosis still possible, 3 = minor artifacts not interfering with diagnostic decision making, and 4 = No artifacts

Ringartifact	*Artifacts affecting diagnostic information*	*Major artifacts*	*Minor artifacts*	*No artifacts*
ROI Ventricle	1	2	3	4
ROI 1	1	2	3	4
ROI 2	1	2	3	4
ROI 3	1	2	3	4
ROI 4	1	2	3	4
ROI 5	1	2	3	4

3.3 Motion-Artifact

Please assess the **Motion-artifact** for the Ventricle ROI and for Myocardium ROI 1-5.

Artifacts are graded using a four-point scale: 1 = artifacts affecting diagnostic information, 2 = major artifacts affecting visualization of major structures but diagnosis still possible, 3 = minor artifacts not interfering with diagnostic decision making, and 4 = No artifacts

Motion Artifact	*Artifacts affecting diagnostic information*	*Major artifacts*	*Minor artifacts*	*No artifacts*
ROI Ventricle	1	2	3	4
ROI 1	1	2	3	4
ROI 2	1	2	3	4
ROI 3	1	2	3	4
ROI 4	1	2	3	4
ROI 5	1	2	3	4

End of Patient 25

B Plots

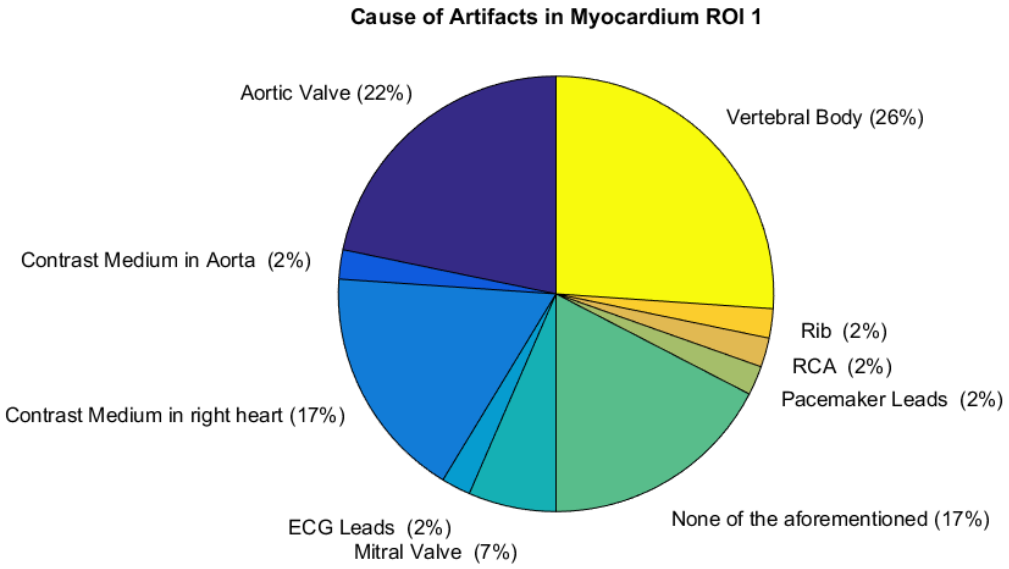

Figure B.1: Pieplot for the causes of Streak-artifacts in ROI 1

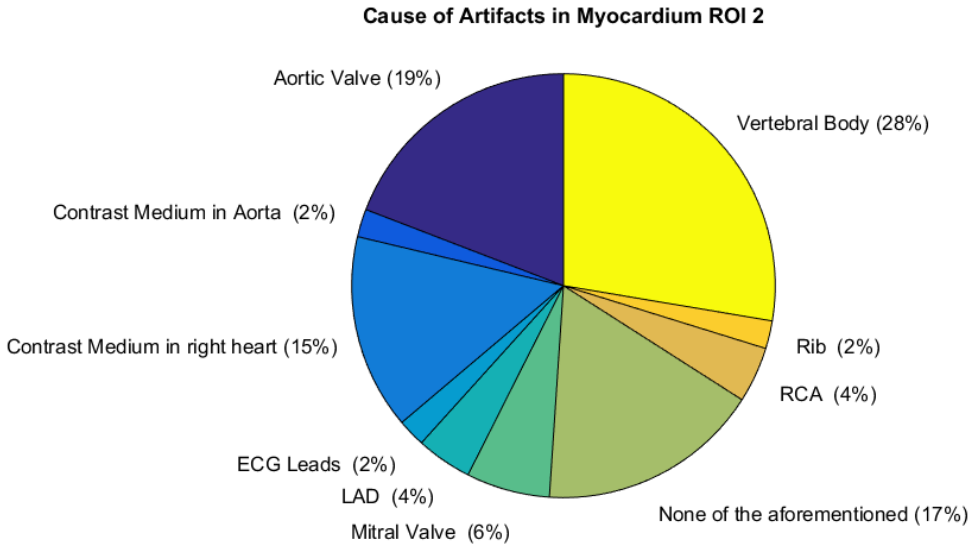

Figure B.2: Pieplot for the causes of Streak-artifacts in ROI 2

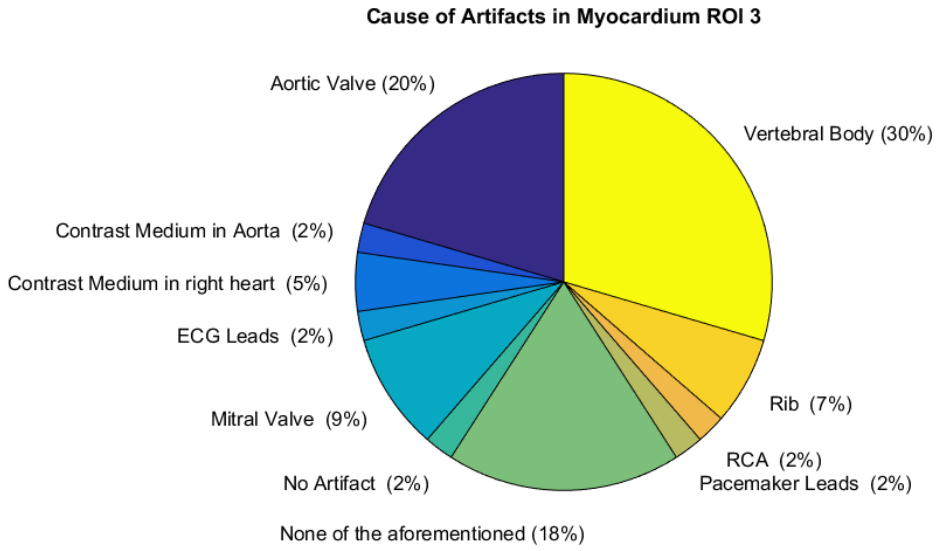

Figure B.3: Pieplot for the causes of Streak-artifacts in ROI 3

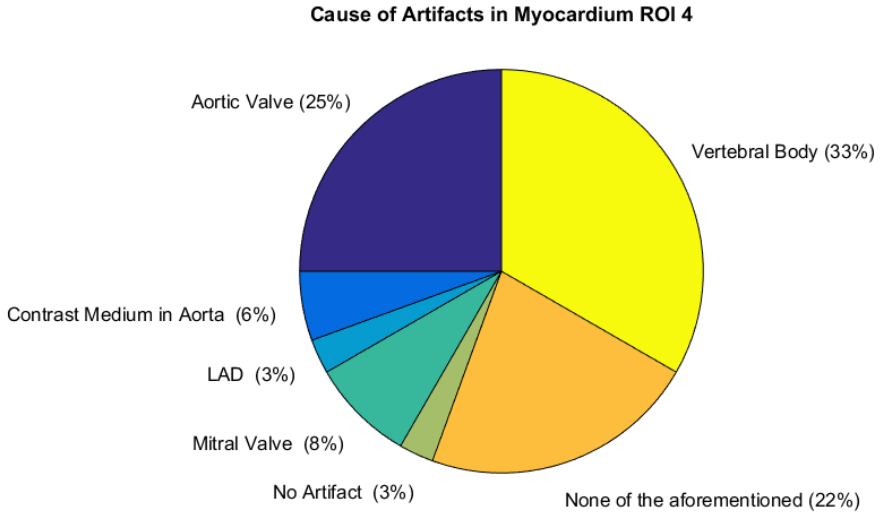

Figure B.4: Pieplot for the causes of Streak-artifacts in ROI 4

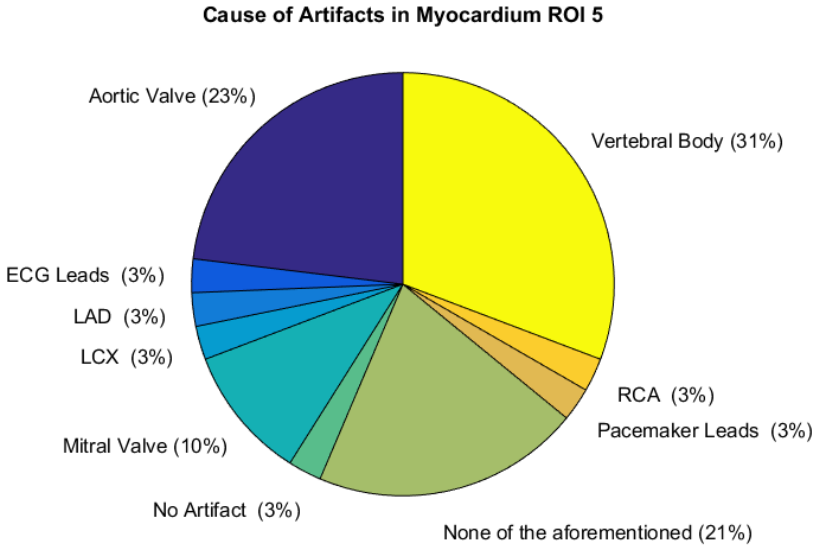

Figure B.5: Pieplot for the causes of Streak-artifacts in ROI 5

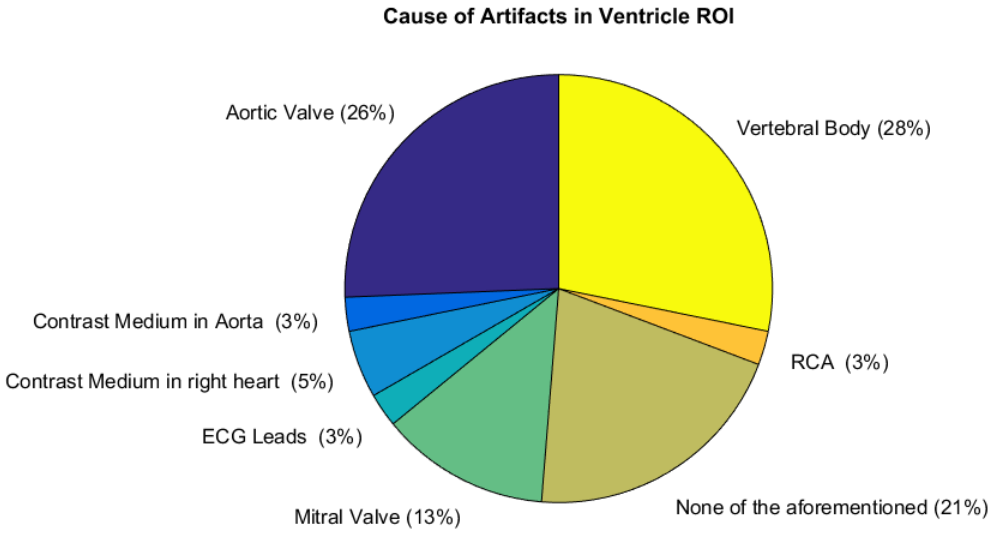

Figure B.6: Pieplot for the causes of Streak-artifacts in Ventricle

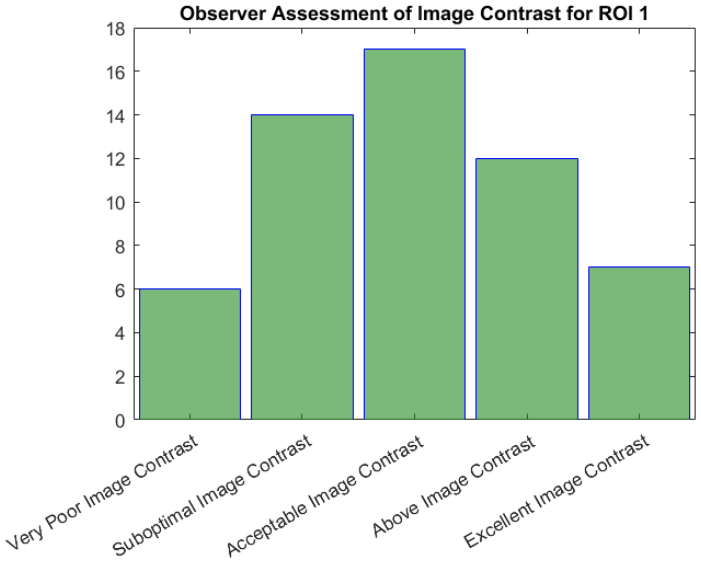

Figure B.7: Histogram for the observer evaluation of image contrast in ROI 1

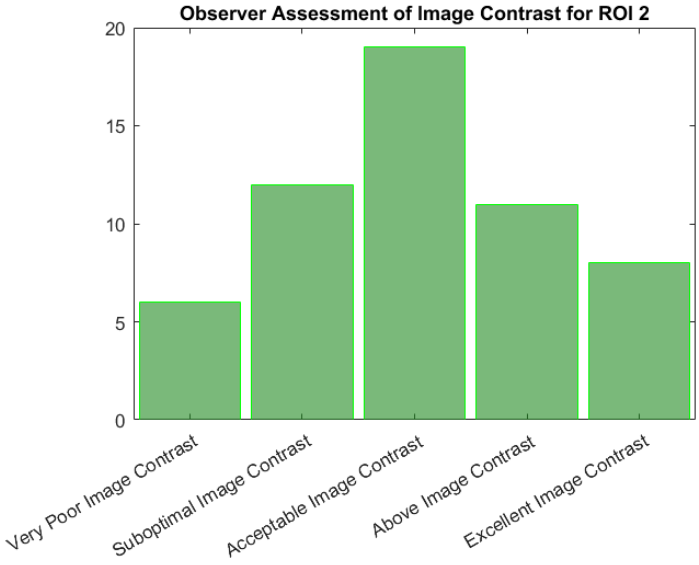

Figure B.8: Histogram for the observer evaluation of image contrast in ROI 2

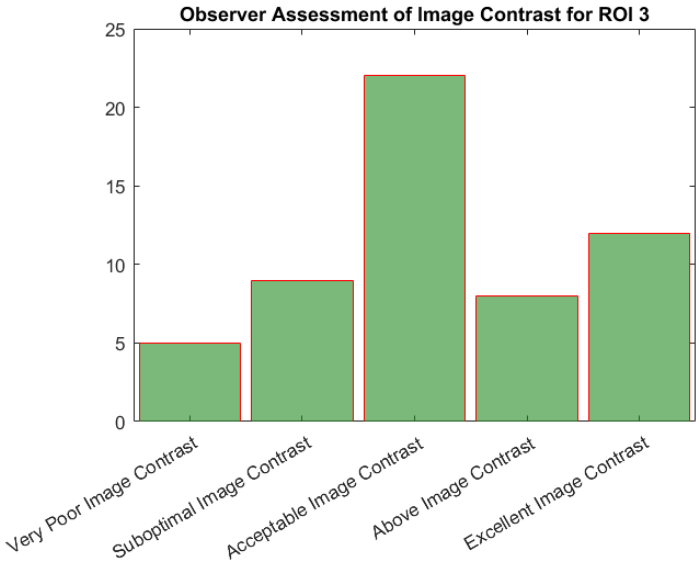

Figure B.9: Histogram for the observer evaluation of image contrast in ROI 3

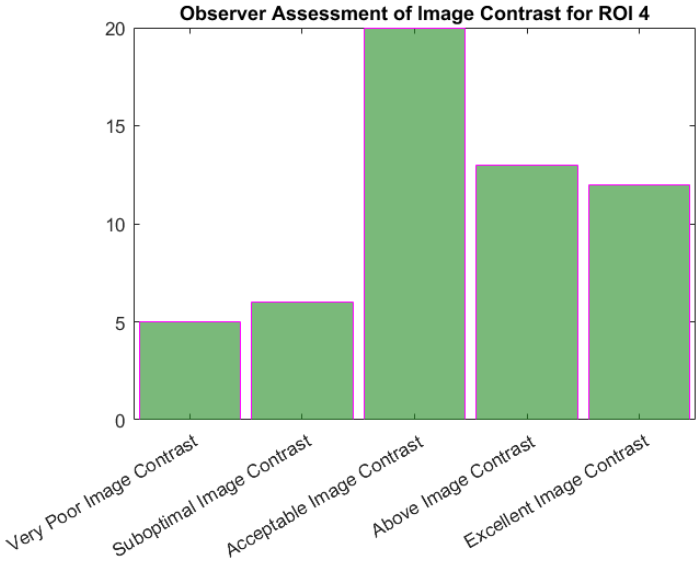

Figure B.10: Histogram for the observer evaluation of image contrast in ROI 4

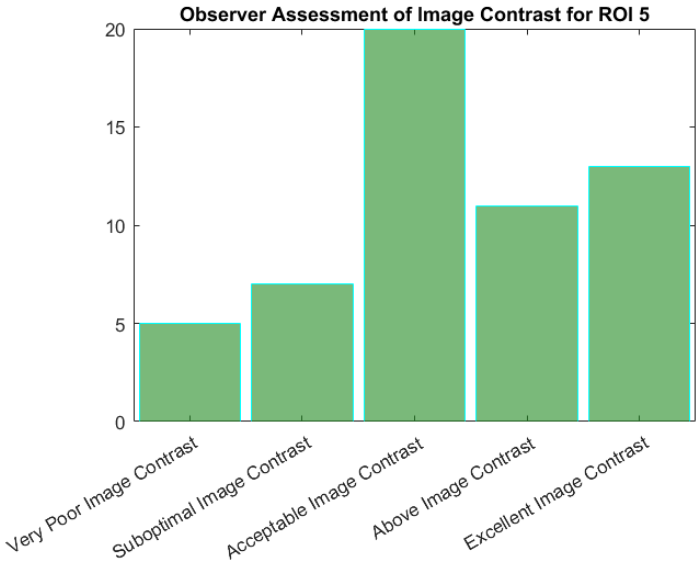

Figure B.11: Histogram for the observer evaluation of image contrast in ROI 5

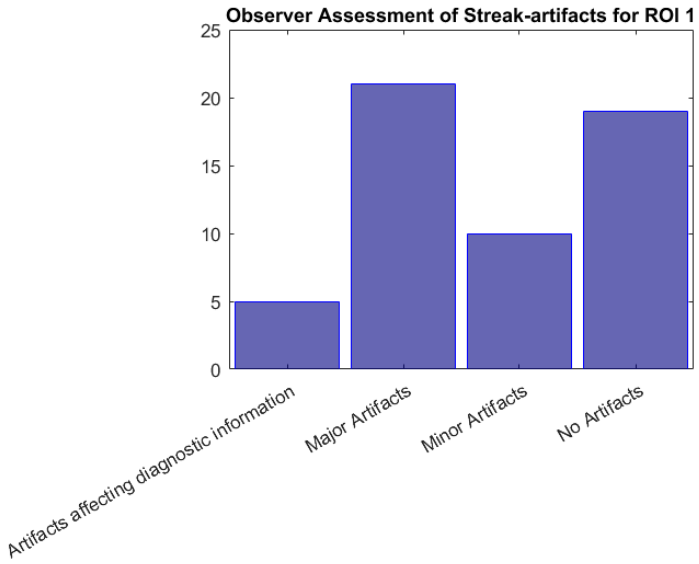

Figure B.12: Histogram for the observer evaluation of streak-artifacts in ROI 1

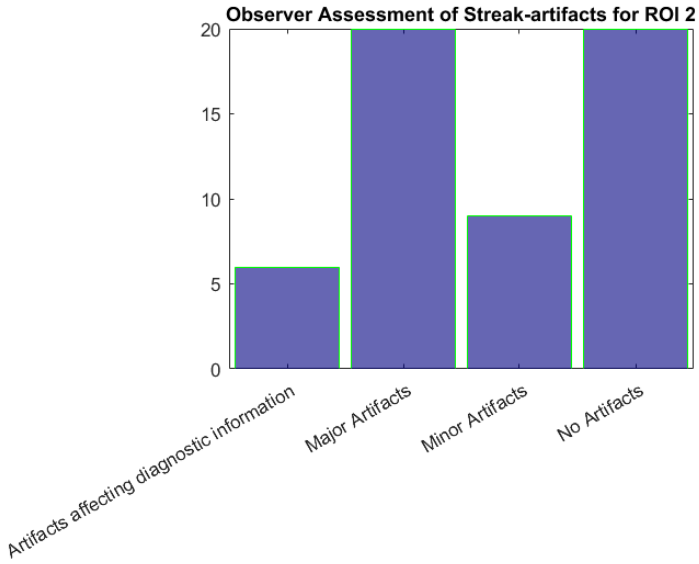

Figure B.13: Histogram for the observer evaluation of streak-artifacts in ROI 2

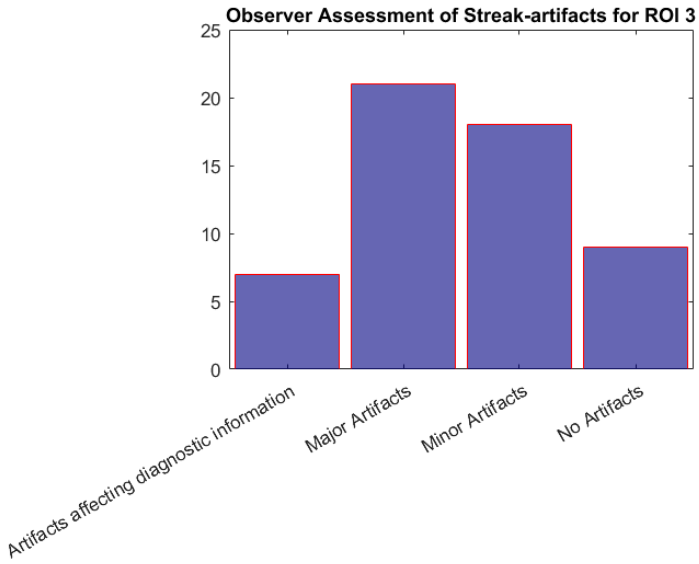

Figure B.14: Histogram for the observer evaluation of streak-artifacts in ROI 3

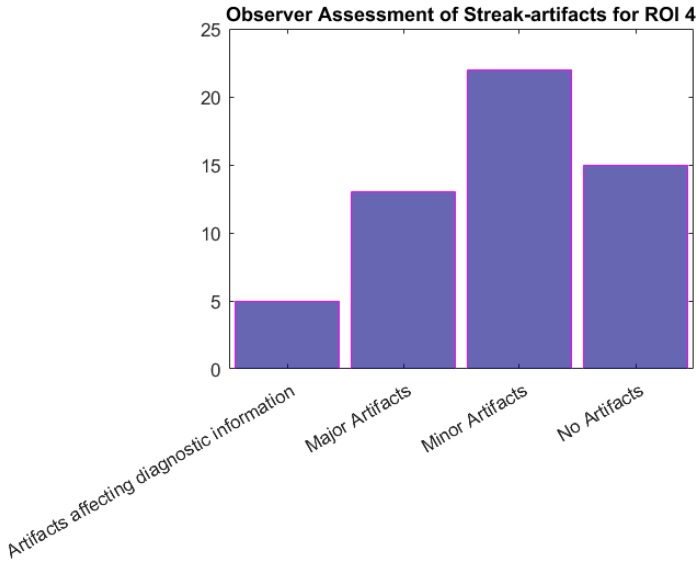

Figure B.15: Histogram for the observer evaluation of streak-artifacts in ROI 4

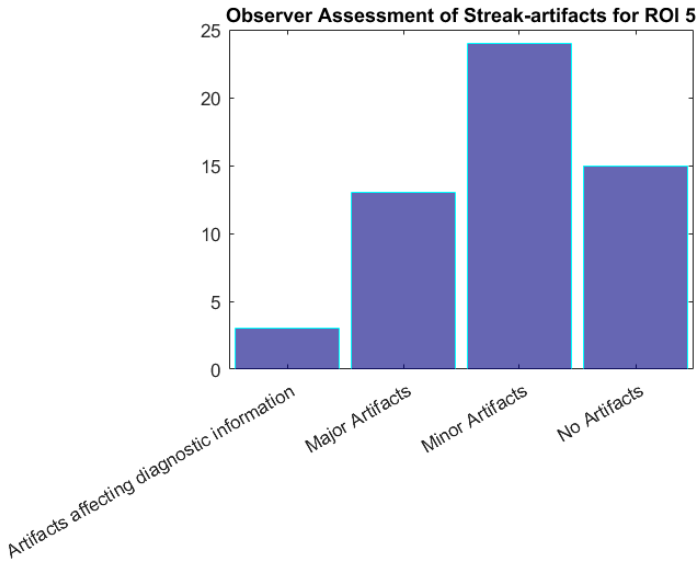

Figure B.16: Histogram for the observer evaluation of streak-artifacts in ROI 5

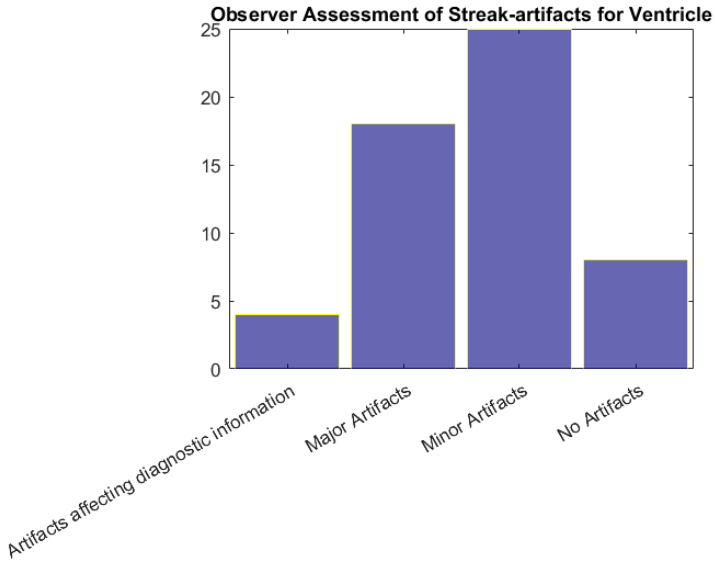

Figure B.17: Histogram for the observer evaluation of streak-artifacts in the ventricle

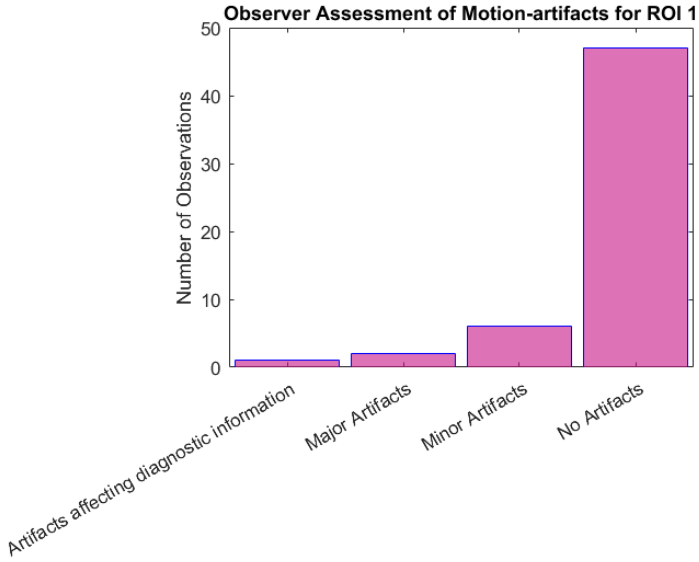

Figure B.18: Histogram for the observer evaluation of motion-artifacts in ROI 1

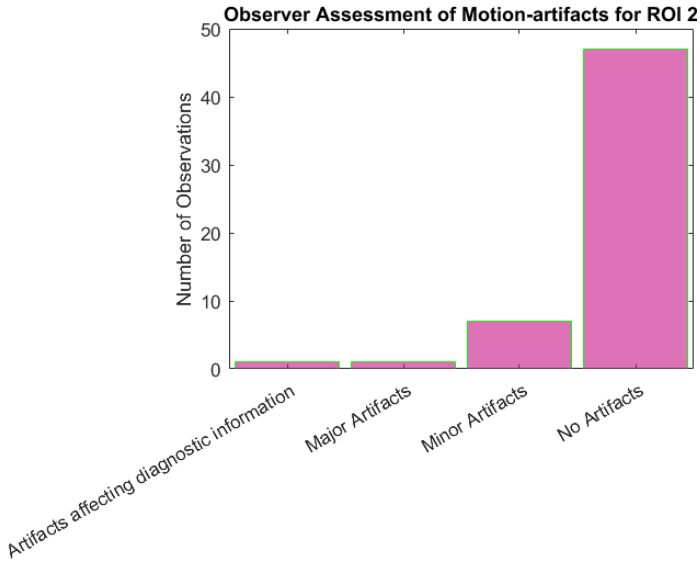

Figure B.19: Histogram for the observer evaluation of motion-artifacts in ROI 2

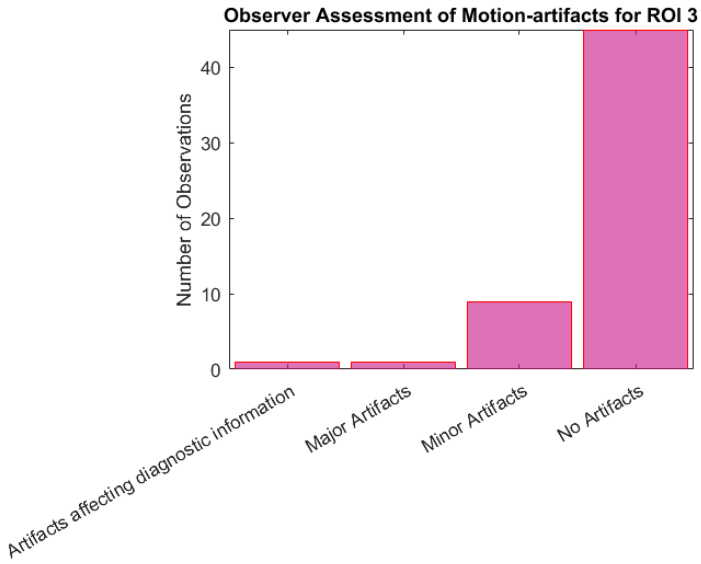

Figure B.20: Histogram for the observer evaluation of motion-artifacts in ROI 3

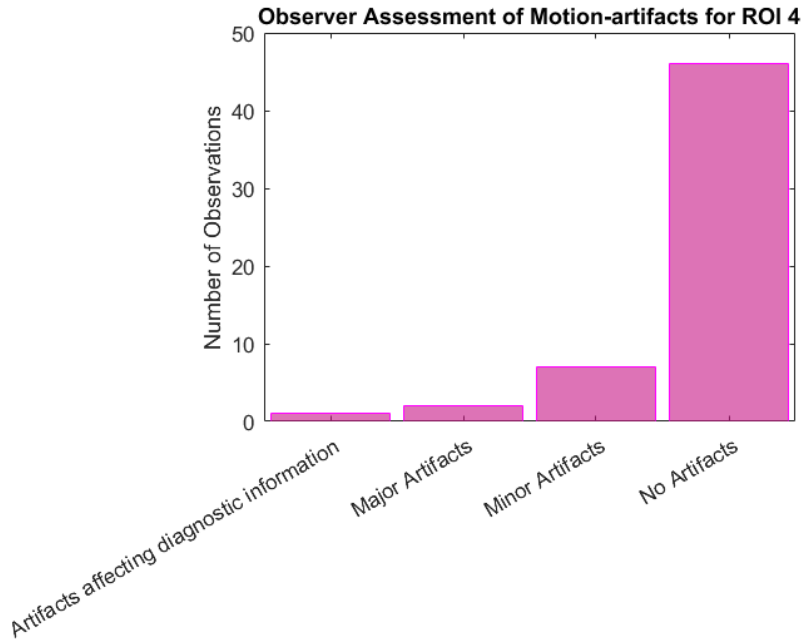

Figure B.21: Histogram for the observer evaluation of motion-artifacts in ROI 4

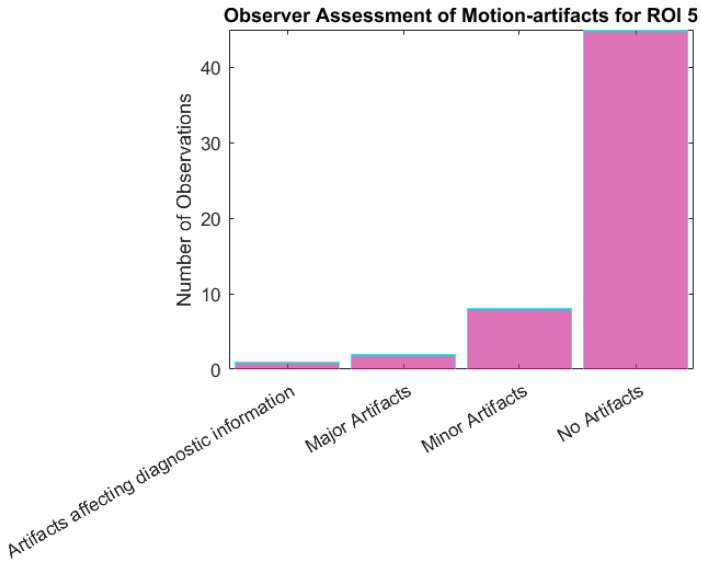

Figure B.22: Histogram for the observer evaluation of motion-artifacts in ROI 5

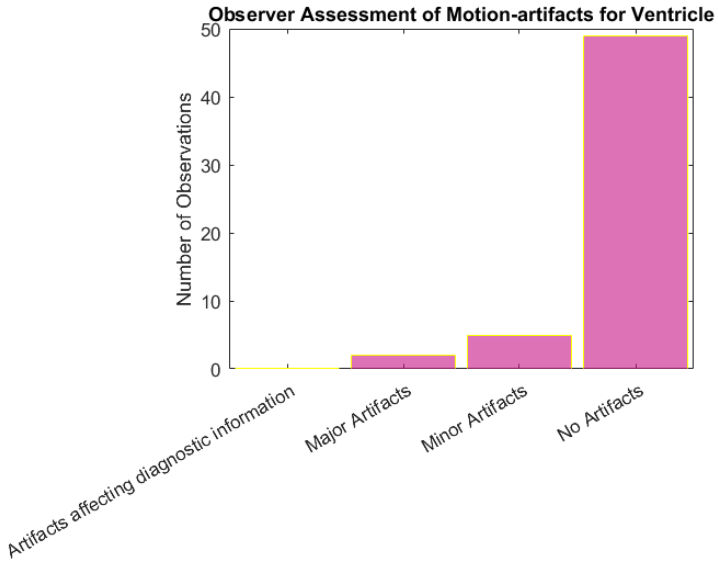

Figure B.23: Histogram for the observer evaluation of motion-artifacts in the ventricle

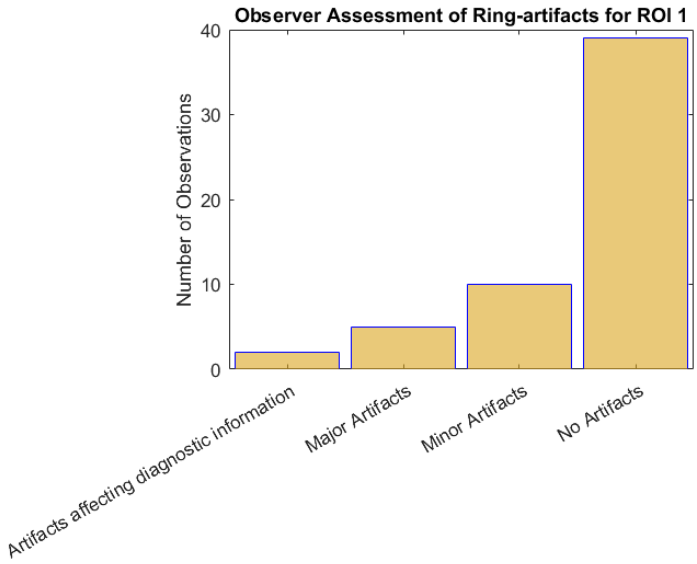

Figure B.24: Histogram for the observer evaluation of ring-artifacts in ROI 1

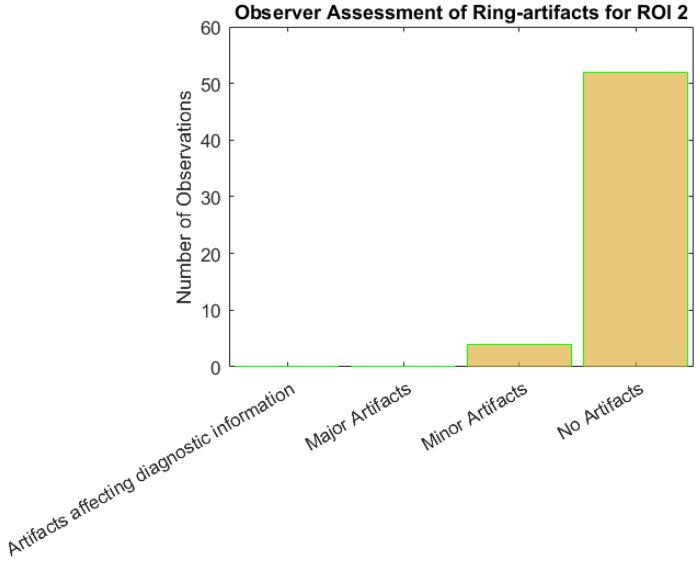

Figure B.25: Histogram for the observer evaluation of ring-artifacts in ROI 2

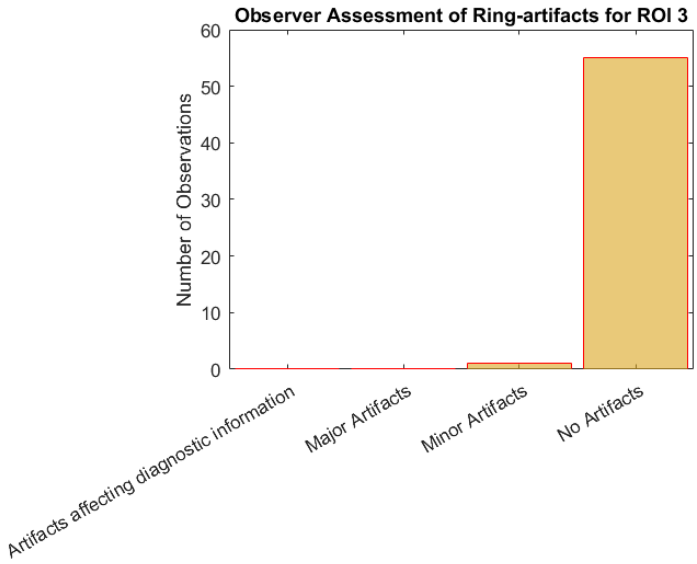

Figure B.26: Histogram for the observer evaluation of ring-artifacts in ROI 3

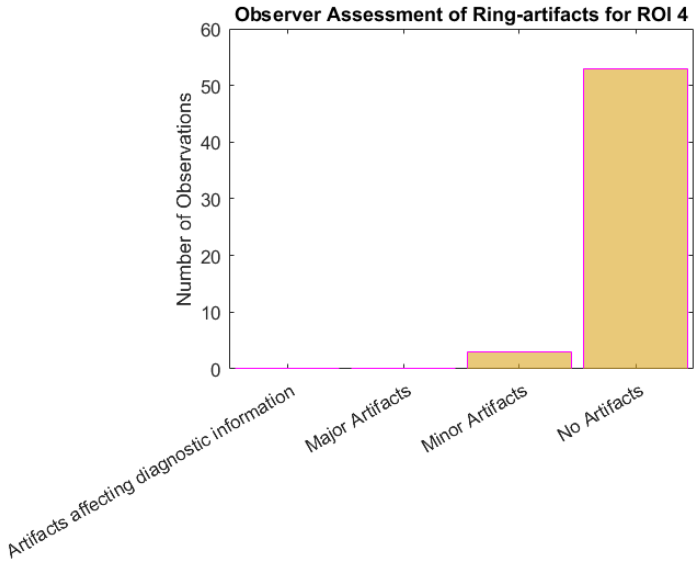

Figure B.27: Histogram for the observer evaluation of ring-artifacts in ROI 4

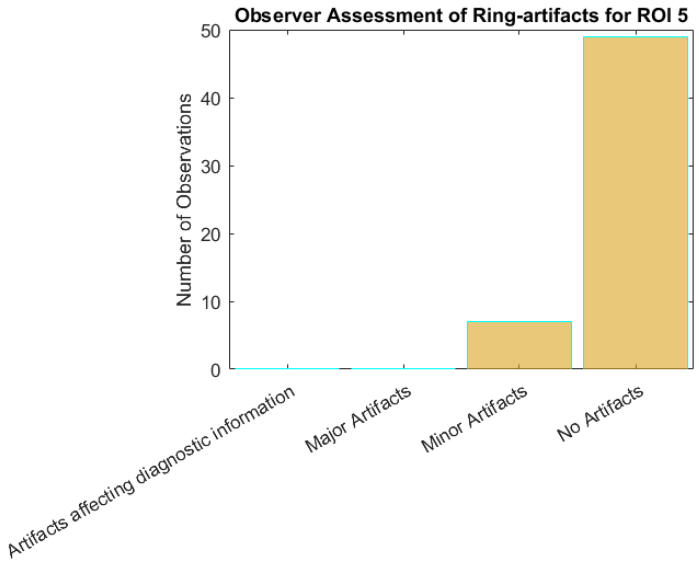

Figure B.28: Histogram for the observer evaluation of ring-artifacts in ROI 5

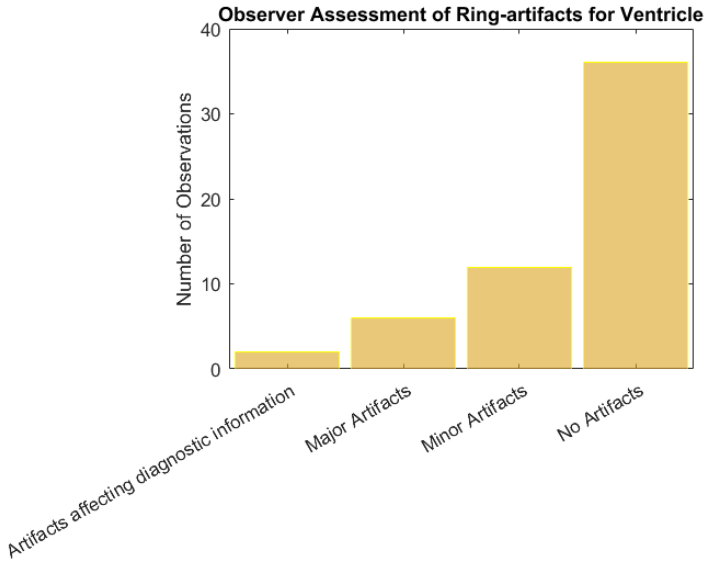

Figure B.29: Histogram for the observer evaluation of ring-artifacts in the ventricle

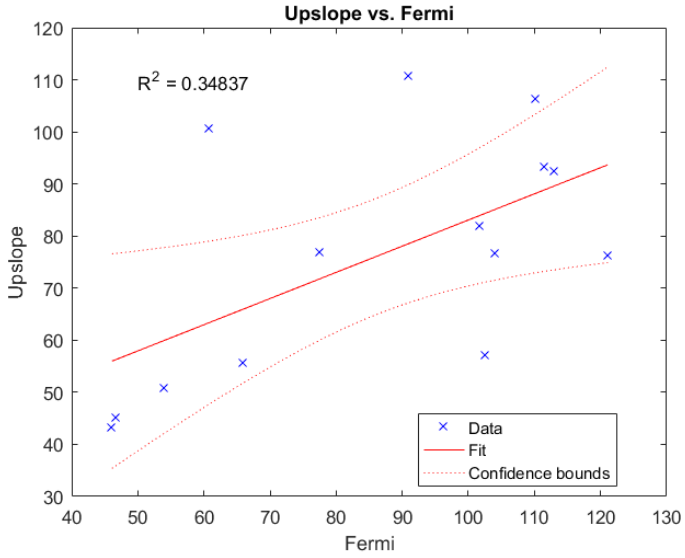

Figure B.30: Correlation between Upslope and Fermi method for MBF in ROI1

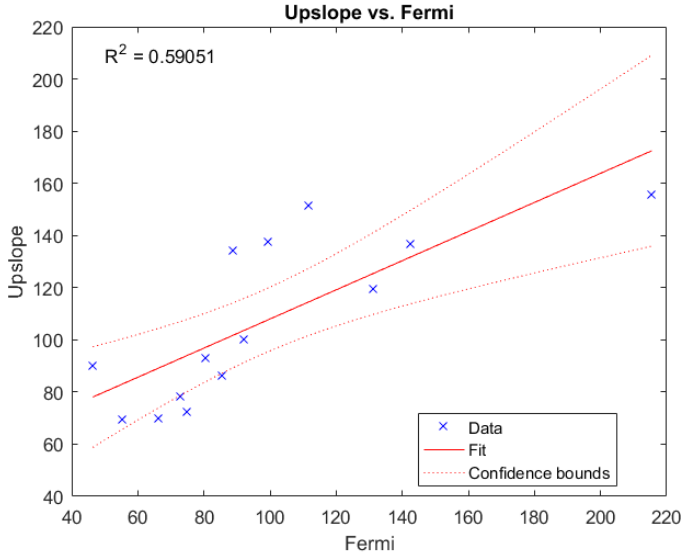

Figure B.31: Correlation between Upslope and Fermi method for MBF in ROI2

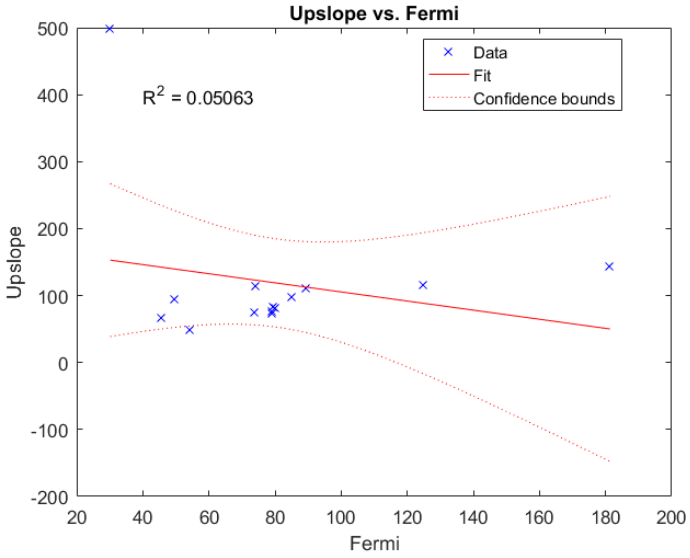

Figure B.32: Correlation between Upslope and Fermi method for MBF in ROI3

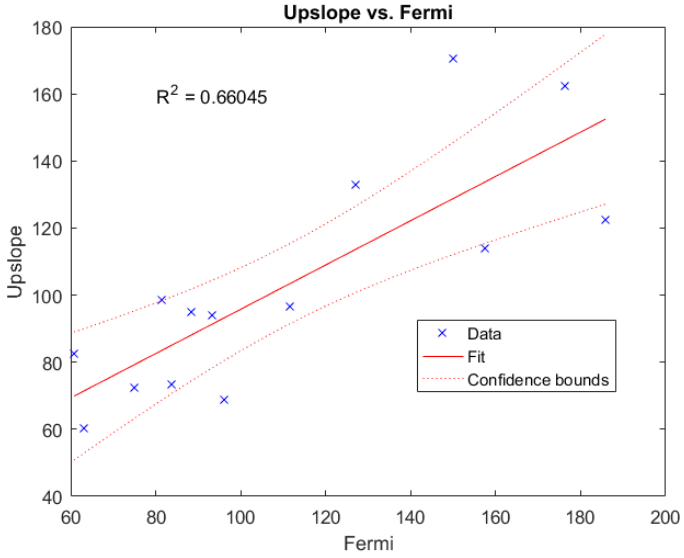

Figure B.33: Correlation between Upslope and Fermi method for MBF in ROI4

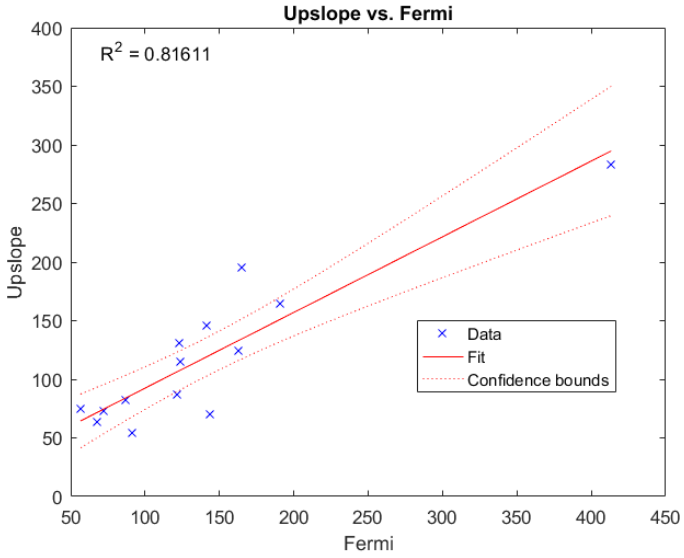

Figure B.34: Correlation between Upslope and Fermi method for MBF in ROI5

Bibliography

[1] N. Townsend, L. Wilson, P. Bhatnagar, K. Wickramasinghe, M. Rayner, and M. Nichols, "Cardiovascular disease in Europe: Epidemiological update 2016", en, *European Heart Journal*, vol. 37, no. 42, pp. 3232–3245, Nov. 2016, ISSN: 0195-668X. DOI: 10.1093/eurheartj/ehw334.

[2] A. Narang, A. Singh, and A. R. Patel, "Diagnostic usefulness of myocardial perfusion imaging in patients reluctant to undergo angiography", *Research Reports in Clinical Cardiology*, vol. 7, pp. 35–36, 2016.

[3] J. H. Mieres, A. N. Makaryus, R. F. Redberg, and L. J. Shaw, "Noninvasive cardiac imaging.", *American family physician*, vol. 75, no. 8, 2007.

[4] P. T. Siemers, C. B. Higgins, W. Schmidt, W. Ashburn, and P. Hagan, "Detection, quantitation and contrast enhancement of myocardial infarction utilizing computerized axial tomography: Comparison with histochemical staining and 99mTc-pyrophosphate imaging.", eng, *Investigative radiology*, vol. 13, no. 2, pp. 103–109, 1978, ISSN: 0020-9996.

[5] T. Techasith and R. C. Cury, "Stress myocardial CT perfusion: An update and future perspective", *JACC: Cardiovascular Imaging*, vol. 4, no. 8, pp. 905–916, 2011.

[6] A. Kurata, T. Mochizuki, Y. Koyama, T. Haraikawa, J. Suzuki, Y. Shigematsu, and J. Higaki, "Myocardial perfusion imaging using adenosine triphosphate stress multi-slice spiral computed tomography", *Circulation Journal*, vol. 69, no. 5, pp. 550–557, 2005.

[7] T. Rienmüller, C. Baumgartner, M. Handler, V. Makarenko, P. Ourednicek, I. Krestinich, S. Zhorzholiani, R. Rienmüller, and L. Bockeria, "Quantitative estimation of left ventricular myocardial perfusion based on dynamic CT scans", *Biomedical Engineering/Biomedizinische Technik*, 2013.

[8] S. Seitun, C. De Lorenzi, F. Cademartiri, A. Buscaglia, N. Travaglio, M. Balbi, and G. P. Bezante, *CT Myocardial Perfusion Imaging: A New Frontier in Cardiac Imaging*, en, https://www.hindawi.com/journals/bmri/2018/7295460/abs/, Research Article, 2018. DOI: 10.1155/2018/7295460.

[9] F. Cademartiri, S. Seitun, A. Clemente, L. La Grutta, P. Toia, G. Runza, M. Midiri, and E. Maffei, "Myocardial blood flow quantification for evaluation of coronary artery disease by computed tomography", *Cardiovascular Diagnosis and Therapy*, vol. 7, no. 2, pp. 129–150, Apr. 2017, ISSN: 2223-3652. DOI: 10.21037/cdt.2017.03.22.

[10] A. Fieselmann, M. Kowarschik, A. Ganguly, J. Hornegger, and R. Fahrig, "Deconvolution-based CT and MR brain perfusion measurement: Theoretical model revisited and practical implementation details", *Journal of Biomedical Imaging*, vol. 2011, p. 14, 2011.

[11] M. Jerosch-Herold, "Quantification of myocardial perfusion by cardiovascular magnetic resonance", *Journal of Cardiovascular Magnetic Resonance*, vol. 12, no. 1, p. 57, 2010.

[12] M. Toifl, "Quantitative Estimation of Left Ventricular Myocardial Perfusion Using Contrast Agent Computed Tomography", PhD Thesis, Master's Thesis. UMIT, 2014.

[13] A. E. Stillman, M. Oudkerk, D. A. Bluemke, M. J. de Boer, J. Bremerich, E. V. Garcia, M. Gutbertlet, P. van der Harst, W. G. Hundley, and M.

Jerosch-Herold, "Imaging the myocardial ischemic cascade", *The international journal of cardiovascular imaging*, pp. 1–15, 2018.

[14] K. L. Gould, K. Lipscomb, and G. W. Hamilton, "Physiologic basis for assessing critical coronary stenosis: Instantaneous flow response and regional distribution during coronary hyperemia as measures of coronary flow reserve", *The American journal of cardiology*, vol. 33, no. 1, pp. 87–94, 1974.

[15] S. Seitun, M. Castiglione Morelli, I. Budaj, S. Boccalini, A. Galletto Pregliasco, A. Valbusa, F. Cademartiri, and C. Ferro, "Stress Computed Tomography Myocardial Perfusion Imaging: A New Topic in Cardiology", *Revista Española de Cardiología (English Edition)*, vol. 69, no. 2, pp. 188–200, Feb. 2016, ISSN: 1885-5857. DOI: 10.1016/j.rec.2015.10.018.

[16] A. Varga-Szemes, F. G. Meinel, C. N. De Cecco, S. R. Fuller, R. R. Bayer, and U. J. Schoepf, "CT Myocardial Perfusion Imaging", *American Journal of Roentgenology*, vol. 204, no. 3, pp. 487–497, Feb. 2015, ISSN: 0361-803X. DOI: 10.2214/AJR.14.13546.

[17] D. Caruso, M. Eid, U. J. Schoepf, K. N. Jin, A. Varga-Szemes, C. Tesche, S. Mangold, A. Spandorfer, A. Laghi, and C. N. De Cecco, "Dynamic CT myocardial perfusion imaging", *European journal of radiology*, vol. 85, no. 10, pp. 1893–1899, 2016.

[18] B. Bischoff, F. Bamberg, R. Marcus, F. Schwarz, H.-C. Becker, A. Becker, M. Reiser, and K. Nikolaou, "Optimal Timing for First-Pass Stress CT Myocardial Perfusion Imaging", *The international journal of cardiovascular imaging*, vol. 29, no. 2, pp. 435–442, 2013.

[19] A. Isola, H. Schmitt, U. Van Stevendaal, P. Begemann, P. Coulon, L. Boussel, and M. Grass, "Image registration and analysis for quantitative myocardial perfusion: Application to dynamic circular cardiac CT", *Physics in medicine and biology*, vol. 56, no. 18, p. 5925, 2011.

[20] A. Singh, V. Mor-Avi, and A. R. Patel, "Update on Computed Tomography Myocardial Perfusion Imaging", *Current cardiovascular imaging reports*, vol. 9, Jul. 2016, ISSN: 1941-9066. DOI: 10.1007/s12410-016-9381-1.

[21] J. A. Rumberger, A. J. Feiring, M. J. Lipton, C. B. Higgins, S. R. Ell, and M. L. Marcus, "Use of ultrafast computed tomography to quantitate regional myocardial perfusion: A preliminary report", *Journal of the American College of Cardiology*, vol. 9, no. 1, pp. 59–69, 1987.

[22] A. Rossi, D. Merkus, E. Klotz, N. Mollet, P. J. de Feyter, and G. P. Krestin, "Stress myocardial perfusion: Imaging with multidetector CT", *Radiology*, vol. 270, no. 1, pp. 25–46, 2014.

[23] N. A. Mullani and K. L. Gould, "First-pass measurements of regional blood flow with external detectors", *Journal of Nuclear Medicine*, vol. 24, no. 7, pp. 577–581, 1983.

[24] L.-Y. Hsu, D. W. Groves, A. H. Aletras, P. Kellman, and A. E. Arai, "A quantitative pixel-wise measurement of myocardial blood flow by contrast-enhanced first-pass CMR perfusion imaging: Microsphere validation in dogs and feasibility study in humans", *JACC: Cardiovascular Imaging*, vol. 5, no. 2, pp. 154–166, 2012.

[25] L. Axel, "Tissue mean transit time from dynamic computed tomography by a simple deconvolution technique.", eng, *Investigative radiology*, vol. 18, no. 1, pp. 94–99, 1983, ISSN: 0020-9996.

[26] M. Jerosch-Herold, "Quantification of myocardial perfusion by cardiovascular magnetic resonance", *Journal of Cardiovascular Magnetic Resonance*, vol. 12, no. 1, p. 57, Oct. 2010, ISSN: 1532-429X. DOI: 10.1186/1532-429X-12-57.

[27] L. W. Goldman, "Principles of CT: Radiation dose and image quality", *Journal of nuclear medicine technology*, vol. 35, no. 4, pp. 213–225, 2007.

[28] F. Zarb, L. Rainford, and M. F. McEntee, "Image quality assessment tools for optimization of CT images", *Radiography*, vol. 16, no. 2, pp. 147–153, 2010.

[29] W. A. Kalender, *Computed Tomography: Fundamentals, System Technology, Image Quality, Applications*. John Wiley & Sons, 2011.

[30] L. L. Geyer, U. J. Schoepf, F. G. Meinel, J. W. Nance Jr, G. Bastarrika, J. A. Leipsic, N. S. Paul, M. Rengo, A. Laghi, and C. N. De Cecco, "State of the art: Iterative CT reconstruction techniques", *Radiology*, vol. 276, no. 2, pp. 339–357, 2015.

[31] M. Beister, D. Kolditz, and W. A. Kalender, "Iterative reconstruction methods in X-ray CT", *Physica medica*, vol. 28, no. 2, pp. 94–108, 2012.

[32] J. T. Bushberg, J. A. Seibert, E. M. Leidholdt, and J. M. Boone, "The essential physics of medical imaging. 2nd", *Philadelphia: Lippincott Williams & Wilkins*, vol. 16, p. 933, 2002.

[33] F. Cademartiri, G. Casolo, and M. Midiri, *Clinical Applications of Cardiac CT*. Springer, 2008, ISBN: 978-88-470-0862-5.

[34] J. F. Barrett and N. Keat, "Artifacts in CT: Recognition and avoidance", *Radiographics*, vol. 24, no. 6, pp. 1679–1691, 2004.

[35] H. S. Choi, B. W. Choi, K. O. Choe, D. Choi, K.-J. Yoo, M.-I. Kim, and J. Kim, "Pitfalls, Artifacts, and Remedies in Multi– Detector Row CT Coronary Angiography", *RadioGraphics*, vol. 24, no. 3, pp. 787–800, May 2004, ISSN: 0271-5333. DOI: 10.1148/rg.243035502.

[36] F. E. Boas and D. Fleischmann, "CT artifacts: Causes and reduction techniques", *Imaging Med*, vol. 4, no. 2, pp. 229–240, 2012.

[37] R. L. Morin, T. C. Gerber, and C. H. McCollough, "Radiation dose in computed tomography of the heart", *Circulation*, vol. 107, no. 6, pp. 917–922, 2003.

[38] W. A. Kalender, "Dose in x-ray computed tomography", *Physics in Medicine & Biology*, vol. 59, no. 3, R129, 2014.

[39] M. K. Kalra, M. M. Maher, T. L. Toth, B. Schmidt, B. L. Westerman, H. T. Morgan, and S. Saini, "Techniques and Applications of Automatic Tube Current Modulation for CT", *Radiology*, vol. 233, no. 3, pp. 649–657, Dec. 2004, ISSN: 0033-8419. DOI: 10.1148/radiol.2333031150.

[40] . M\a ansson, "Methods for the evaluation of image quality: A review", *Radiation protection dosimetry*, vol. 90, no. 1-2, pp. 89–99, 2000.

[41] J. D. Thompson, "Image Quality: An unanswered problem?", *OPTIMAX 2017*, p. 27,

[42] M. Bath and L. G. Mansson, "Visual grading characteristics (VGC) analysis: A non-parametric rank-invariant statistical method for image quality evaluation", *The British journal of radiology*, vol. 80, no. 951, pp. 169–176, 2007.

[43] E. Ludewig, A. Richter, and M. Frame, "Diagnostic imaging–evaluating image quality using visual grading characteristic (VGC) analysis", *Veterinary research communications*, vol. 34, no. 5, pp. 473–479, 2010.

[44] P. Bhosale, "Comparing CNR, SNR, and Image Quality of CT Images Reconstructed with Soft Kernel, Standard Kernel, and Standard Kernel plus ASIR 30% Techniques", en, *International Journal of Radiology*, vol. 2, no. 2, pp. 60-65–65, Dec. 2015, ISSN: 2313-3406.

[45] H. Demirturk Kocasarac, D. Helvacioglu Yigit, B. Bechara, A. Sinanoglu, and M. Noujeim, "Contrast-to-noise ratio with different settings in a CBCT machine in presence of different root-end filling materials: An in vitro study", eng, *Dento Maxillo Facial Radiology*, vol. 45, no. 5, p. 20 160 012, 2016, ISSN: 0250-832X. DOI: 10.1259/dmfr.20160012.

[46] J. F. Lawless, *Statistical Models and Methods for Lifetime Data*, en. John Wiley & Sons, Jan. 2011, ISBN: 978-1-118-03125-4.

[47] *Weibull Distribution - MATLAB & Simulink - MathWorks Deutschland*, https://de.mathworks.com/help/stats/weibull-distribution.html, Apr. 2019.

[48] Thompson Howard K., Starmer C. Frank, Whalen Robert E., and Mcintosh Henry D., "Indicator Transit Time Considered as a Gamma Variate", *Circulation Research*, vol. 14, no. 6, pp. 502–515, Jun. 1964. DOI: 10.1161/01.RES.14.6.502.

[49] O. Camara, T. Mansi, M. Pop, K. Rhode, M. Sermesant, and A. Young, *Statistical Atlases and Computational Models of the Heart: Imaging and Modelling Challenges: 5th International Workshop, STACOM 2014, Held in Conjunction with MICCAI 2014, Boston, MA, USA, September 18, 2014, Revised Selected Papers*, en. Springer, Dec. 2014, ISBN: 978-3-319-14678-2.

[50] M. T. Madsen, "A simplified formulation of the gamma variate function", en, *Physics in Medicine and Biology*, vol. 37, no. 7, pp. 1597–1600, Jul. 1992, ISSN: 0031-9155. DOI: 10.1088/0031-9155/37/7/010.

[51] C. Baumgartner, *Messung Der Cerebralen Durchblutung Mittels Elektronenstrahl-Computertomographie*. na, 1998.

[52] S. D. Qanadli, A.-M. Jouannic, J. Dehmeshki, and T.-L. Lu, "CT attenuation values of blood and myocardium: Rationale for accurate coronary artery calcifications detection with multi-detector CT", eng, *PloS One*, vol. 10, no. 4, e0124175, 2015, ISSN: 1932-6203. DOI: 10.1371/journal.pone.0124175.

[53] L. Fahrmeir, R. Künstler, I. Pigeot, and G. Tutz, "Statistik der Weg zur Datenanalyse (7. Aufl., korr. Nachdr.)", *Berlin [ua]: Springer*, 2011.

[54] *Kruskal-Wallis test - MATLAB kruskalwallis - MathWorks Deutschland*, https://de.mathworks.com/help/stats/kruskalwallis.html?s_tid=doc_ta, Apr. 2019.

[55] K.-T. Ho, H.-Y. Ong, G. Tan, and Q.-W. Yong, "Dynamic CT myocardial perfusion measurements of resting and hyperaemic blood flow in low-risk subjects with 128-slice dual-source CT", en, *European Heart Journal - Cardiovascular Imaging*, vol. 16, no. 3, pp. 300–306, Mar. 2015, ISSN: 2047-2404. DOI: 10.1093/ehjci/jeu200.